Evaluating the Aerodynamic Performance of MFC-Actuated Morphing Wings to Control a Small UAV

Troy Anthony Probst

Thesis submitted to the Faculty of the
Virginia Polytechnic Institute and State University
in partial fulfillment of the requirements for the degree of

Master of Science
in
Mechanical Engineering

Kevin B. Kochersberger, Chair
Scott W. Case
Pablo A. Tarazaga

Date October 16, 2012
Blacksburg, Virginia

Keywords: Morphing Wings, Macro Fiber Composites, Composite Laminates

Evaluating the Aerodynamic Performance of MFC-Actuated Morphing Wings to Control a Small UAV

Troy Anthony Probst

ABSTRACT

The purpose of this research is to evaluate certain performance characteristics of a morphing wing system that uses Macro Fiber Composites (MFC) to create camber change. This thesis can be broken into two major sections. The first half compares a few current MFC airfoil designs to each other and to a conventional servomechanism (servo) airfoil. Their performance was measured in terms of lift and drag in a 2-D wind tunnel. The results showed MFC airfoils were effective but limited by aeroelasticity compared to the servo. In addition, a morphed airfoil and a flapped airfoil were rapid prototyped and tested to isolate the effects of discontinuity. The continuous morphed airfoil produced more lift with less drag.

The second half of this thesis work focused on determining the ideal MFC configurations for a thin wing application. Simulations were run on a thin wing with embedded MFCs such that the whole wing morphed. Finite element and vortex lattice models were used to predict deflections and rolling moment coefficients. Different configuration parameters were then varied to quantify their effect. The comparisons included MFC location, number of MFCs, material substrate, and wing thickness. A prototype wing was then built and flight tested. While the simulations overestimated the wing deflection, the flight results illustrated the complexity and variability associated with the MFC morphing system. The rolling moment coefficients from flight were consistent with the simulation given the differences in deflection.

Acknowledgments

The following research would not have been possible without the generous support of those around me. First and foremost, I would like to thank my parents, Joyce and Tony Probst. They were always there for advice or anything I needed along the way. Any decision I made, they were always behind me one hundred and ten percent. Next, I would like to thank my advisor Dr. Kevin Kochersberger. As one of the lead investigators on this project, he gave me the opportunity to explore this exciting new area of research. His advice and guidance were invaluable to the project and to my research. Like many research endeavours, this project is a continuation of the work of previous researchers, particularly Eric Gustafson who instructed me and introduced me to the project. I also could not have done anything without Osgar John Ohanian III from AVID LLC., and his commitment to the project. I would also like to thank his colleagues at AVID LLC., particularly Etan Karni, Brandon Stiltner, Christopher Hickling, and Christopher Olien for all their hard work. In addition, I would be remiss if I did not mention my colleagues at Virginia Tech especially the hard-working members of the Unmanned Systems Laboratory. Peter Fanto, Bryan Krawiec, Kenneth Kroeger, Bob Collins, Brian David, Justin Stiltner, Matt Turok, Mike Bromely, and Donnie Rodgers were all instrumental to my research.

I would also like to thank my sponsors. First, thank you to the AFRL Munitions Directorate for funding the research through a Phase II SBIR and to the SMART Program for funding my education. All figures are the author's work except as noted.

Table of Contents

List of Figures

List of Tables

Nomenclature

Acronyms

AFC	Active Fiber Composite
AMPS	AM Power Systems
AVL	Athena Vortex Lattice
CF	Carbon Fiber
CIMSS	Center for Intelligent Material Systems and Structures
CLT	Classical Lamination Theory
DAQ	Digital Aquisition
FE	Finite Element
GenMAV	Generic Micro Aerial Vehicle
LE	Leading Edge
MAV	Micro Aerial Vehicle
MFC	Macro-Fiber Composite
PWM	Pulse Width Modulated
PZT	Lead Zirconate Titanate
RP	Rapid Prototyping
TE	Trailing Edge
UAV	Unmanned Aerial Vehicle

Chapter 1

Introduction

Unmanned aerial vehicles (UAVs) are becoming an increasingly important technology both in the military and in commercial applications. In recent years, computing and mechanical technology has advanced significantly and along with increased understanding of aerodynamics, research has pushed the boundaries of what UAVs can do. UAVs can be large and carry heavy payloads, or they can be small with more agility. For example, General Atomic's MQ-1 Predator drones with a wingspan of 55 ft. have been widely accepted into use in the United States military[1]. On the other hand, the Aeryon Scout, a hand-carried, vertical take-off UAV, weighs less than 3 lbs. and is for vastly different missions such as urban surveillance[2]. UAVs can be built with a wide range of capabilities to conquer myriad different objectives. The research presented here focuses on the improvement of small fixed-wing UAVs, in particular those with approximately 2 ft. wingspan.

The flight system for a conventional UAV consists of a propulsion system, a lifting surface such as wings, and control surfaces. The control surfaces do exactly what the name implies; they control the aircraft. The most common method is to move the control surface such that the aerodynamic forces change which consequently changes the movement of the aircraft. For example, conventional ailerons are flapped surfaces attached to the trailing edge of a main wing. Their movement creates camber change which changes the lift profile. Applied

asymmetrically to each half of the wing, the changes in lift create a rolling moment and the airplane turns. Examples of typical control surfaces include ailerons, elevators, rudder, and flaps.

For small UAVs, the conventional method is to have a servomechanism (servo) move a linkage which moves a hinged control surface. This system of moving hinged surfaces has been used with great success for many years, and almost all fixed-wing airplanes today, from hobbyists' remote controlled (RC) planes to the Boeing 747, use some variation of this system. The research presented here investigates an alternative approach using embedded piezoelectric actuators which bend the wing itself instead of moving discrete hinged control surfaces.

The embedded piezoelectric devices convert voltage to strain, and the wing changes shape. The new shape creates different aerodynamic forces and thus enacts control. Specifically, this research looks at using piezoelectric devices called macro-fiber composites (MFCs). These are commercially available actuators which expand or contract in response to voltage. When embedded in wing, the expansion or contraction bends, or morphs, the wing. Control surfaces actuated in this manner potentially offer distinct advantages over conventional hinged surfaces. MFC-actuated morphing wings could have continuous surfaces. Discontinuities on the wing such as those created by hinges can cause separation increasing drag and reducing lift. In addition, MFCs could also provide a larger control bandwidth compared with servomechanism systems.

1.1 Motivation

The motivation behind this research was to evaluate the performance of the MFC-actuated morphing wing system. Theoretically, the MFC system does offer some advantages as mentioned above. Morphing wings can be continuous and solid-state. With no moving parts or external linkages, the MFC actuation potentially could be a more reliable alternative to servos. Other researchers are currently investigating the reliability of MFCs. In addition,

morphing surfaces allow UAV designers to easily employ thin wings ($\approx 0.4mm$) which would not feasible with servos, linkages, and flaps. Early studies have also shown the MFCs offer advantages in terms of frequency response and bandwidth[3]. However, like any technology MFCs have their own set of limitations including non-linear actuation and the necessity of operation on a relatively flexible wing, resulting in significant aeroelastic effects..

Because this is a relatively new technology, only a few different researchers have studied MFCs and morphing wings. Bilgen proved the concept could work by designing and building a small UAV with MFC-morphing control surfaces[4]. Gustafson built on this research and looked at improving many aspects of the MFC system. His work included designing a method for simulating morphing airfoils and verified it with wind tunnel testing[5]. Their work and that of other researchers has shown the potential of the MFC technology in morphing wings and morphing control surfaces, but they have also identified some key disadvantages. The research presented here attempts to further evaluate and more importantly quantify the MFCs' advantages and disadvantages as control surfaces. In addition, simulations were performed to study how to best take utilize the MFC technology in morphing wings.

1.2 Proposed Method and Organization

This research is organized into two major objectives: first, to evaluate the current MFC morphing technology and compare it to conventional servos, and second, to investigate how different wing parameters affect the capabilities of a fully morphing, MFC-actuated wing.

For the first objective, a series of experiments were performed. Gustafson and others have designed and built functioning MFC-embedded airfoils which have shown promise for actual flight implementation[5][6]. These airfoils are designed to operate as discrete control surfaces where only a certain section of the wing is separated as the designated moving control surface. This is how many current flapped control surfaces are configured. The research presented here tested the existing airfoil designs in a 2-D wind tunnel to measure and evaluate the

aerodynamic performance of this type of morphing control surface. A similar conventional servo-actuated airfoil was also tested for comparison. Non-actuating replicas of the MFC and servo airfoils were then tested in the 2-D wind tunnel to isolate and quantify the aerodynamic effect of the flap's discontinuity. In addition, frequency response testing was performed on the MFC and servo airfoils to quantify any differences. Chapter 3 details the background behind MFC technology and provides a brief description of the wind tunnel equipment and procedure. Chapter 4 and Chapter 5 then present and analyze the results of the 2-D wind tunnel experiments and frequency response experiments respectively.

To address the second objective of this thesis, finite element simulations were performed to characterize the effect of different parameters on the morphing effectiveness. The experiments of the first part of this thesis tested MFCs in a discrete control surface configuration. These simulations of the second part looked at using the MFCs to morph the entire wing surface of a small UAV. A methodology using finite element and vortex lattice software was developed where the 3-D aerodynamic performance of a wing surface could be estimated given the MFC and composite configuration. Many simulations were run that varied critical parameters such as relative MFC location, wing thickness, and substrate material to quantify the effect of each. A wing was then fabricated and flight tested to evaluate the simulations. Chapter 6 gives a thorough description of the simulation methodology, and Chapter 7 presents the simulation results and comparison to flight data.

Chapter 2

Literature Review

This section presents a brief review of the literature relevant to this research. The review is broken up into four sections. The first describes the work into MFC technology in general while the second section looks at MFCs applied specifically to morphing airfoils and wings. Next, a few other morphing UAV designs are presented, and the last section examines literature related to modeling and simulating the aerodynamics of UAVs.

2.1 MFC Technology

Macro-fiber composites were originally designed by researchers at NASA Langley Research Center[7]. In their paper, Wilke et al. describe the design of the MFC actuator and evaluate it against other piezoelectrics available at the time. The MFC actuator was designed with a few features that give it significant advantages to the other piezoelectrics. MFCs are composites of piezoelectric fibers embedded in an epoxy matrix with interdigitated copper electrodes. The interdigitated electrodes allow for in-plane poling of the piezoelectrics and use of the strong d_{33} coupling constant. This configuration is also similar to that of active fiber composite (AFC) actuators, and allows for a high strain yet flexible actuator. However,

before MFCs, "piezoelectric fiber composites have typically employed high cost, extruded, round piezocermic fibers". Wilkie et al. developed a manufacturing method that used rectangular fibers. This method allowed MFC to be relatively inexpensive actuator that "retains most of the advantageous features of active fiber composite actuators". The result is that MFCs were able to produce large strains on the order of 2000 microstrain under a relatively low voltage cycle of 4000 V peak-to-peak. MFCs were also shown to have significantly long endurance and were flexible. The authors also discuss research into different potential applications of the technology. All statements come from [7].

Williams [8] then researched the behavior of piezoceramic composites in his Ph.D. dissertation. He looked at and modeled the complex non-linear behavior of the actuators theoretically and verified his results experimentally. His contributions include verifying that the rule-of-mixtures and classical lamination theory hold for MFCs and developing models for the mechanical behavior of a piezoelectric material subject to different types of mechanical and electrical loads. He also experimentally determined the piezoelectric strain parameters of an MFC under certain conditions, and modeled MFC hysteresis by modifying the Preisach model. His research into the theory behind and the behavior of MFCs allowed others to model and use MFCs in different applications[8].

2.2 MFC Morphing Control Surfaces

Bilgen [4][9] built on the research of Williams and Wilkie and applied the piezoelectrics to morphing wings. He implemented the MFCs by bonding them to the surface of a substrate. When the MFC expands the substrate bends and changes shape. If the substrate is the wing of a UAV, the bending changes the wing shape and provides control authority. In his master's thesis, Bilgen designed, tested, built, and flew a small fixed-wing UAV with MFC-actuated control surfaces[4]. His design included computer modeling and wind tunnel testing. The flight test aircraft employed one MFC 8557 actuator in a unimorph configuration near each

wingtip. The plane had a 0.76 m wingspan and flew at approximately 13 -17 m/s. In the end, six successful flight tests of the morphing-wing UAV were performed which showed both the issues and the potential advantages of a UAV with morphing control surfaces[4].

In his Ph.D. dissertation[9], Bilgen researched how to best apply the piezocermanic composites to morph the wings of UAVs. MFCs were compared to other piezoelectrics, and different substrates and different MFC configurations were tested for the best displacement and potential in morphing wings. He first studied MFC unimorph structures for energy harvesting and UAV morphing applications. One hurdle to applying MFCs to UAVs is the high voltage and complex circuitry required. Bilgen designed a lightweight circuit to actuate bimorphs and then applied his circuit to a simple morphing airfoil. His work also extended some into applying morphing control surfaces on vertical take-off and landing (VTOL) aircraft[9]. Bilgen then designed a few composite morphing airfoils and tested them. As part of his master's and doctoral experiments, he designed and built a 2-D wind tunnel[9]. His final version of the wind tunnel is at Virginia Tech's Center for Intelligent Material Systems and Structures (CIMSS) and was used for the wind tunnel experiments presented in the thesis here. Overall, Bilgen showed that a UAV with MFC-actuated control surfaces was feasible and potentially offered advantages over conventional technology[9].

Extending Bilgen's work to a flight application, Gustafson [5] then designed and verified a method of modeling and simulating MFC-actuated morphing airfoils. From MFC properties, Gustafson derived an analogy relating the MFC piezoelectric strain to thermal strain. The analogy was then applied to a finite element (FE) model for a composite MFC morphing airfoil[5]. He designed a thin composite airfoil based on a generic UAV airfoil profile from Stewert et al.[10]. As applied to the 2-D composite airfoils, Gustafson used FE and 2-D aerodynamics simulations to optimize certain composite substrate parameters. He then verified his simulations with both static deflection tests and wind tunnel experiments. His wind tunnel experiments used a composite GenMAV airfoil embedded with a single 8557 MFC bimorph. The experiments validated his models and simulations and provided more evidence that MFCs could be implementing successfully in a UAV[5].

Other researchers have shown success modeling and building UAVs which employ MFC actuators. Butt, et al. designed, built, and flew a fixed wing UAV with MFC-actuated main wings and a conventional servo tail[11]. LaCroix and Ifju also have done FE models and simulations of MFCs in different configurations. Their work primarily looks at applying them to a much smaller micro aerial vehicle (MAV) type aircraft[12].

2.3 Other UAV Morphing Systems

Many different researchers have looked at morphing UAV configurations. Barbarino et al. [13] gives a thorough review of many of the current morphing aircraft projects. Morphing is a broad term that can apply to a number of situations where the aircraft changes shape. In some cases, the morphing relies on mechanical motion while others use smart materials like piezoelectrics[13]. This section details a few of the many morphing fixed wing UAV designs.

Vos et al. [14] designed a wing morphing system which employs post-buckled precompressed (PBP) piezoelectric bender actuators. In this system, the actuators, embedded in a deformable wing structure, induce camber change. When in the PBP configuration "the piezoelectric bimorph bender actuators can achieve significantly higher deflections than for conventional piezoelectric bender actuators"[14]. The authors develop a model to predict the behavior of the PBP elements using classical lamination theory. A test article was built to verify their models and then the PBP elements were implemented on flight vehicle. The flight vehicle had a wingspan of 1.4 m and was able to achieve "a 38% increase in roll authority .. compared to conventional ailerons" [14]. The PBP elements offered additional weight and power savings[14].

Other researchers have explored using shape memory alloy (SMA) devices. For example, Icardi and Ferrero investigated a system in which torsion SMA tubes actuated camber change[15]. This research centered on numerical studies to assess the feasibility of such a system. They looked at power required, weight, and ability to withstand aerodynamic load-

ing. The wing consisted of a box structure with flexible skin and an SMA tube connected to flexible ribs. Their studies showed that the system was able to provide adequate morphing without significant penalties in weight or power[15]. Peel et al. used Rubber Muscle Actuators with flexible elastomeric composite skins to create camber change[16].

2.4 Simulating UAV Aerodynamics

Because of the high cost of prototype fabrication, many researchers have turned to software and simulations for developing and analyzing aircraft. Turan[17] gives a thorough analysis of the different modeling techniques and software available for MAV design. He used a multidisciplinary, integration program called ModelCenter and developed a tool for the design of fixed wing MAVs. QPROP software was used for designing the propulsion while Athena Vortex Lattice (AVL) was employed for its capabilities with control and stability. He also evaluates the capabilities of other software such as Microsoft Excel, MATLAB, and the aerodynamic solver Digital DATCOM[17].

The Vortex Lattice Method employed by programs like AVL is a way to solve for aerodynamic forces and flow around a wing or airplane. Margason and Lamar [18] designed their own vortex lattice software. Their program is built in FORTRAN and is designed to solve for the flow around complex planforms. They provide details of how the solver works and its capabilities. Examples are given to further illustrate the workings of the program and of the vortex lattice method[18].

Grant [19] used AVL to design and model his mechanically morphing MAV. His MAV was designed to mimic the behavior of a gull which has a shoulder and elbow joints. The joints allowed him to mechanically adjust the sweep of the wings. As part of his effort, he used AVL to model and evaluate the complex shapes of the MAV. His simulations showed the capabilities of the aircraft in different configurations and allowed him to draw conclusions about the MAVs effectiveness in different scenarios[19].

Chapter 3

MFC Background and Wind Tunnel Testing Description

The section provides the background information on MFC technology and the wind tunnel experiments. The goal of the experiments was to evaluate current MFC airfoil designs. Building on previous research, a key objective was to quantify the aerodynamic benefit, if any, of the continuous control surface versus the conventional hinged technology. In theory, discontinuities create drag and reduce lift. In order to discern how significant this improvement is or even if it exists at all, 2-D wind tunnel testing was performed on several MFC-actuated airfoils and a conventional airfoil. This testing also examines the effect of changing the configuration of the airfoils. Two thin MFC airfoils and one thick MFC airfoil were tested. A thick conventional airfoil was tested to be a baseline for comparison. These airfoils were designed and fabricated by Gustafson[5] and researchers from AVID LLC., an aerospace research company. In addition, two airfoils were fabricated by rapid prototyping based on computer models of the conventional and MFC airfoils at full actuation. This section details the background of MFC structure, actuation, and hysteresis, and also includes the wind tunnel specifications, test article fabrication, and a description of the test equipment, and procedure. Much of this information is the work of other researchers and is

included here as background to understand the experiments and simulations that are bulk of the presented thesis.

3.1 MFC Background

This section details the piezoelectric technology behind the MFC-actuated airfoils including how the MFCs are actuated and implemented in the airfoils. The MFCs are advanced piezoelectric devices which have capabilities suited for application in morphing airfoils and wings.

3.1.1 Macro-Fiber Composites (MFCs) Description

Macro-Fiber Composites are piezoelectric actuators developed at NASA Langley Research Center[7]. They were fabricated to be inexpensive actuators which could produce large strains at relatively low-voltage. Due to the typically high voltage requirements of piezoelectric materials on the order of thousands of volts, piezoelectrics are usually judged on the strain they can create while minimizing voltage requirements. Their capabilities surpassed those of all existing piezoelectric actuators. Another benefit is that they are much more flexible than previous piezoelectric devices[7]. These characteristics make MFCs well-suited for application embedded in a composite airfoil. MFCs are flat, thin, rectangular actuators composed of a composite of piezoelectric fibers, epoxy, and copper electrodes. Specifically, their structure consists of rectangular PZT 5A fibers unidirectionally embedded in structural epoxy with copper electrodes on the upper and lower surface. The electrodes are interdigitated on a polymide film. Kapton tape is applied to the outside for environmental protection and insulation[7].

This particular structure is the key to the MFC success. The piezoelectric material is inherently brittle and inflexible but the fibers embedded in epoxy allow for significant deflection

and flexibility. Active Fiber Composites (AFCs) also use fibers embedded in epoxy[7]. However, AFCs use circular fibers whereas MFCs use rectugular ones[7]. Also, MFCs can create large strain with relatively low voltage because of how the electric field is implemented relative to the piezoelectric fibers. Piezoelectric materials have two primary actuation modes, d_{33} and d_{31}. The d_{33} mode is actuated when the electric potential is parallel to the fibers. On the other hand, the d_{31} mode is opposite and the electric potential is perpendicular to the fibers. Typically, the d_{33} mode is nearly two or three times more efficient than the d_{31} mode. The d_{33} mode allows for larger strains and larger applied voltages[20]. The interdigitated copper electrodes in the MFC create the electric field parallel to the fiber direction[20]. In addition, NASA Langley Research Center developed a method for very efficient, and thus relatively inexpensive, fabrication of the MFCs[7]. MFCs are now commercially available from Smart Material Corporation[20].

The focus of the research presented here is on the implementation of these actuators in embedded airfoils, thus much of the detail of the underlying physics is beyond the scope of this paper. For a more detailed discussion of the mechanics of piezoelectrics, readers are encouraged to read Wilkie et al. [7] or Williams [8]. Gustafson and Bilgen look at piezoelectric MFCs in regards to airfoil and wing applications[4][9][5].

3.1.2 Bimorph Description

The MFCs are implemented in the airfoils and wings in a configuration where the expansion and contraction of the actuators is transformed into a bending motion. This motion was chosen in part to maximize the actuator potential to affect aerodynamic control. The bending is similar to conventional control surfaces which have hinges to create the required camber change. In the simplest MFC configuration, the MFCs actuate to bend the trailing edge (TE) relative to the leading edge (LE) and thus create camber change.

It is possible to create a wing entirely of MFCs alone, but this is expensive and unnecessary. One method is to bond the MFCs to a substrate. The substrate can be the structure of the

wing and act as lever arm to amplify the strain of the actuator into larger TE deflections. The exact ratio of actuator surface area to total wing surface area is a design trade-off. More actuator area means more support to the deflection. Each actuator applies strain to maintain the new shape and in general the actuators are stiffer than the substrate so they provide stiffness as well. However, actuators are heavy relative to the substrate. Weight is a tremendous concern for aircraft and especially for small UAVs. If too many actuators are required, the weight could make MFC-actuation completely infeasible. The wind tunnel tests and finite element simulations presented in this thesis show some insight into this design trade-off.

One of the design choices is to use the MFCs in configurations called bimorphs. A bimorph is composed of two individual MFC actuators working in tandem. This is different than a unimorph which is only a single MFC bonded to the substrate. In a bimorph, one MFC is bonded to the upper surface and the other is bonded to the lower surface. Sometimes there is a substrate, as is the case for this research, but that does not always have to be true. The MFCs convert a voltage to expansion or contraction. A negative voltage causes contraction while a positive voltage causes expansion. In a bimorph, for downward curvature a negative voltage is applied to the bottom MFC in combination with a positive voltage applied to the top MFC. Thus, the top expands while the bottom contracts improving bending. The case of downward bending will be referred to as positive actuation for the remainder of this work. Figure 3.1 illustrates both positive and negative actuation of a bimorph.

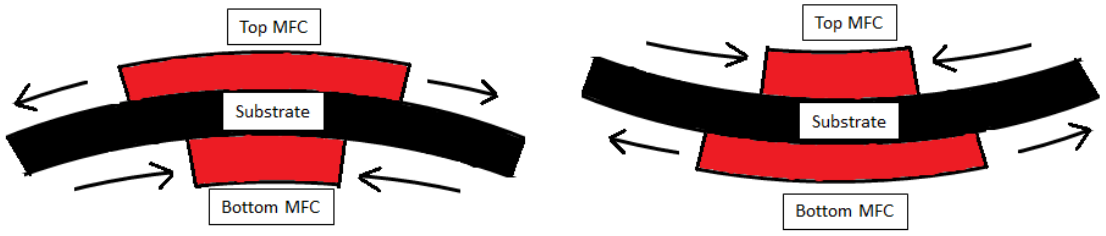

(a) Positive actuation (b) Negative actuation

Figure 3.1: Diagram showing bimorphs during positive and negative actuation

3.1.3 MFC Actuation

A piezoelectric material changes mechanically in response to an electric field. These materials have been used in many different applications particularly sensors and actuators. In a sensor, the piezoelectric material is subjected to a strain and outputs a voltage. The outputted voltage correlates with the applied strain. Because very small magnitude strains in a piezoelectric material create large voltages, a piezoelectric sensor can be very sensitive. Actual sensitivities can vary widely depending on the specific material and implementation[20]. Piezoelectric actuators work in the opposite way. When a voltage is applied, a strain is created in the piezoelectric. Typically in order to achieve an appreciable strain a significantly high voltage is required[7]. The reader is encouraged to see [8] and [20] for more details on the behavior and general physics associated with piezoelectric materials.

An MFC, like many piezoelectric devices, can function as both sensor and actuator. For the research presented here, MFCs were solely used in their capacity as actuators. The commercially available MFCs have a maximum operating voltage range of -500 to 1500 V. This range produces a maximum elongation on the order of $1400\mu\epsilon$[20]. For this research, as discussed previously, the MFCs were implemented in a bimorph configuration to maximize the bending effect[5]. Figure 3.2 shows the applied voltages to each MFC in bimorph from -100% to $+100\%$ actuation. A diagram of a thick airfoil at ± 100 is also shown in Figure 3.2 as an illustration.

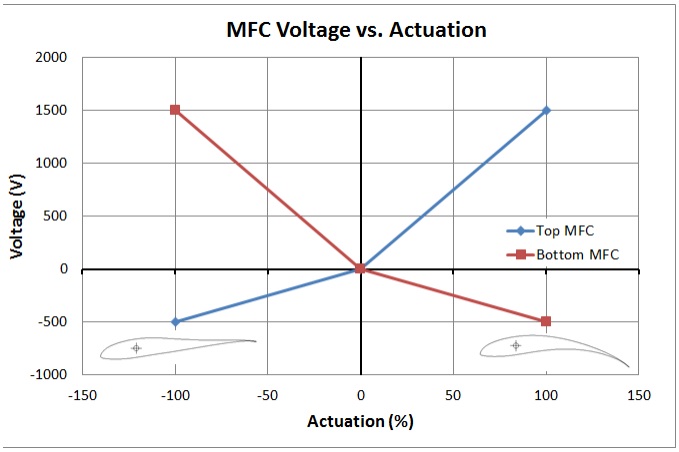

Figure 3.2: Graph of voltage applied to the MFCs versus actuation

For the purposes of this research and to be consistent with previous research and results[5], positive 100% actuation is defined as the case of maximum downward bending. For this case, 1500 V is applied to the top MFC which expands to its maximum while -500 V is applied to the bottom MFC which contracts to its minimum. Negative -100% actuation is the maximum upward bending. As the plot shows in Figure 3.2, 1500 V is applied to the bottom MFC causing maximum expansion while -500 V is applied to top MFC causing maximum contraction[5]. Figure 3.3 shows photos of a GenMAV airfoil in the wind tunnel under aerodynamic loading at +90% and -90%. The red dotted line was added for clarity.

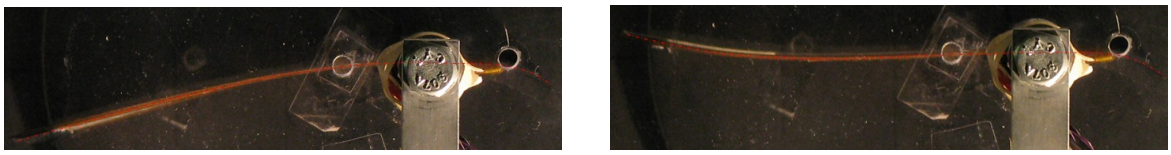

(a) +90% actuation (b) -90% actuation

Figure 3.3: Pictures of a GenMAV airfoil at +90% and -90% actuation

Due to the relatively large voltages required, actuating the MFCs is not a trivial problem. The goal of this research is to implement MFCs on small UAVs. If MFC actuated control surfaces can be a viable option, the MFCs have to offer some improvement over the current conventional control surfaces. The potential advantages such as better aerodynamics must

outweigh any disadvantages. Thus, one important characteristic for any system on a small UAV is weight. The entire MFC system should be of comparable weight or at the very least be as light as possible. This system weight includes any actuation circuitry and electronics the MFC needs. The large operating voltages means a significant voltage amplifier is needed in any control circuitry. In addition, because of the asymmetry in the MFC operating voltages, the control circuitry needs to support the asymmetric positive and negative voltages. However, as stated this circuitry must also be as light as possible. Several different circuits have been designed by previous researchers Bilgen and Gustafson which employ a single voltage amplifier[5]. A single input voltage is scaled to both the positive and negative sides of a bimorph. The circuitry was designed such that the input voltage was scaled to the positive three times more than to the negative. Thus, the maximum +100% input voltage is scaled to +1500 V and -500 V[5].

Two actuation systems are used in this research. The first system is not flight weight and was strictly for experimental laboratory tests such as the wind tunnel experiments and frequency response testing. This system will be referred to in this paper as the Trek system and consists of a Trek 623B high voltage amplifier with a custom circuit designed by Bilgen[9]. The Trek amplifier is a large unit that draws power from a standard wall outlet. An input voltage between -2 and 2 V is inputted into the Trek amplifier which sends the amplified voltage to the Bilgen circuit. The circuit then outputs the necessary asymmetric, high voltage MFC input to the bimorph. An input voltage of 2 corresponds to 100% actuation and the top MFC receives 1500 V while the bottom MFC receives -500 V. An input of -2 V results in -100% actuation. Everything in between is scaled appropriately[9].

The other actuation system uses flight-weight circuitry. This system is based on a custom circuit designed by Gustafson[5] for AVID LLC. The circuit runs on power from a 12 V constant input and accepts a variable input voltage between 0 and 5 V. The voltage output is based on this variable input. An input of 5 V is 100% actuation and the MFCs receive 1500 V and -500 V to the top and bottom MFCs respectively. With an input of 0 V, or -100% actuation, the top MFC receives -500 V while the bottom MFC receives 1500 V. This circuit

was contracted out to an electronics company AM Power Systems (AMPS) which made a flight-weight version of the circuit. The prototype was used in frequency response testing. This actuation system will be referred to as the AMPS board in this paper.

3.1.4 Hysteresis

One of the primary complications associated with piezoelectric actuators and sensors is an effect called hysteresis. Hysteresis is when the output of a system depends on the previous inputs in addition to the current input. The history of inputs determines what the current output will be. Hysteresis can be a significant problem for control systems. Ideally, when a certain input is applied to a system, the system will always return the same output. However, with hysteresis, the output becomes difficult to predict. The previous inputs affect the output, and thus a certain input could give significantly different outputs depending on the history. A possible controller becomes much more complex as it has to know how the history of inputs will impact the output. Previous researchers have studied hysteresis in regards to MFC actuation[8][9].

Unfortunately, MFCs, like most piezoelectric devices, exhibit hysteresis. MFCs form what are known as hysteresis loops. When the MFCs are actuated, their output depends on the maximum reached and whether the actuation is currently increasing or decreasing. Williams provides a good analysis and discussion of hysteresis in MFCs[8]. Hysteresis is an issue to both experimental testing and actual implementation in a UAV. First, for actual implementation, the UAV controller needs to be able to control the aircraft. In order to achieve this, it needs to be able to position the MFC actuated control surfaces. However, hysteresis and other non-linear effects make it difficult to know exactly how the MFCs deflect[6]. Several different methods have been proposed to account for this in the control algorithm. One method is to use a closed loop controller with feedback on the MFC deflection. The other method is to use an open loop controller with a feed-forward model of the hysteresis. In parallel with this present work, AVID LLC. developed an inverse hysteresis operator to

linearize the input/output relationship[6]. While these methods have shown success for vehicle implementation, the requirements for experimental testing are much less stringent. For experimental testing, the key is to implement a control scheme that can create consistent deflection between test runs. A laser can measure displacement and calculate the actual deflection in the post-processing of the data, but there needs to be consistent deflections so the test runs can be comparable. Fortunately, the hysteresis loops do allow consistent deflection[8].

The deflection of an MFC bimorph depends on which hysteresis loop the MFCs are in. Thus, given that the MFCs are in a particular loop, there is some degree of predictability to the output. Actuating the MFCs to maximum to a minimum then back to a maximum sets the MFCs to a particular loop and the previous history no longer affect the output [8]. This process of actuating the MFCs into a particular loop is referred to as zeroing in this paper. Other researchers including [5] and [9] have used this process. Without zeroing or knowing the history, a given actuation percentage could give an infinite number of different deflections. Once zeroed the MFCs output is limited to being on that maximum/minimum loop. Figure 3.4 shows a plot of the hysteresis loop of the zeroing process. The MFC bimorph was actuated from 0% to +90% then to −90% then back to +90%. The input is voltage while the output is TE deflection of the airfoil as measured by a laser. Descriptions of test equipment are available in Section 3.1.5.

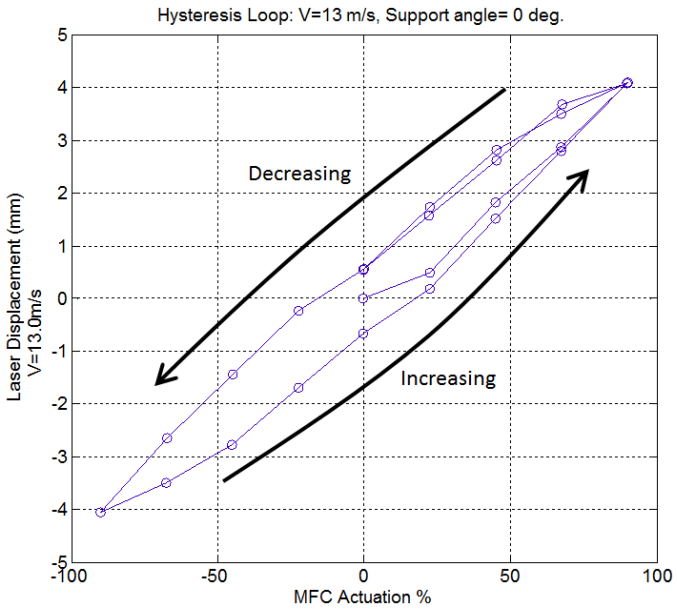

Figure 3.4: Graph of tip displacement versus actuation for zeroing process

As shown, the output is still not completely predictable even after zeroing. While the maximum and minimum actuation percentages give the same output no matter the input history, the actuation levels in between still show hysteresis. Each non-extreme input has two possible output values. For example in the above graph which was after zeroing, an input of 45% would give a tip deflection of approximately 2.7 or 1.7 mm. As shown in Figure 3.4, which output value occurs depends on whether the actuation percentage was increasing or decreasing. However, despite the remaining hysteresis effect, this process gives a means to achieve consistent deflections for experiments. As detailed in Section 3.2, zeroing was used in wind tunnel and frequency response experiments.

3.1.5 Wind Tunnel Description

The wind tunnel used for these experiments was a custom wind tunnel at the Center for Intelligent Material Systems and Structures (CIMSS) at Virginia Polytechnic Institute and State University. The wind tunnel was built by Bilgen as part of his doctoral research also

into MFCs for morphing wing technology. The details of the tunnel's construction and an evaluation of the wind tunnel is available in his dissertation[9].

Figure 3.5: Picture of CIMSS wind tunnel

Shown in Figure 3.5, the wind tunnel is an open circuit tunnel with a test section that is 136 mm tall by 365 mm wide. The test section is made of acrylic to provide a smooth surface and allow pictures to be taken during testing. Several access holes were available and installed with Pitot-static probes, pressure transducers, a thermocouple, and other assorted instrumentation. A full listing of the instrumentation installed during these wind tunnel tests in available in Table 3.1. The wind tunnel has flow straighteners at the inlet. Two large fans at the outlet pull air through the tunnel. The tunnel operates at speeds from 2 m/s to 22 m/s[9].

One of the most important capabilities of the tunnel as relevant to this research is to measure lift and drag forces on an airfoil. For these measurements, the wind tunnel includes a balance with two load cells. The balance, shown in Figure 3.6 consists of a C-arm attached to a rotary table. The rotary table sits on a two-directional u-joint. Two load cells are attached at the u-joint to provide measurements of lift and drag. As seen in Figure 3.6, the airfoil is rigidly installed in the balance and installed such that it does not make contact with test section structure. The rotary table is actuated with a stepper motor to allow the movement different

support angles which are defined in Section 4.1[9].

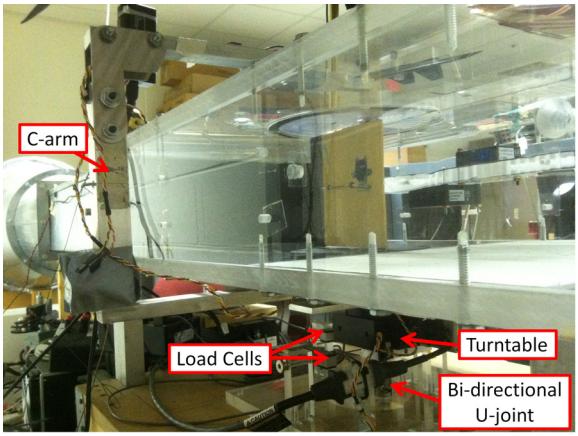

Figure 3.6: Picture of C-arm balance as installed on the wind tunnel

When lift and drag forces act on the airfoil, the forces provide a moment about the bi-directional U-joint. This moment is counteracted and recorded by the load cells. Knowing the distances between the midpoint of the airfoil and the u-joint and between the load cells and u-joint, the lift and drag forces can be calculated.

The wind tunnel is also equipped with electronics hardware and software for data acquisition and to control the different airfoils. A computer with LabVIEW is the user interface and the central processing hub. For data acquisition, a National Instruments digital aquisition (DAQ) card reads the data from the instruments and sends them to the computer. The DAQ has eight analog channels for recording experimental data. It also has output channels to send signals to the airfoils for actuation and other functions. The computer and DAQ system were capable of outputting signal voltages from -5 to 5 V required by the MFC actuation circuitry. The input voltage is sent to the Trek high voltage amplifier and then to the circuitry and MFCs. The system is also capable of outputting pulse width modulated (PWM) signals to control the servomechanism actuated airfoil. Table 3.1 gives a detailed list of the other instruments used in the tests[5].

Table 3.1: Instruments installed at the CIMSS wind tunnel

Output Channels	Instrument	Purpose
AO/0	Trek 623B High Voltage Amplifier	MFC actuation
D/3	Canon S5IS Camera	Test photographs
C/0	Servo Motor PWM	Servo actuation
Input Channels		
AI/0	Setra 267 Pressure Transducer	Static port pressure
AI/1	Omega CCT-22 Thermocouple Amplifier	Temperature measurement in test section
AI/2	Trek 623B High Voltage Amplifier	MFC actuation voltage measurement
AI/3	optoNCDT ILD1800-200	Laser displacement
AI/4	Dywer 668-5	Pitot-Static tube pressure
AI/5	Transducer Techniques MLP10, TMO-2	Lift measurement
AI/6	Transducer Techniques MLP10, TMO-1	Drag measurement
AI/7	Trek 623B High Voltage Amplifier	MFC actuation current measurement

3.1.6 Airfoil Descriptions

One of the primary goals of this study was to evaluate the aerodynamic performance of the MFC actuated airfoils. In order to accomplish this task, 2-D wind tunnel testing was done to compare MFC actuated airfoils to a conventional airfoil actuated by a servomechanism. In addition, different configurations of MFC-actuated airfoils were also fabricated and tested. As a basis of comparison, lift and drag coefficients were calculated as the airfoils underwent actuation percentage sweeps at various air velocities and angles of attack. This section details the specific configurations of each airfoil and how each was fabricated. The airfoils to be tested in this research are as follows: two thin composite MFC-actuated airfoils, one thick MFC-actuated airfoil, and one conventional, servo-actuated airfoil. The different thin and thick MFC airfoils were distinguished by the size and number of MFC actuators employed. The results of these tests were also compared to previously tested MFC-actuated airfoils from literature[5].

Thin MFC Airfoils

One of the MFC-actuated airfoil configurations to be studied is a thin composite airfoil with embedded actuators. A thin airfoil was chosen for several reasons. First, a thin airfoil offers a unique opportunity for the MFC technology. Despite some distinct advantages, thin

airfoils are not typically used in UAVs because it is difficult actuate thin control surfaces. Because embedding a servo inside a thin airfoil is impractical, a thin control surface requires long or complicated linkage mechanisms to transfer the servo movement to control surface movement. Complex moving parts hurt reliability and sustainability against environmental factors. Linkages can break or get caught in the environment. An embedded MFC actuator can be encapsulated within even a thin airfoil and have no moving parts or linkages[5].

The other reason to test thin airfoils is to compare against results from literature. The thin MFCs built and tested in this research were designed by Gustafson. In addition to the wind tunnel testing, he did a great deal of research into the composite structure and actuation of this airfoil design[5]. Working with AVID LLC., Gustafson also developed the fabrication method used in this research, and did much of the fabrication of the test articles.

The thin airfoils are referred to in this paper have a profile based on the GenMAV airfoil profile. The GenMAV UAV is a generic micro-aerial vehicle (MAV) developed by researchers at the Air Force Research Laboratory at Eglin Air Force Base and at Oregon State University. The purpose of this aircraft is to provide a baseline for developments in MAV and UAV technology. Stewart et al. saw that many researchers across the world were designing improvements and changes to MAVs and UAVs. The GenMAV aircraft was built as generic frame to compare these new improvements. The GenMAV wing uses a thin airfoil with a profile shown in Figure 3.7. The actual coordinates are listed are available in [5] or [10].

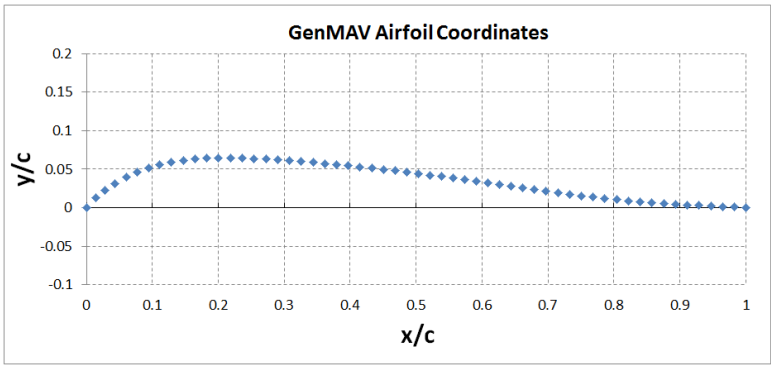

Figure 3.7: Plot of GenMAV airfoil profile coordinates normalized with the chord (c)

The GenMAV airfoils were constructed of composite materials specifically carbon fiber (CF) and electronic fiberglass (E-glass). Two types of CF were used: a 2 ply [0/90] weave and a uni-directional single ply . The E-glass was a [0/90] weave. The carbon fiber weave used was $6.6oz/yd^2$ while the uni-directional CF $6.0oz/yd^2$. The E-glass was $4.6oz/yd^2$. The composite properties of these materials are shown in Table 6.1. The ply schedule, how many layers and their orientations, was designed by Gustafson. He used finite element models and lamination theory to optimize the number of layers, material, and orientation. His work is detailed in [5]. He used his ply schedule, shown in Figure 3.8, to construct the GenMAV test articles used in these experiments. Building on this research, Chapter 7 in this thesis presents a detailed study of the effects of different ply schedule parameters on the morphing capabilities. Information in Figure 3.8 is from Gustafson[5].

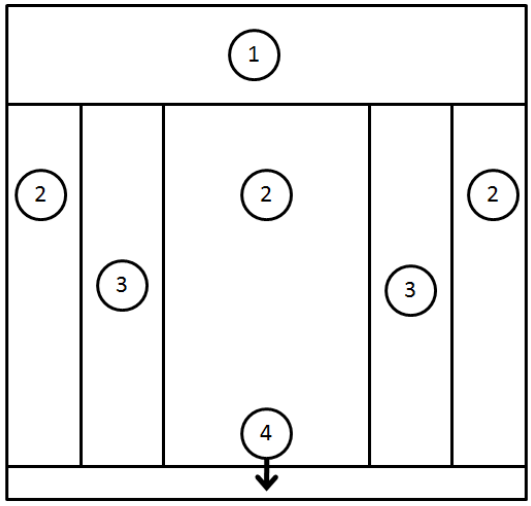

Figure 3.8: Diagram of the ply schedule for the GenMAV airfoils

The airfoils were built with a nominal 5.25 in. span and 5 in. chord. They were fabricated by first using a CNC machine to cut a mold out of wax. The mold was built to the coordinates of the GenMAV profile. The MFC actuators were properly wired and placed in the mold. Coupons of carbon fiber and fiberglass were cut from weaves and placed in their respective

orientations between the MFCs. The manufacturers information is available in The layup was then saturated with West System 105/206 Epoxy and cured overnight under vacuum. The airfoil was then cut to the proper chord and span direction. Threaded studs and wiring connectors were then attached to allow installation in the wind tunnel[5]. Figure 3.9 shows a GenMAV airfoil during and after fabrication.

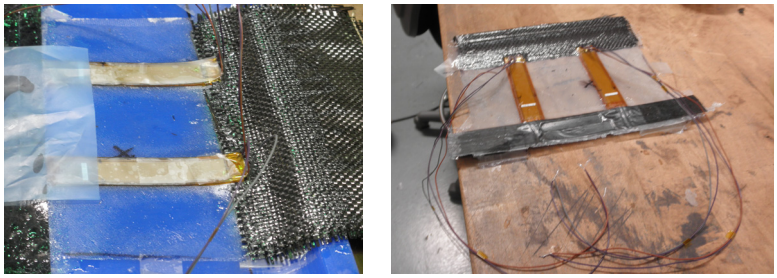

Figure 3.9: Pictures of a GenMAV MFC airfoil during fabrication

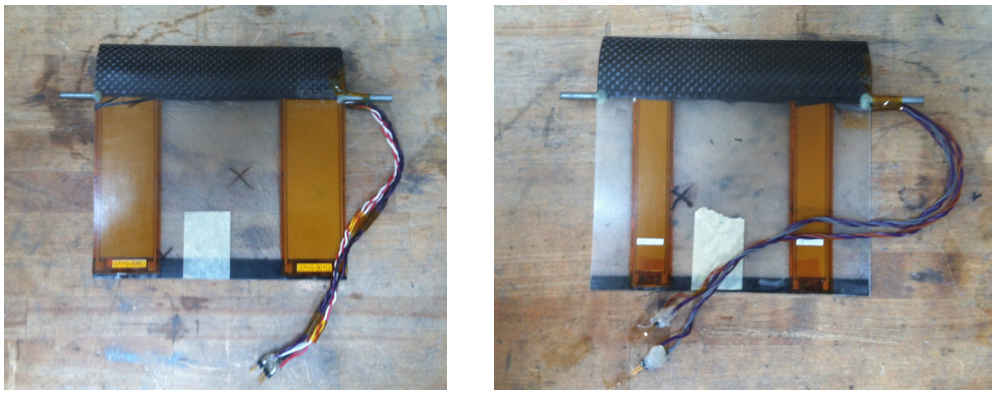

(a) 8528 (x2) (b) 8514 (x2)

Figure 3.10: Pictures of the 8528 and 8514 GenMAV MFC airfoils

Gustafson designed and fabricated two different airfoil configurations to be tested in addition to the airfoil discussed in his research. The differences between the airfoils are the number and size of MFC actuators employed. Smart Material Corporation sells several different MFC actuators which are designated by a number such as M8514 P1. The M indicates MFC while P1 designates the actuation mode. All the actuators used in this study are P1 and actuate as described in Section 3.1.3 so P1 is omitted in future references for simplicity. The

8514 means an actuator with an 85 mm long and 14 mm wide active area. An 8557 actuator would be 85 mm by 57 mm in active area[20]. Two airfoils were fabricated: one with two 8528 bimorphs located on the edges and one with two 8514 bimorphs located just offset from the edges. Two bimorphs consist of four individual MFC actuators. The exact dimensions are shown in Figure 3.11.

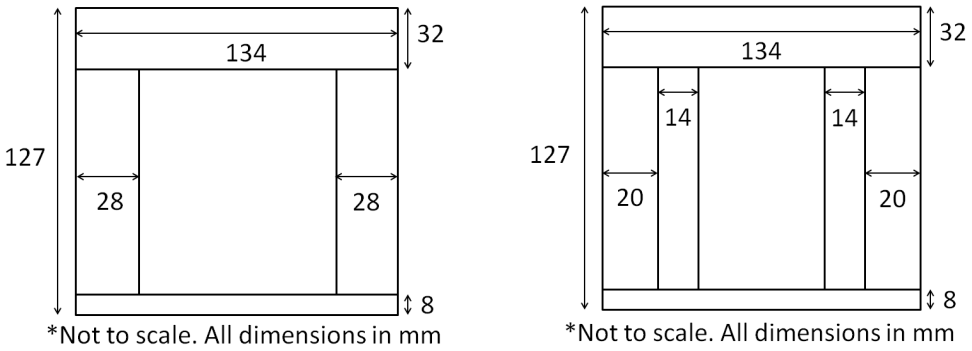

Figure 3.11: Diagram showing nominal dimensions of the GenMAV airfoils

Thick MFC Airfoil

The thick airfoil was designed and fabricated by AVID LLC. This airfoil was adapted from a Selig S1210 airfoil which is a low Reynold's number high lift airfoil[6]. An outline of the baseline airfoil profile and extreme actuation levels are shown in Figure 3.12. Information on the Selig airfoils are available from Selig et al. [21].

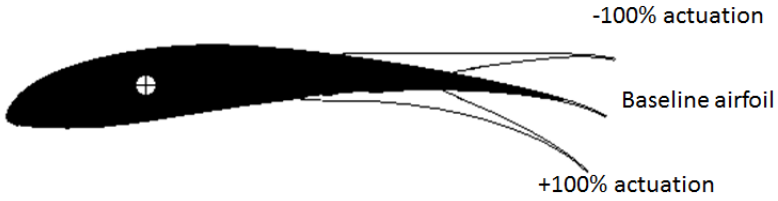

Figure 3.12: Profiles of the thick MFC Airfoil

The thick airfoil consisted of several components: a basswood D-box for the leading edge, a composite upper skin embedded with MFCs, and a composite lower skin which served as a

wiper. The D-box was carved from basswood by a CNC machine. Studs were installed for installation in the wind tunnel. The upper skin was composed of 1 ply of 3 oz/yd^2 fiberglass oriented ±45 deg., with a 0.5 in. wide 10 oz./yd^2 carbon fiber trailing edge stiffener. The MFCs were wired and aligned on the upper and lower surfaces of the upper skin. The layup was then cured. The thick airfoil was embedded with two 8514 MFC bimorphs located on the edges as shown in Figure 3.13. The lower skin was composed of 1 ply of 3 oz. fiberglass oriented ±45 deg. with an inner ply of isotropic carbon veil. The purpose of this skin was to be a wiper to maintain the airfoil profile[6].

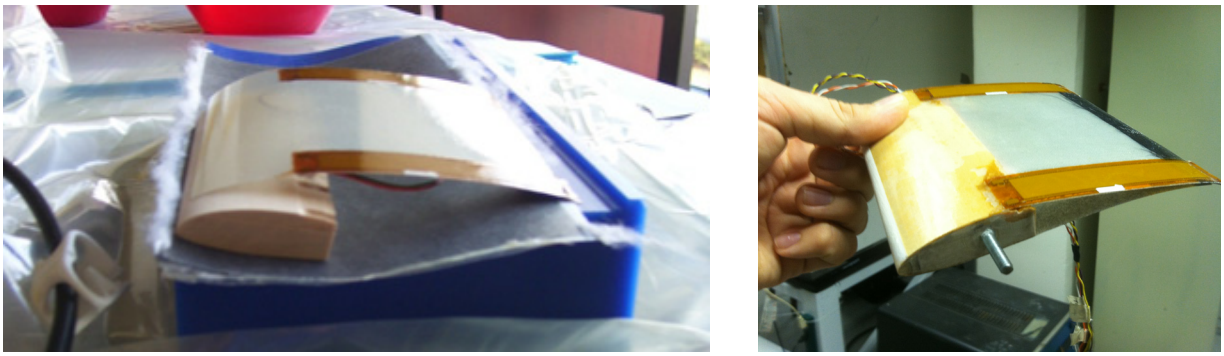

Figure 3.13: Pictures of the thick airfoil during and after fabrication. Images from [6] and used with permission

Servo Airfoil

The morphing technology is meant to be an alternative to conventional servo-actuated flapped mechanism. In order to assess the effectiveness, a conventional servo airfoil was built to be a comparison against the morphing airfoils. Ideally, the servo airfoil was built to be exactly the same as the thick MFC airfoil with the only difference being the actuation. This servo airfoil was designed and fabricated by AVID LLC. The airfoil was made entirely of basswood with a small hole in which a simple servo was placed. As shown in Figure 3.14, a small linkage converted the rotation of the servo into movement of the control surface. The servo is actuated from −100% to 100% by a pulse width modulation (PWM) signal.

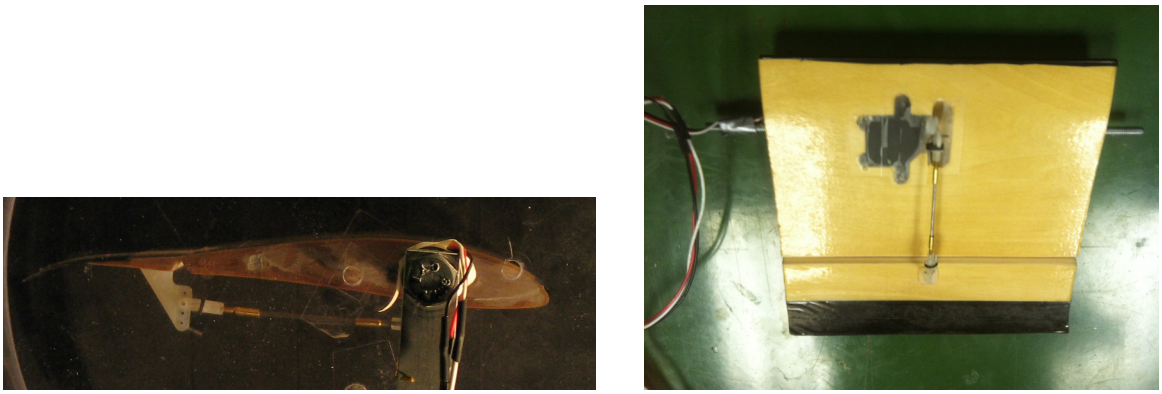

Figure 3.14: Pictures of the servo airfoil

The servo airfoil was built with a control surface that was 30% of the chord and linkages that were trimmed to actuate approximately ±20 deg. This configuration was chosen because it is typical of a conventional control surface, and roughly approximates the trailing edge deflection of any MFC. A servo could be designed for larger displacement and thus more range in lift and more control authority. A design choice was made to limit the deflection of the servo airfoil to approximately the same as the MFC deflection. This was done because the real interest is to compare the effects of a continuous vs. discontinuous airfoil, and MFC vs. Servo around operational range. Comparing the MFCs to each other, the range in lift and deflection was still considered. Figure 3.15 shows a comparison of the servo and MFC airfoils at maximum positive and negative actuation. The pictures are taken with the airfoils installed in the wind tunnel.

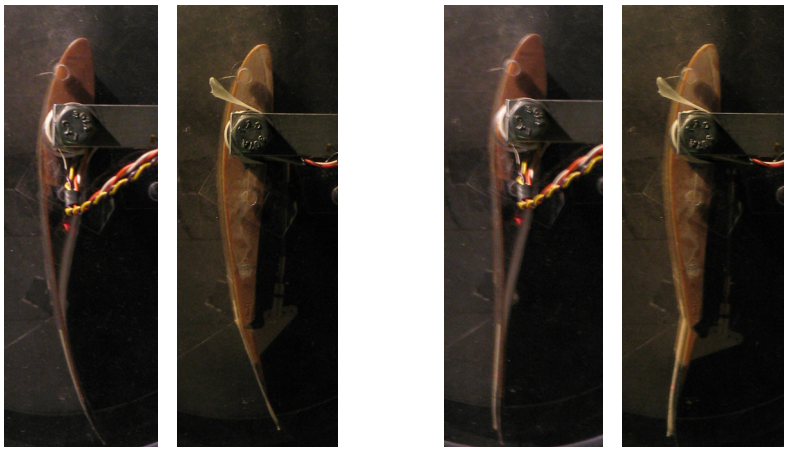

(a) MFC (b) Servo Maximum

(c) MFC (d) Servo Minimum

Figure 3.15: Pictures comparing the MFC and Servo deflections at the extremes of actuation

One of the advantages of articulated control surfaces is they can be designed to achieve almost any deflection including very large deflections. In contrast, the MFCs are relatively limited in what deflections they can create. However, the goal is not to compare the relative maximum range of lift coefficient of each type of airfoil. An aircraft would not necessarily benefit from this maximum, and would likely only need a small range for typical operational control authority. This research examines the effectiveness of each type of airfoil within this operational range. Thus, the servo airfoil's trailing edge displacement was limited as a design variable for the specific comparison of servo vs. MFC technology. This was justified with the understanding servos hold a distinct advantages for applications where maximizing the lift coefficient range is important. However, maximizing TE displacement and range in coefficient of lift was examined in comparing among only the different MFC airfoil configurations. The trade-offs and considerations involved in maximizing MFC TE displacement is one of the major topics of this research. It is discussed in detail in both the MFC wind tunnel results of Chapter 4 and finite element analysis presented in Chapter 7.

3.2 Wind Tunnel Experimental Procedure

The goal of the wind tunnel testing was to determine how the lift and drag coefficients are affected by the actuation. Each airfoil underwent a full cycle of actuation from 100% actuation to −100% actuation at a series of different flow conditions. An actuation cycle was done at several different support angles and at different flow speeds. The specific actuation levels, support angles, and wind velocities are listed below. After installation, most of the experiment was cycled through automatically using a LabVIEW program developed by Gustafson[5]. The exact procedures are listed below[6]:

1. Record tare data from load cells at each support angle
2. Manually set wind velocity using readings from pressure sensors
3. Automatically cycle through specified range of support angles

   At each support angle:

   a) Zero hysteresis (MFC airfoils only)

   b) Cycle through each specified actuation level or flap angle

   c) Wait 5 sec. at each step to allow settling

   d) Collect data from all channels for 5 sec.

4. After data collected at all support angles and actuation levels, turn off wind and take a second tare
5. Repeat from step 2 with next wind velocity

All airfoils underwent testing at wind tunnel speeds of 9 m/s, 13 m/s, and 17 m/s, except the rapid prototyped (RP) airfoils. The RP wind tunnel testing is described in Section 4.8. The Reynolds numbers for the three wind speeds were approximately 7.3×10^4, 1.1×10^5, and 1.4×10^5. At each wind speed, the airfoils were tested at support angles of -5 deg. to 15 deg. with 2.5 deg. increments. Support angle is defined in Section 4.1. At each support angle,

the MFC airfoils were actuated from +90% to -90% and back to +90% at 22.5% increments. The servo airfoil was actuated from -20 deg. flap angle to +20 deg. flap angle at increments of 5 deg. at each support angle.

The data was processed by first subtracting the mean of the two tare data sets from the data collected in step 3d. The data was then converted to engineering units. Force data from the lift and drag load cells was then converted into sectional lift and drag coefficients, C_l and C_d respectively, according to Equation 3.1 below. Data from all channels was averaged from at each collection step.

$$C_l = \frac{L}{0.5\rho V^2 A} \qquad C_d = \frac{D}{0.5\rho V^2 A} \tag{3.1}$$

Where V is wind velocity, A is the airfoil area, ρ is the air density, L is the induced aerodynamic force perpendicular to the flow, and D is the aerodynamic force in the flow direction.

For the MFC airfoils, due to hysteresis, there are two unique values for deflection at each actuation percentage. Thus, there are also two unique values for C_l and C_d at each actuation point depending on whether the actuation was increasing or decreasing for a given hysteresis loop. Unless noted, all plots presented in Chapter 4 represent the decreasing value of C_l and C_d from the two data sets. Maximum and minimum actuation points are unaffected by hysteresis, and are the same for increasing and decreasing actuation[6]. A small wind tunnel correction was included to account for flow blockage by the airfoil. The details of this correction are available in Gustafson[5].

Chapter 4

Wind Tunnel Results

This section presents the results from the wind tunnel experiments. Each airfoil discussed in Section 3.1.6 underwent testing as described in Section 3.2. For each, the coefficient of lift and drag were calculated at each test point and plotted. The results are organized by airfoil with the figures and then the conclusions. First, the GenMAV airfoil results are presented followed by the thick MFC and servo airfoils. As described in the following sections, additional experiments were deemed necessary to fully investigate the aerodynamic differences between the continuous and discontinuous control surfaces. Two airfoils, a flapped and morphing version, were rapid prototyped based on computer models of the maximum deflection for each. The airfoils do not actuate and are intended to remove all variables to isolate the continuous vs. discontinuous effects. Section 4.8 describes the details of the motivation for the rapid prototyped airfoils, their fabrication, and the results of their wind tunnel experiments. Conclusions are drawn from all the wind tunnel tests about the design trade-offs and capabilities of the morphing control surfaces. Experimental uncertainty is discussed in Appendix A.

4.1 Definition of Support Angle and Calibration

The purpose of this section is to define an important parameter called support angle, β, which is necessary to better understand the wind tunnel results presented in the next few sections. Here the support angle is defined as the angle between the free stream wind velocity and the airfoil chord at zero actuation and zero loading. This angle, shown in Figure 4.1 is constant at all levels of airfoil control surface actuation and is controlled by the rotation of the airfoil and C-arm assembly on the rotary table. At zero actuation, the support angle is equivalent to the true angle of attack, α[6]. The angle of attack is defined as the angle between the free stream velocity and the chord line, which is defined by the leading edge and trailing edge points[22]. However, as the control surface actuates, the angle of attack changes as the trailing edge deflects up and down due to morphing. The support angle allows for simpler comparisons between different initial angles to the flow without the additional complication of a changing angle of attack. Most figures in this paper use support angle as an independent variable. The support angle can be thought of as the angle of attack of the aircraft or the incidence angle of a wing on an aircraft. The local angle of attack changes with actuation, but the support angle does not. The pictures in Figure 4.1 show the support angle, β, for the thick MFC airfoil. The support angle and angle of attack are defined in the same manner for the GenMAV airfoils.

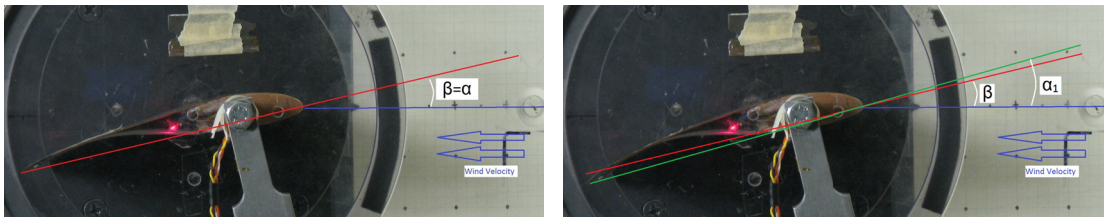

(a) Zero Actuation (b) Postive Actuation

Figure 4.1: Pictures illustrating the difference between support angle, β, and true angle of attack, α

After data collection, a calibration was done on the thick MFC airfoil to investigate the relationship between the support angle, actuation percentage, and angle of attack. The

calibration allows the calculation of the local angle of attack from a given control surface actuation and support angle for the thick MFC airfoil. Calibrations for the other MFC airfoils can be calculated, but will be similar to that of the thick MFC airfoil. This calibration was found by looking at wind tunnel data from the thick MFC run with the wind speed at 13 m/s. As discussed in Section 3.2, at each support angle, the airfoil was actuated through an entire hysteresis loop, 100% to −100% back to 100%. Figure 4.2 shows the calculated angle of attack at four different support angles across the entire actuation cycle. The true angle of attack was measured by examining the pictures at each actuation. During testing, at each data actuation level, a photograph was taken from above. Two of these photos are shown in Figure 4.1. For each digital photograph, a pixel that represented the leading edge and one on the trailing edge were manually selected. A computer program then calculated the true angle of attack from the location of these pixels. Thus, the true angle of attack can be found for a particular actuation level and support angle from the photograph.

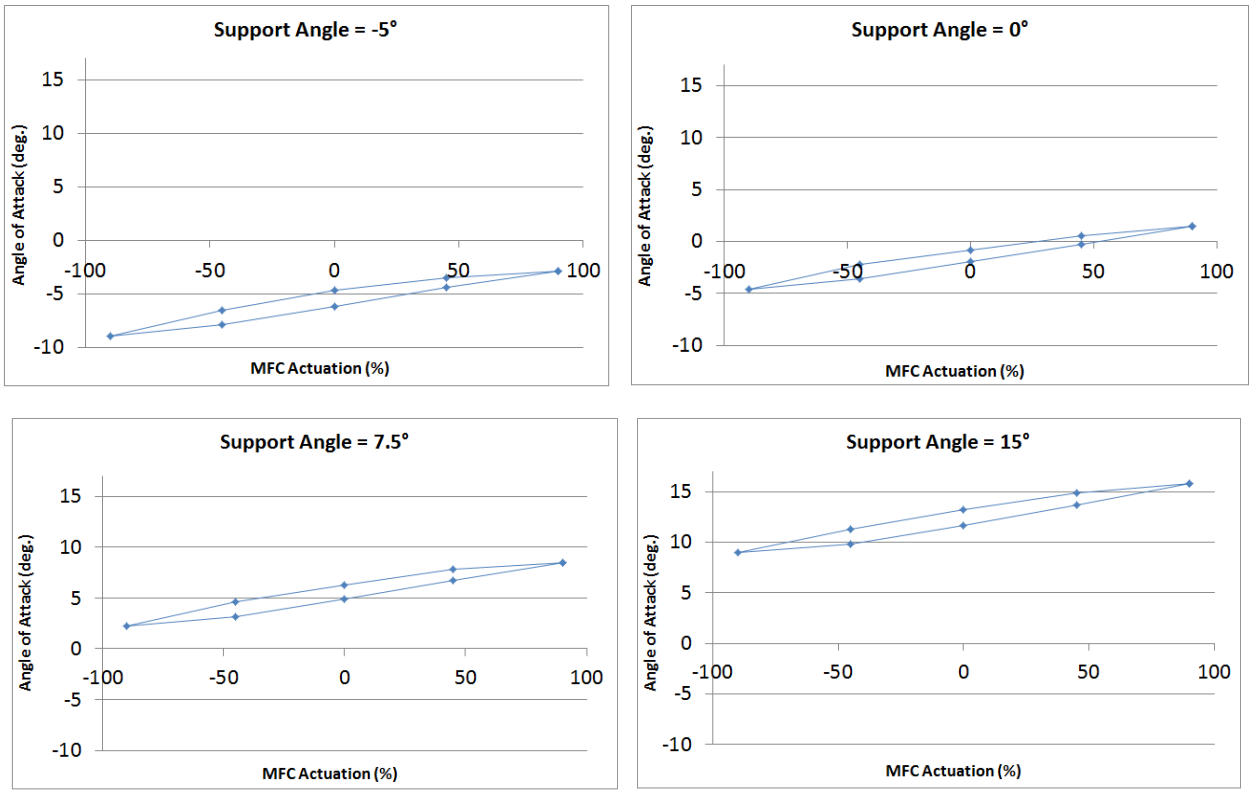

Figure 4.2: Calibration of local angle of attack from support angle and actuation at 13 m/s for the thick MFC airfoil

From the data in Figure 4.2, the angle of attack varies by approximately 6° with actuation depending on support angle. A few additional important conclusions can be gleaned from the plots in Figure 4.2. First, because hysteresis affects deflection, it also has a noticeable effect on true angle of attack. From the hysteresis loops, angle of attack is approximately 1° to 2° different depending upon whether actuation was increasing or decreasing. This is a sizeable difference in angle of attack that could affect control. The effect of hysteresis is explored in more depth in Section 4.5 with regards to the wind tunnel results.

Another key feature in Figure 4.2 is the effect of dynamic pressure. The MFC airfoil is inherently flexible in order to ensure the MFC actuators can create sufficient displacement and camber change. However, this flexibility means dynamic pressures can create airfoil profile changes and reduce the MFC actuated displacement. Thus, the airfoil deflection

becomes a function of dynamic pressure which is affected by factors such as airplane angle of attack and wind speed. A control surface that is dependent in this way complicates the aircraft flight control algorithm and compromises the practicality of the morphing technology. Looking at the plots in Figure 4.2, the angle of attack loops are not centered on the given support angle. This is particularly evident as the support angle increases. From the definition of support angle in Figure 4.1, the angle of attack and support angle should be equivalent when the actuation is zero. However, at 15° support angle for example, zero actuation corresponds to an angle of attack of 11.6° and 13.2°. The entire hysteresis loop is shown, thus there are two values depending on whether the airfoil was increasing or decreasing. At 7.5° support angle, zero actuation corresponds to an angle of attack of 6.3° and 4.9°. This difference is due to deflection caused by dynamic pressure loadings. The load on the airfoil is a function of lift and drag which is maximum at 15° and correspondingly the 15° data shows the highest effects. At −5° support angle, the airfoil camber becomes more stream line with the flow and as expected the dynamic pressure has the smallest effect. In fact, the effect is small enough such that the angle of attack data points are centered around −5° where they would be under no aerodynamic loading. The aeroelastic effects involved with MFC technology is one of the central points of investigation in this thesis and is discussed in more detail in both the wind tunnel results and finite element simulations.

4.2 8528 MFC GenMAV Airfoil Results

This section presents the results from the 2-D wind tunnel testing on the GenMAV airfoil embedded with two 8528 bimorph actuators. The sectional lift coefficients are shown in Figure 4.3 while the sectional drag coefficients shown in Figure 4.4. The coefficients were plotted against support at each level of actuation and each wind speed. The data shown is from the decreasing side of the hysteresis loop. This means the coefficients were from when the airfoil was at the higher deflection state at each actuation level. Thus, this represents the best case of the two hysteresis states for lift and the worst case for drag. The difference

between the two hysteresis states is quantified in Section 4.5.

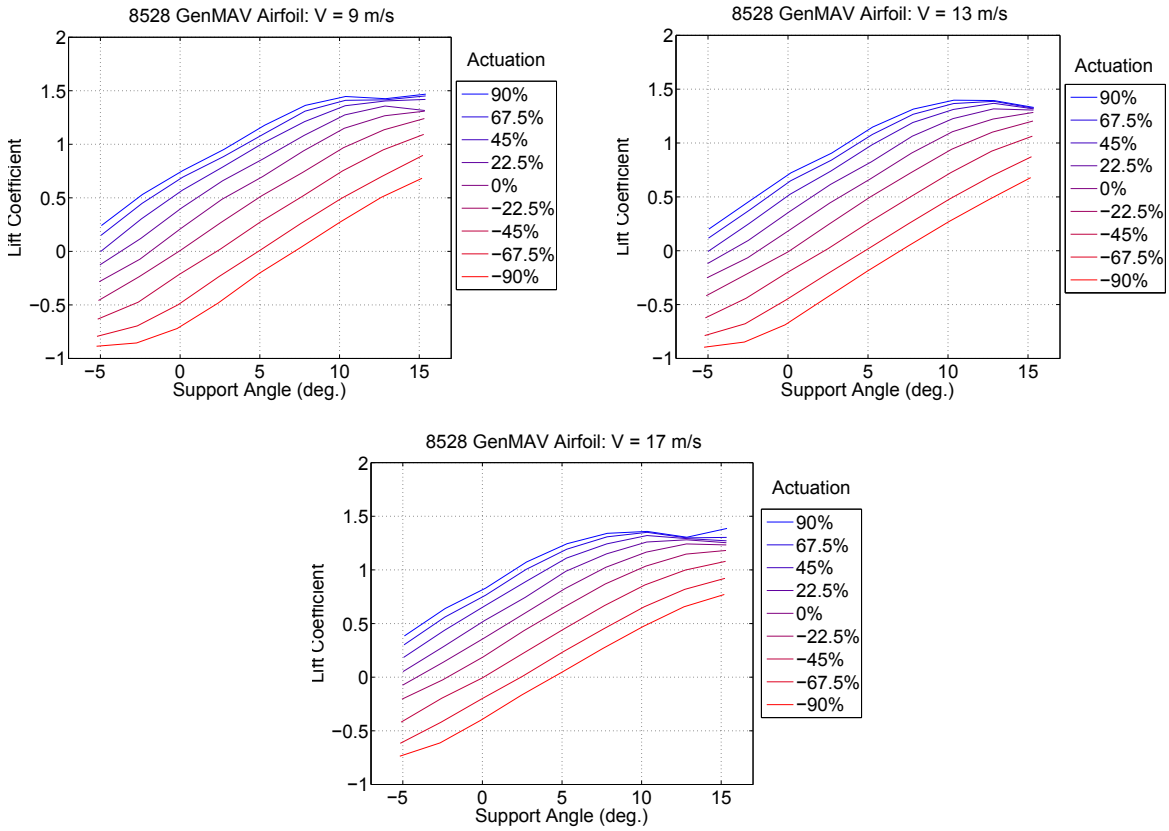

Figure 4.3: Lift Coefficient vs. Support Angle for the 8528 GenMAV airfoil at wind velocities of 9, 13, and 17 m/s.

As Figure 4.3 shows, the 8528 GenMAV airfoil achieves an adequate range of C_l for each wind speed. For 9 m/s, at a support angle of 5°, the C_l ranges from -0.20 to 1.17. However, this range decreased to -0.19 to 1.15 for 13 m/s and then to 0.05 to 1.25 for 17 m/s. The decrease in range is a result of the increased aerodynamic loading. The dynamic pressure works against the MFC actuation and reduces the airfoil deflection. Interestingly, for 17 m/s at the 5° support angle, the lower limit of C_l was most affected by the aeroloadings while the upper limit actually increased slightly. The upper limit increase is not very significant and could be due to experimental error, which is discussed in Appendix A. Also, the increase can be due to the increase in camber that occurs when the airfoil is loaded up. However, the effect on the lower limit however is significant. The large difference is likely because at

-90% the airfoil is trying to bend up into the flow and an area of higher dynamic pressure. Overall, the effect of the changing aerodynamic loading is relatively small, and the airfoil maintains enough range in C_l for UAV control authority at all three wind speeds.

The C_l curves also illustrate the effect of actuation on stall angle. The 90% actuation cases show signs of stall near a support angle of $9-13°$ while -90% actuation cases do not even at 15° support angle. Thus, increasing actuation decreases the stall angle. This effect makes sense and agrees with previous MFC airfoil results[5].

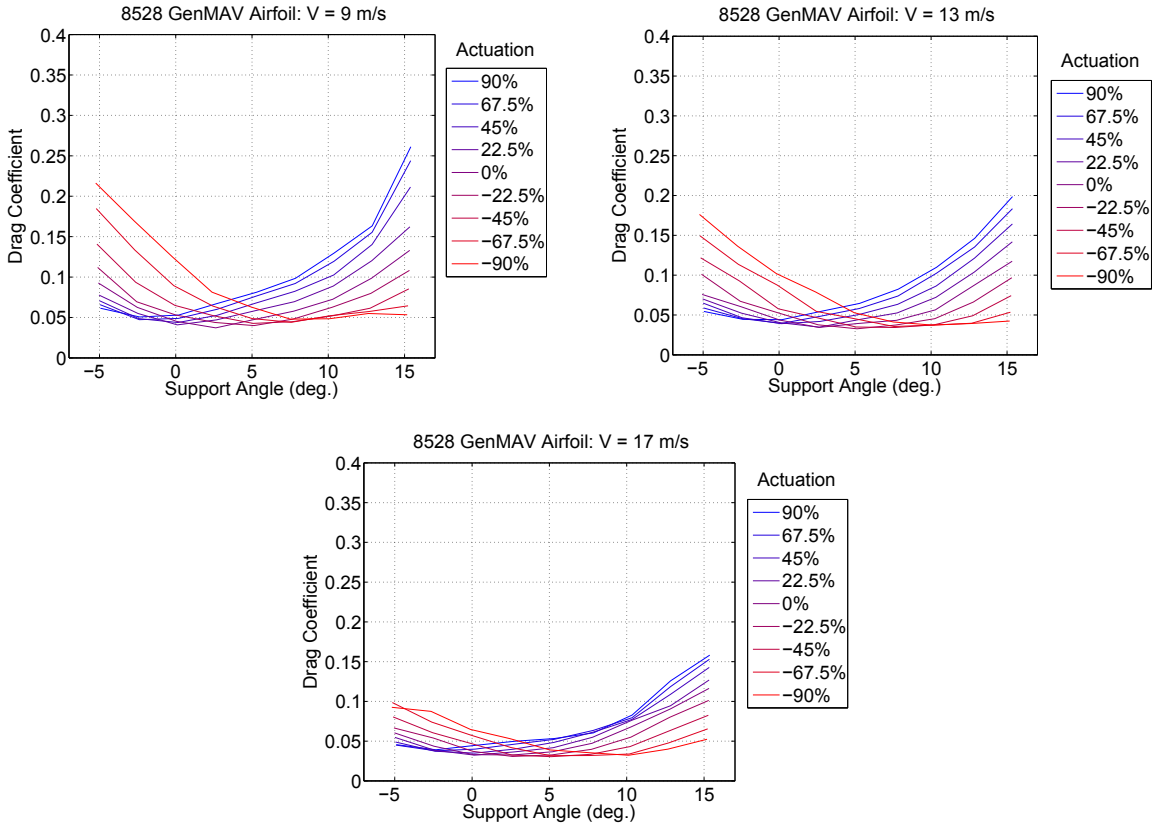

Figure 4.4: Drag Coefficient vs. Support Angle for the 8528 GenMAV airfoil at wind velocities of 9, 13, and 17 m/s.

For the drag coefficient plots in Figure 4.4, the drag range also decreases with increasing wind speed. At a support angle of 5°, the range in drag was 0.04 to 0.08 at 9 m/s and 0.03 to 0.05 at 17 m/s. Not only did the range decrease, the overall values of drag coefficient decreased

with increasing wind speed. This follows as the larger deflection at low wind speeds creates more impedance to the flow and thus more drag. In general the drag values are a bit higher than might be expected. This is likely an effect of the wind tunnel and possibly surface roughness and has been documented by Bilgen [9] and Gustafson[5].

4.3 8514 MFC GenMAV Airfoil Results

This section presents the results for the 2-D wind tunnel testing on the GenMAV airfoil embedded with two 8514 MFC bimorphs. The plots show the data from decreasing side of the hysteresis loop which is the best case for lift and worst case for drag.

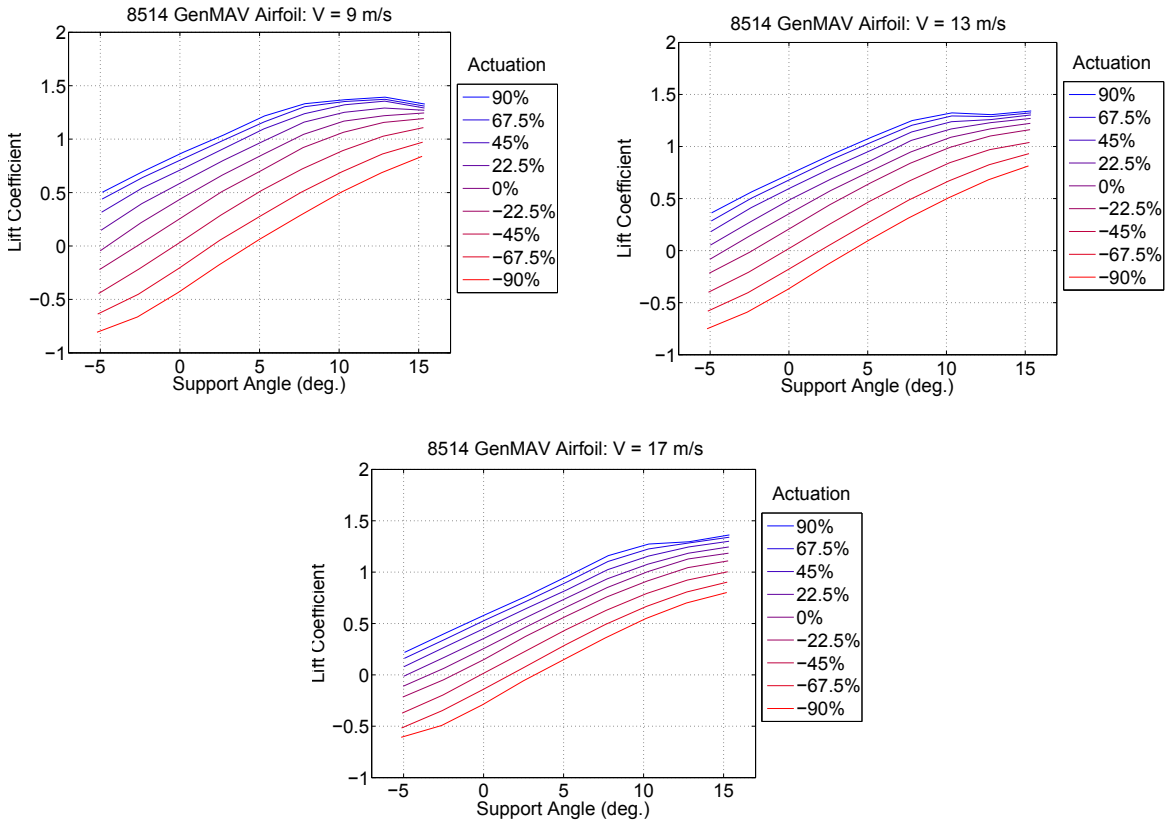

Figure 4.5: Lift Coefficient vs. Support Angle for the 8528 GenMAV airfoil at wind velocities of 9, 13, and 17 m/s.

Figure 4.5 shows the sectional lift coefficients vs. support angle for the three different wind speeds and at all actuation levels. The range in C_l is adequate for control authority for all three wind speeds. However, it is interesting to note the reduction in range with increasing wind speed. At a support angle of 5°, the C_l ranged from 0.06 to 1.22 for 9 m/s, 0.10 to 1.09 for 13 m/s, and 0.15 to 0.96 for 17 m/s. These represent sizable reduction. The C_l at 90% actuation was reduced 20% in going from 9 m/s to 17 m/s. In general, the GenMAV airfoil with 8514 MFCs still maintains adequate control authority.

Comparing to the GenMAV airfoil with 8528 actuators, the GenMAV airfoil with 8514 actuators is more sensitive to the changes in wind speed. At a support angle of 5°, the C_l range of the 8528 airfoil decreased by approximately 12% while the C_l range for the 8514 airfoil decreased by 30%. The difference is likely due to the simple fact that the airfoil with 8528 MFCs has a higher ratio of MFC area to total area. The MFCs provide the bending force and are stiffer relative to the fiber glass substrate against the aeroloads. The increased sensitivity of the 8514 GenMAV airfoil could present a challenge to aircraft control as the effect of the control surfaces becomes dependent on wind speed.

At 9 m/s, the maximum C_l values were comparable for the two airfoils, but the 8528 GenMAV had improved range for all speeds and was better able to minimize the effects. The trade-off is the increased weight due to the heavier MFCs. The 8528 GenMAV airfoil weighed approximately 36.9 g while the 8514 GenMAV airfoil only weighed 28.4 g. This weight savings could be worth the aeroelastic drawbacks.

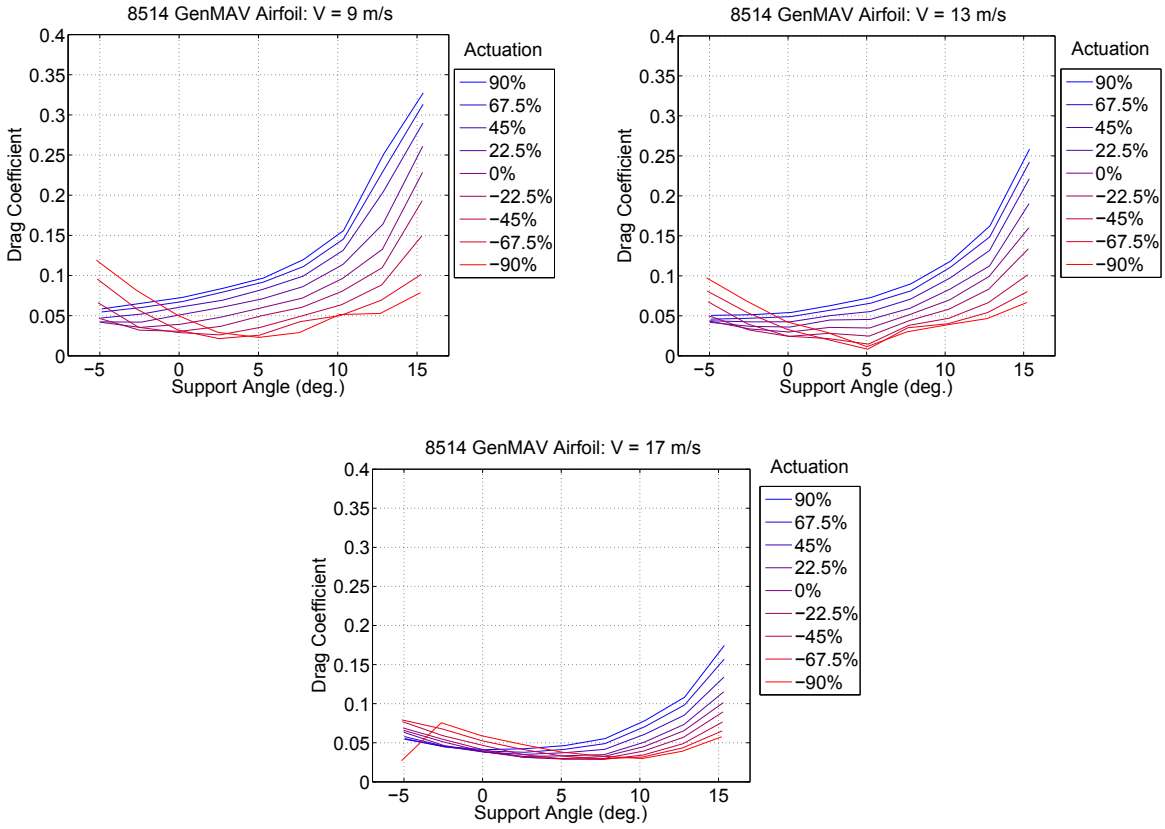

Figure 4.6: Drag Coefficient vs. Support Angle for the 8528 GenMAV airfoil at wind velocities of 9, 13, and 17 m/s.

Figure 4.6 shows the sectional drag coefficient for 8514 GenMAV airfoil. At a support angle of 5°, the range in drag coefficient was 0.02 to 0.10 for 9 m/s while 0.03 to 0.05 for 17 m/s. Overall, the drag is comparable to the drag from the 8528 GenMAV airfoil. The GenMAV airfoil with 8514 MFCs achieved a lower minimum drag but a slightly larger range over each wind speed. However, the relatively small changes and large experimental error make it difficult to conclude that there are any significant differences between the drag coefficient data of the two airfoils.

4.4 Thick MFC Airfoil Results

This section presents the results for the thick MFC airfoil. This airfoil is based on a Selig 1210 profile and is embedded with two 8514 MFC bimorphs. The profile is maintained by a wiper as the lower surface which moves with the upper surface. As was done with the other MFC airfoils, the data from the decreasing hysteresis loop was presented.

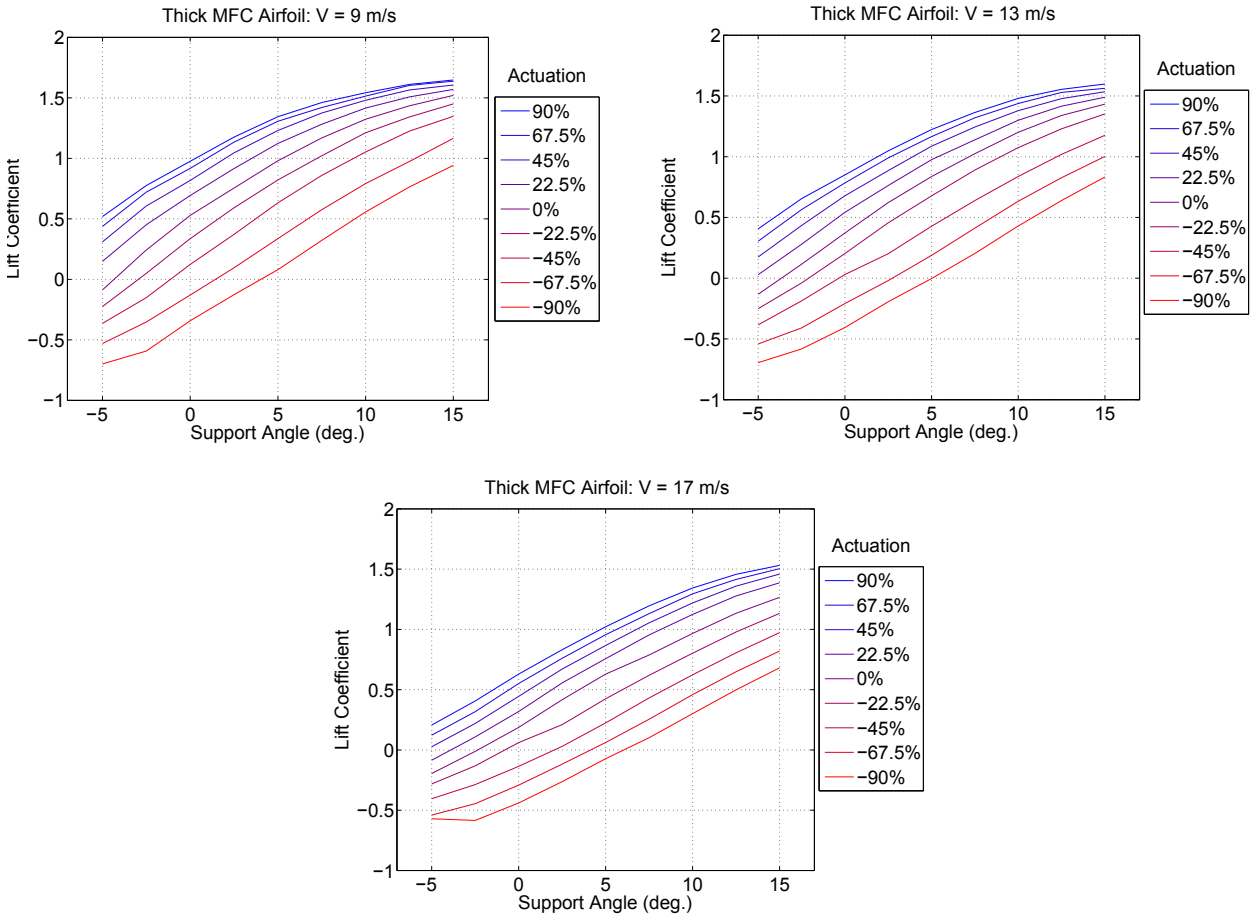

Figure 4.7: Lift Coefficient vs. Support Angle for the thick MFC airfoil at wind velocities of 9, 13, and 17 m/s.

From Figure 4.7, the range in sectional C_l for the thick MFC airfoil at a support angle of 5° was: 0.08 to 1.35 for 9 m/s, 0.04 to 1.15 for 13 m/s, -0.08 to 1.03 for 17 m/s. The C_l range was increased comparing to the GenMAV airfoil also with two 8514 bimorphs for all three

wind speeds. At 13 m/s, the GenMAV airfoil's C_l range was 0.99 while the thick airfoil's range was 1.11. The thick airfoil also displayed a decreased susceptibility to deflections from aerodynamic loading. Going from 9 m/s to 17 m/s, the C_l range of the thick airfoil only decreased by 13%. The difference could be due to the lower surface wiper which was able to support some of the aeroloads.

In addition to increased range, the thick airfoil also achieved higher values for lift coefficient. The maximum values of C_l at each of the three wind speeds for the thick airfoil were: 1.65 for 9 m/s, 1.57 for 13 m/s, and 1.53 for 17 m/s. The respective maximums for the 8514 GenMAV were: 1.39, 1.36, and 1.34. The thick airfoil also had a larger stall angle with only the 9 m/s test case showing stall at a support angle of 15° and near maximum actuation. At all three wind speeds, the GenMAV airfoil showed signs of stall near maximum actuation around a support angle of $10 - 15°$.

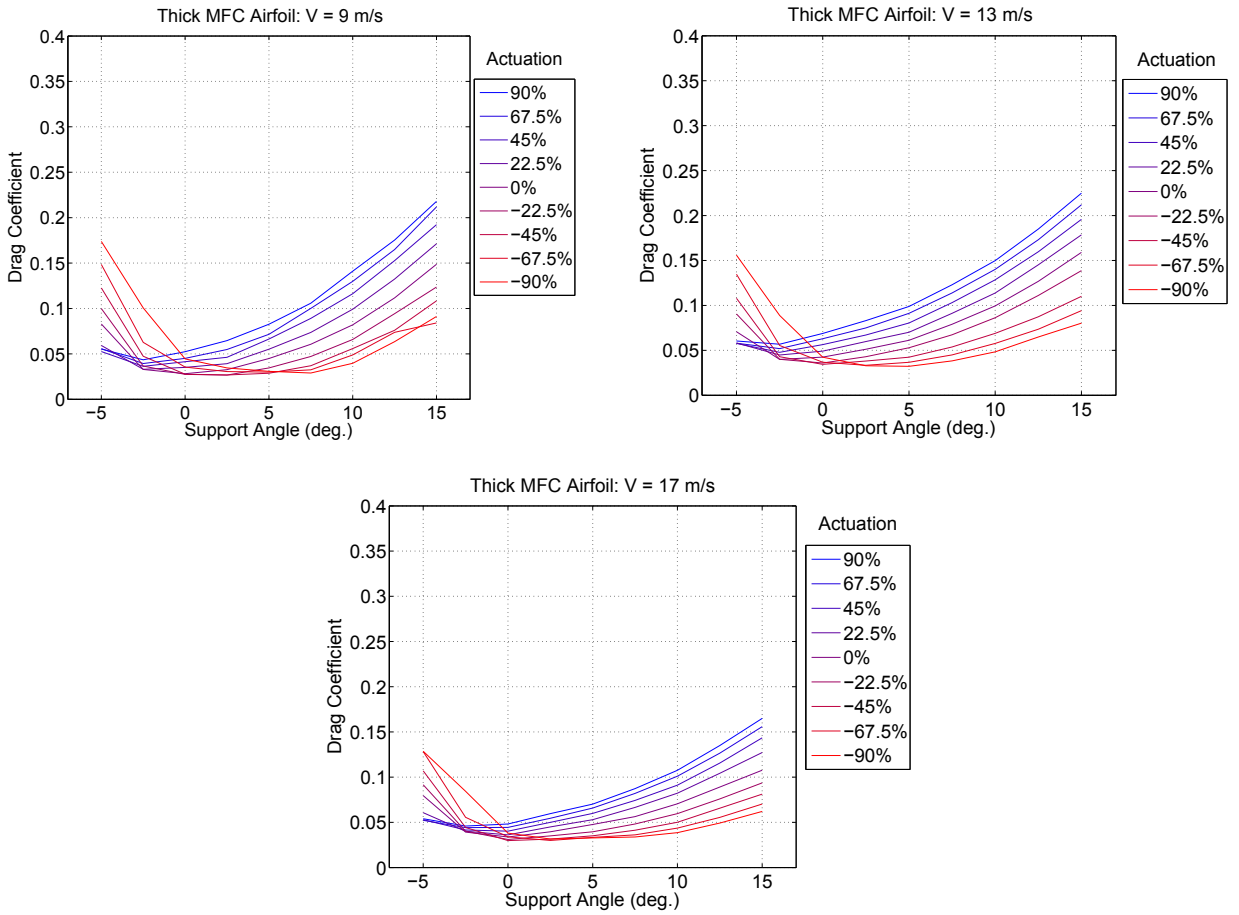

Figure 4.8: Drag Coefficient vs. Support Angle for the thick airfoil at wind velocities of 9, 13, and 17 m/s.

From Figure 4.8, the sectional drag plots show similar trends that have characterized other MFC airfoils, like the decrease in drag with wind speed. Comparing to the GenMAV airfoil with 8514 MFCs, the drag was lower with the thick airfoil for the 9 m/s and 13 m/s test cases. For 9 m/s, the GenMAV maximum drag coefficient was 0.33 while the maximum drag coefficient for the thick airfoil was 0.22. The 17 m/s test case had comparable drag between the two airfoils.

4.5 Hysteresis Effects on C_l and C_d

One of the simplifications that was made for many of the plots in this chapter was to only present the decreasing half of the hysteresis loop. As a reminder, at each wind speed and at each support angle, the MFCs were actuated from +90% down to -90%, the decreasing half, and back to +90%, the increasing half. The decreasing half represents the best case for deflection, which is the best case for lift and worst case for drag. This section quantifies and discusses the difference between the decreasing and increasing loops for lift and drag coefficient. The test case that is presented is the thick airfoil with 8514 MFCs at a wind speed of 13 m/s. The other airfoils also could be examined, but the hysteresis differences are comparable to the thick airfoil. The 13 m/s test case was chosen because it is the middle wind speed. The effects of wind speed follow the same trends discussed previously.

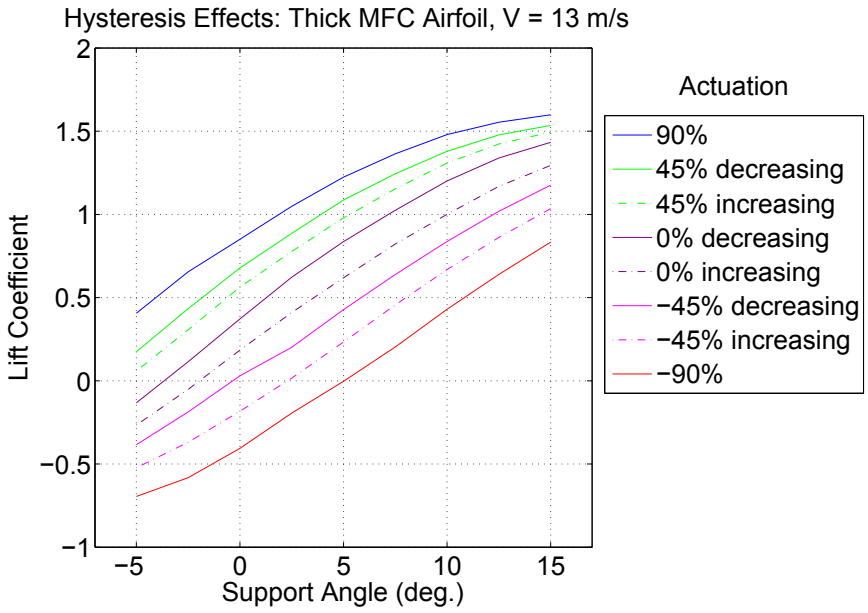

Figure 4.9: Effects of hysteresis on the lift coefficient for the thick MFC airfoil at 13 m/s

Figure 4.9 shows the sectional lift coefficient for the thick MFC airfoil at 13 m/s. Only the a few representative actuation levels are shown to better visualize the effects. The solid lines from the decreasing data are same data from Figure 4.7. The dotted lines show the data

from increasing half of the hysteresis loop. The maximum values have only a single value and there is no increasing or decreasing. They are shown as a reference.

As Figure 4.9 illustrates, whether the MFCs were increasing or decreasing has a significant effect on the lift coefficient. For example at a support angle of 5°, -45% actuation gives a C_l of 0.43 for decreasing but 0.23 for increasing. This can be issue for control if the aircraft pilot or autopilot does not know what C_l is being produced for a given actuation. Control of the MFCs is an interesting problem that has been researched in parallel with this work. A few different successful control methods have been developed by researchers at AVID LLC. [6].

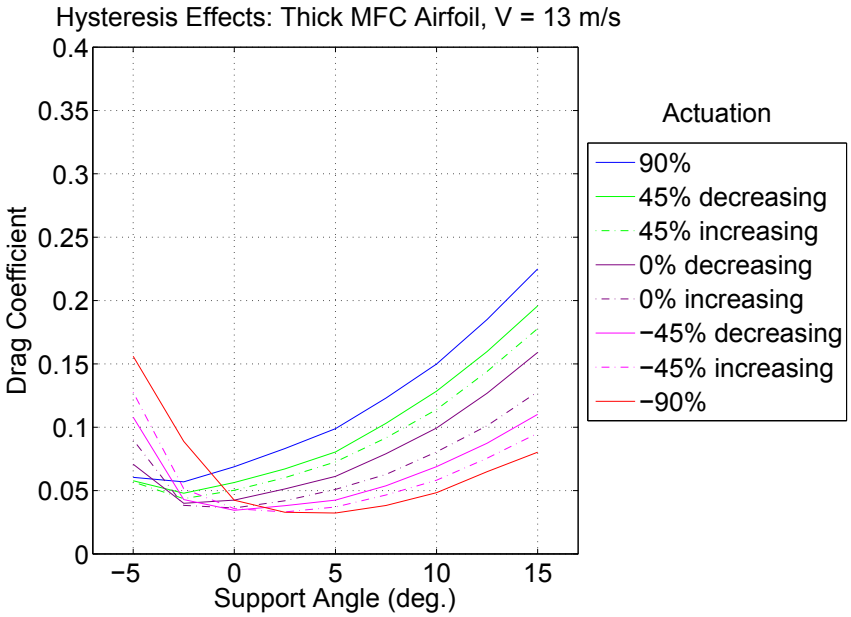

Figure 4.10: Effects of hysteresis on the drag coefficient for the thick MFC airfoil at 13 m/s

Figure 4.10 plots the sectional drag coefficient for the thick MFC airfoil at 13 m/s. Again, only a few actuation levels are shown. The drag coefficient also is affected by whether the MFCs were increasing or decreasing in actuation. At a support angle of 5°, -45% actuation gives 0.042 if decreasing but 0.037 if increasing. Compared to lift coefficient, the hysteresis effects on C_d are not as significant. The differences were much more substantial for lift, and lift is more critical than drag because of its effects on control

4.6 Servo Airfoil Results

The thick servo airfoil was constructed to be a baseline for comparisons and evaluation of the MFC airfoils. Particularly, the goal was to quantify the benefits of the continuous surface. The servo airfoil was actuated by setting the flap angle to a particular degree. A Pulse Width Modulated (PWM) signal controls the servomechanism. The servo moves a linkage which sets the flap to the proper degree. This system is how most small fixed-wing UAVs and hobby RC airplanes are controlled. The flap angle was stepped from $-20°$ to $20°$ at $5°$ increments. There is no hysteresis in the PWM signal controlled servo system so a single value was recorded at each actuation level.

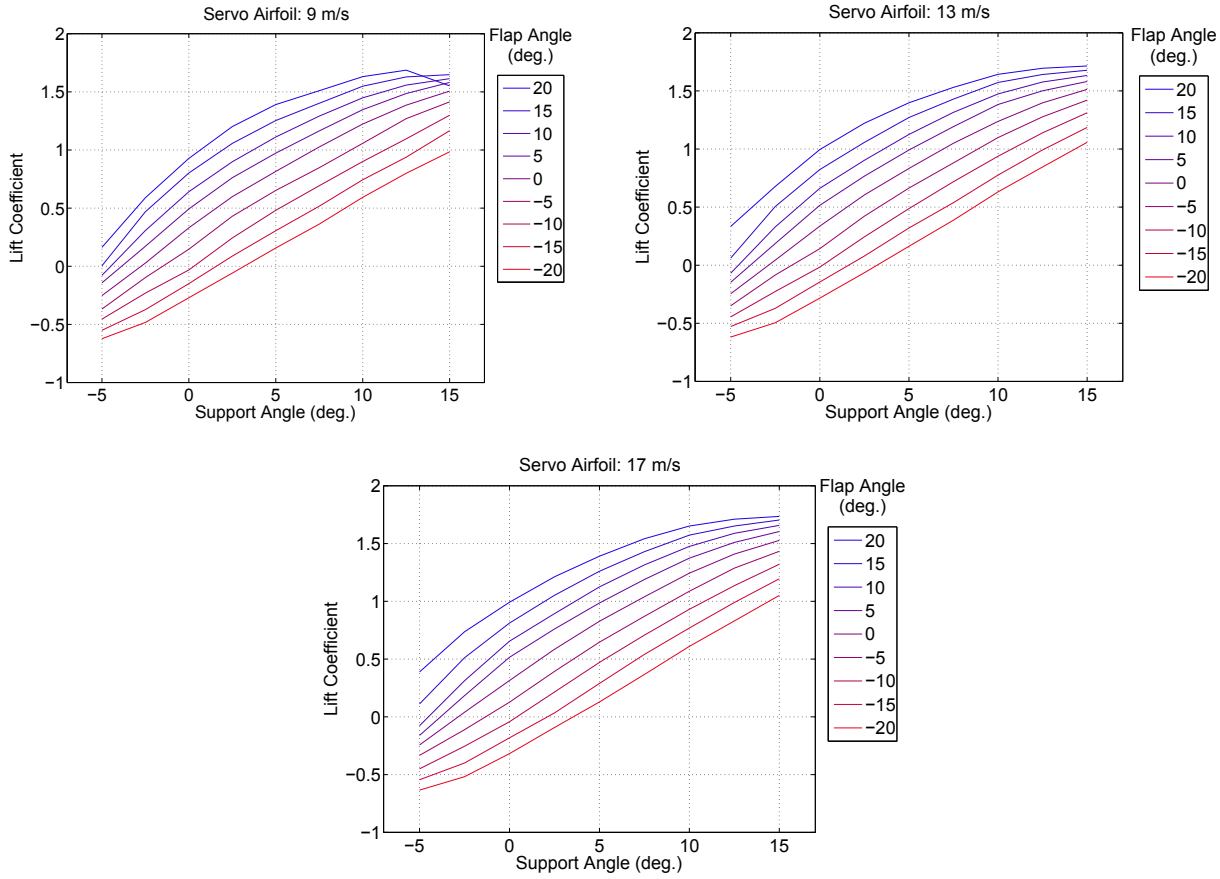

Figure 4.11: Lift Coefficient vs. Support Angle for the servo airfoil at wind velocities of 9, 13, and 17 m/s.

Figure 4.11 shows the sectional lift coefficient for the servo airfoil. The flaps create a good range in lift coefficient that is adequate for controlling a UAV. The C_l range is 0.13 to 1.39 and is consistent for all three wind speeds. Unlike the MFC airfoils, the servo airfoil is not susceptible to aeroelastic effects. The servo control is based on position. The PWM signal specifies a particular position for the servo and the servo will maintain that position no matter the loading, within reason. The servo just draws more power to overcome increased loading. The MFCs on the other hand operate differently. The specified voltage creates a particular strain in the MFCs. Aeroloads then create strain in the opposite direction which works to counteract the MFC-generated strain. The MFCs do not compensate. However, it is possible to build a controller which could include compensation. A more detailed comparison between the thick MFC airfoil and servo airfoil is available in Section 4.7.

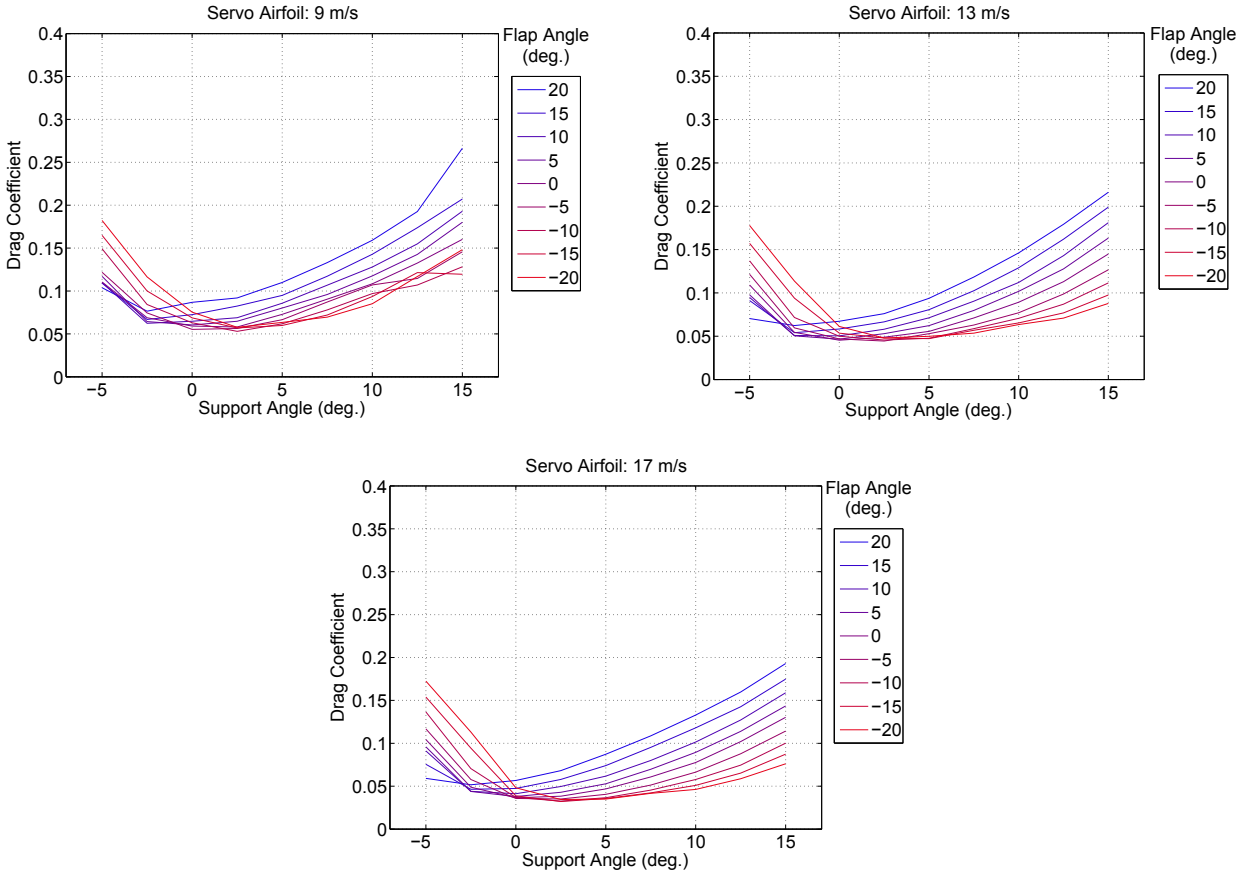

Figure 4.12: Drag Coefficient vs. Support Angle for the servo airfoil at wind velocities of 9, 13, and 17 m/s.

Figure 4.12 presents the sectional drag coefficients for the servo airfoil. Similarly to the case with lift, the drag plots appear nearly identical for each wind speed. The only difference is that the servo begins to stall at 9 m/s and near maximum flap angle.

4.7 MFC Airfoil vs. Servo Airfoil Comparison

This section compares the sectional lift and drag coefficients from the 2-D wind tunnel testing for the servo airfoil to those from the thick MFC airfoil which has two 8514 bimorphs. The two airfoils were constructed to be identical except for the actuation mechanism. The servo airfoil was actuated by a PWM signal which controlled a servo with linkages to move a hinged flap. The MFC airfoil was actuated by voltage which creates strain in the embedded MFCs, and thus moves the trailing edge. The two airfoils underwent testing through various actuation levels at different support angles and different wind speeds. The results were presented in Section 4.4 and Section 4.6.

First, the ability to maximize sectional coefficient of lift while maintaining low drag is important in a control surface. More lift means more possible payload for the UAV. In addition, it is important to minimize drag and thus minimize the required UAV propulsion. Theoretically, the MFC airfoil has advantages. First, the servo airfoil has linkages that are on the exterior surface and interfere with the flow. These linkages will create drag. The MFC has no such linkages. Secondly, the morphing MFC airfoil maintains a continuous profile during actuation. Conversely, the servo airfoil has a hinged flap which when actuated creates a discontinuity in the profile. The discontinuity should disrupt the flow along the airfoil and both decrease lift and increase drag.

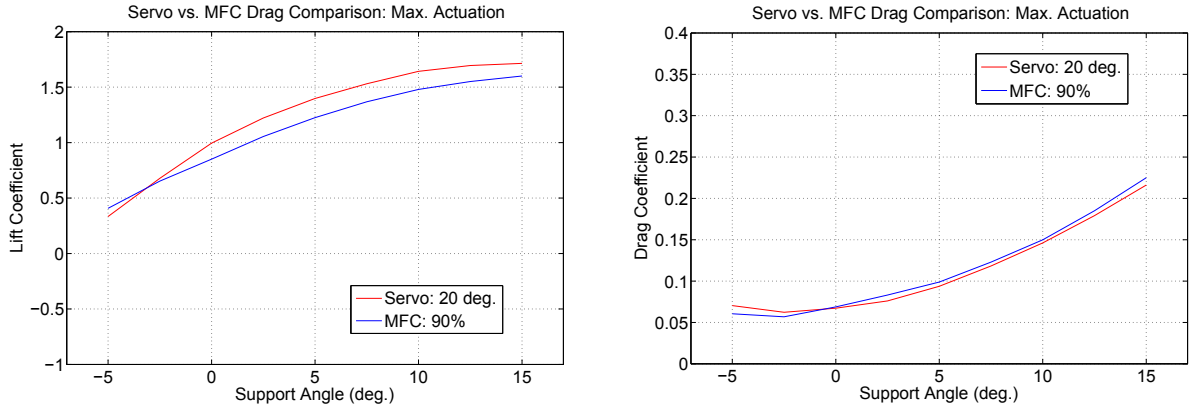

Figure 4.13: Comparison of the servo vs. MFC airfoils with maximum actuation at a wind velocity 13 m/s.

Looking at the plots in Figures 4.11 and 4.7, the servo generally both reaches a larger maximum lift and maintains a larger range at higher wind speeds. However, when uncertainty is included the lift difference becomes less significant and it is difficult to conclude any difference. The uncertainty is discussed and calculated in Appendix A. The range could be made even larger if the servo airfoil was maximized for range in lift. Section 3.1.6 discusses why the servo airfoil was limited for this research. The maximum C_l is higher for the servo airfoil, but again is within the error. Figure 4.13 shows the sectional lift and drag coefficients for both airfoils at maximum actuation at 13 m/s. However, the sectional drag coefficient is nearly identical for each.

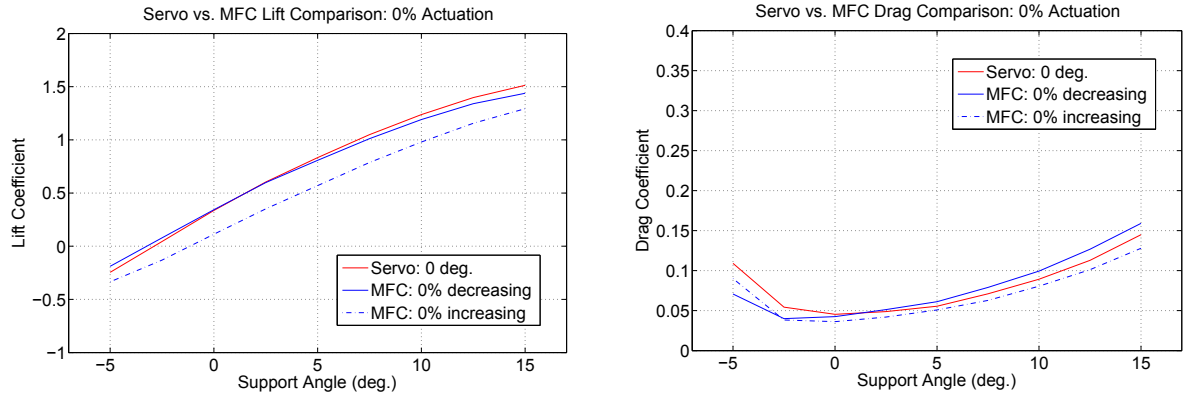

Figure 4.14: Comparison of the servo vs. MFC airfoils with 0% actuation at a wind velocity 13 m/s.

This result is at first surprising. Theoretically, the MFC airfoil should have an advantage in lift and drag. The airfoils were made to isolate and quantify this advantage, but the MFC airfoil has worse lift and nearly identical drag compared to the servo airfoil. One issue is that the servo airfoil at 20 deg. flap angle was made to match the MFC at 100%. However, due to concerns of damaging the MFCs, the extreme value was lowered to 90% to include a margin of safety. This 10% actuation difference could account for the reduced MFC airfoil lift, but not the effect on drag. It is expected that the servo airfoil have higher drag than the MFC airfoil. Increasing the MFC actuation by 10% would only increase drag and exacerbate the discrepancy.

There are a few possible explanations for the result. First, the theoretical MFC aerodynamic advantages may not be significant. The exterior linkages or discontinuity on the servo airfoil may not cause significant drag or decrease in lift. It is also possible the airfoils are not as identical as intended. The goal was to isolate the effects of discontinuity and the exterior linkages. Figure 4.14 shows the sectional lift and drag coefficients for both airfoils at 0% actuation. When comparing non-extreme values like 0%, the MFC airfoil will have two hysteresis values. The servo airfoil was made to match the MFC airfoil before any actuation which is the about the average between the increasing and decreasing values. If the airfoils are identical with no actuation, the lift and drag coefficients of the servo airfoil should be identical to the average C_l and C_d between the two hysteretic values of the MFC airfoil. As Figure 4.14 illustrates, the servo airfoil's C_d is essentially as expected while the C_l is higher than expected. The servo airfoil's C_l did not match the average of the MFC airfoil but instead is closer to the higher decreasing loop values. A couple different factors could cause the difference. The surface finish on the servo airfoil might be slightly better, or possibly the servo airfoil's profile could be just different enough to cause better lift. There are too many variables involved in actuating airfoils. Thus, another experiment was designed using rapid prototyped airfoils in an attempt to truly isolate the effects of discontinuity. The details of this effort are presented in Section 4.8.

However, even given the possible differences in the two airfoils, the wind tunnel data showed

a few weaknesses of the MFC airfoil. One of the reasons the lift coefficient was lower at maximum actuation was aeroelastic effects. Aeroelasticity lowered the deflection so the MFC airfoil did not achieve the same tip deflection as the servo airfoil. Aeroelasiticity also caused decreased C_l range and a dependency on wind speed. The effects of hysteresis are also of concern to an aircraft designer. Fortunately, these weaknesses are not an insurmountable problem. Once quantified, the deflections due to aeroloads can be accounted for in the control surface design. For example, the wing or control surface can be fabricated with a correction such that the aeroload deflection at a cruise velocity puts the surface into proper positioning. The effects of hysteresis can also be mitigated with the proper control algorithm as shown by [6].

4.8 Description of Rapid Prototyped Airfoils

The comparison between the thick servo airfoil and thick MFC airfoil provided many useful conclusions about the advantages and disadvantages of each. However, the experiment was unable to isolate the effects of the continuous-surface actuation. Differences in surface finish and baseline airfoil profile could be clouding the results. In addition, aeroelasticity significantly altered the deflections and thus the comparison. One of the assumptions of evaluating the continuous versus discontinuous was that the deflections were the same. A greater deflection will mean improved C_l. Aeroelasticity in the MFCs, which can be accounted for in the design, prevented equal deflections during actuations. Thus, the question becomes how to quantify the continuous-surface effects without introducing aeroelastic or surface finish differences.

The solution presented in this section was to rapid prototype continuous and discontinuous airfoils. The servo and MFC airfoils were modeled in CAD and rapid prototyped. Developed by AVID LLC., the continuous airfoil model was based on FE results with 0 wind speed and +100% MFC actuation. The discontinuous model was based on the servo airfoil with a flap

that is 30% chord and at 20 deg. flap angle which matched the tip deflection of the MFC within a few hundredths of a degree. Figure 4.15 shows the two CAD model profiles from AVID LLC. They were made with the same chord and span as the other test articles.

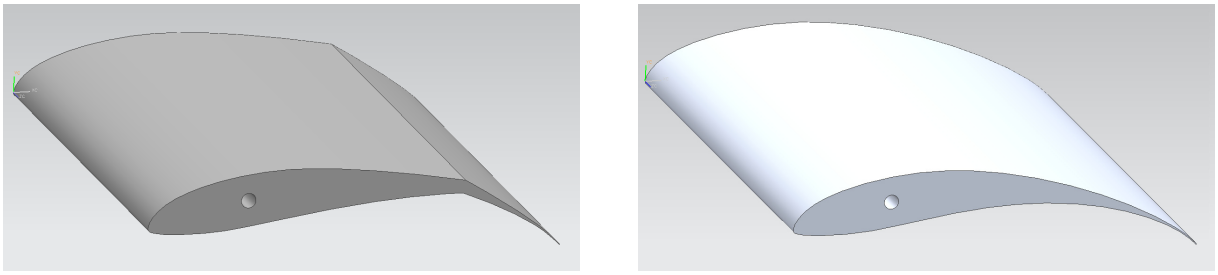

Figure 4.15: CAD models of the flapped and continuous airfoil

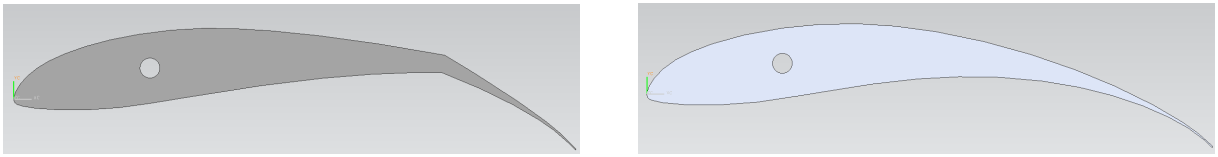

Figure 4.16: CAD models of the flapped and continuous airfoil showing the profiles

There are many advantages of using RP to fabricate the airfoils. One is that the airfoils could be made to be truly identical except for the continuity difference. They were made of the exact same material side-by-side in the same printing session. The deflection was also nearly perfectly matched. The RP airfoils are both stiff enough such that they are not affected by aeroloads. Thus, the deflections remain matched during testing. However, a drawback to the RP is that they cannot actuate. Therefore, only a single actuation level can be compared. Figure 4.17 shows pictures of the two finished airfoils.

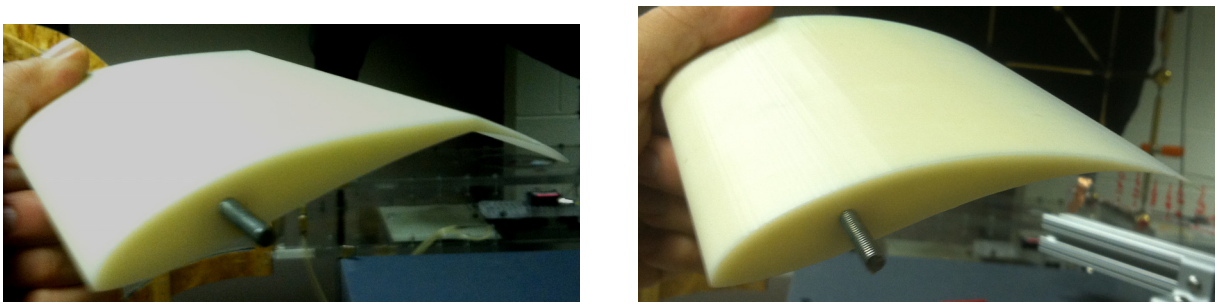

Figure 4.17: RP airfoils after fabrication

4.9 Rapid Prototyped Airfoils Results

Four independent tests for each RP airfoil were done where the airfoil was then installed in the 2-D wind tunnel and tested at a wind speed of 13 m/s. Sectional lift and drag coefficients were calculated at each support angle. Figures 4.18 and 4.19 shows the results from the individual runs and the average of all four runs. The error bars on the averaged data were calculated based on uncertainty of the individual coefficients. Uncertainty calculations are described in Appendix A.

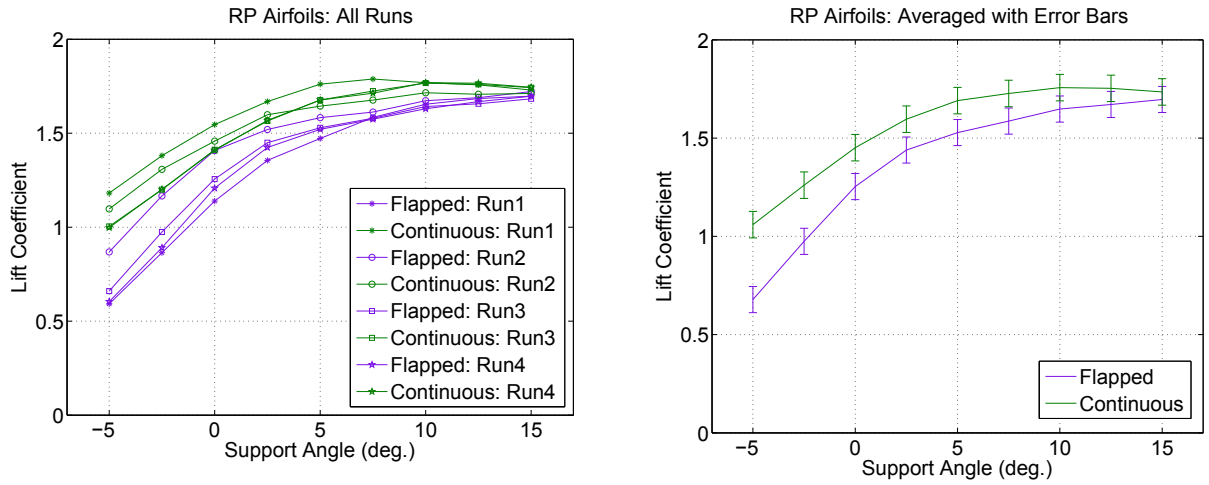

Figure 4.18: Lift Coefficient vs. Support Angle for the RP airfoils at a wind velocity of 13 m/s.

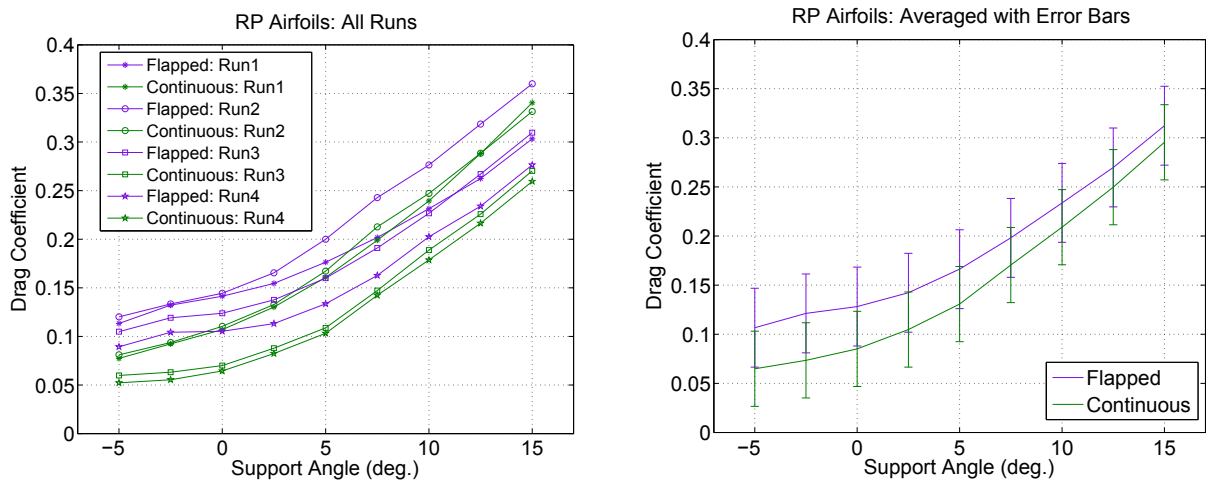

Figure 4.19: Drag Coefficient vs. Support Angle for the RP airfoils at a wind velocity of 13 m/s.

For the RP airfoils, the lift coefficient was generally higher for the continuous airfoil for all support angles. The difference is significant at low support angles and decreased somewhat towards higher support angles. The error was fairly small relative to the measurement and the continuous was almost always higher even given the error in each. The drag coefficient was lower for the continuous airfoil as well, but not as significantly. The average C_d was lower for the continuous at all support angles. However, considering the large error relative to the measurement the difference between the two was not as pronounced as with lift. A few individual runs showed higher average drag for the continuous airfoil at higher support angles.

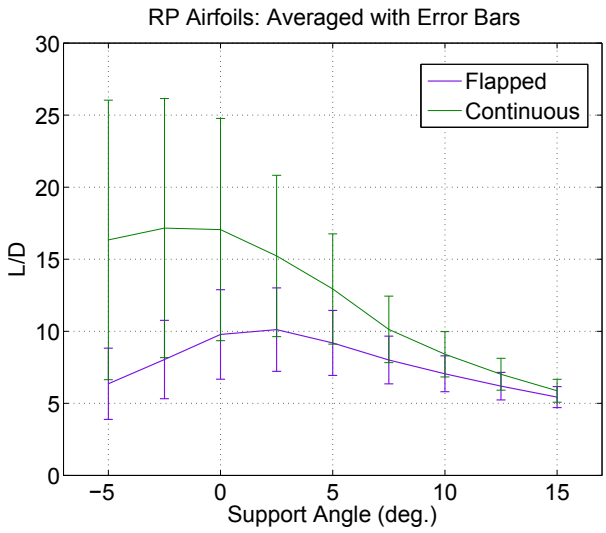

Figure 4.20: L/D vs. Support Angle for the RP airfoils at a wind velocity of 13 m/s.

Figure 4.20 presents the lift to drag ratio of the two airfoils. The L/D ratio is a measure of the airfoils efficiency as a higher L/D means more lift and thus payload for a given drag penalty. The error bars in the ratio were propagated as discussed in Appendix A. The propagation meant that the large error and small value of drag coefficient meant the L/D ratio had fairly large error bars particularly at low support angles where the drag is small. The continuous airfoil overall had a higher L/D with only a small overlap in error bars.

Overall, the RP airfoils data illustrates an advantage of a continuous airfoil. Assuming the surface finish and profile are the same and the airfoils achieve the same deflection under aeroloads, the MFC airfoil should be better aerodynamically than the servo airfoil due to the effects of discontinuity. A real servo control surface could actually be worse than the RP flapped airfoil as the servo will include exterior linkages not included in the RP version. However, the MFC airfoil only has the advantage as long as the stated assumptions hold. As the testing of the actuating airfoils shows, the coefficients are very sensitive to the actual deflection with aeroloads and the MFC airfoil continuous advantage can disappear.

Chapter 5

Frequency Response Testing

5.1 Introduction

This chapter describes the investigation into the frequency response of the MFC airfoils. MFCs, like many piezoelectric devices offer many advantages in frequency response. Particularly, MFCs have shown great potential for increased bandwidth compared to servos and similar technologies. In order to study the frequency response of the MFC airfoils, a series of experiments were conducted.

The experiments compared four different factors affecting the frequency response function. One factor was actuation mechanism. The MFC airfoils' results were compared to those from a similar servo-controlled system. Also, because the frequency response function (FRF) is affected by the entire control and electronics system, the electronics system was varied to illustrate the differences between a large laboratory amplifier and a flight-weight amplifying circuit. Different MFC airfoil configurations were also tested for FRF differences. Lastly, each airfoil was tested in the wind tunnel with and without aerodynamic loading.

5.2 Airfoils Tested

Four different airfoil configurations were tested:

1. Thin GenMAV airfoil with two 8528 MFC bimorphs
2. Thin GenMAV airfoil with two 8514 MFC bimorphs
3. Thick Selig airfoil with two 8528 MFC bimorphs
4. Thick Selig airfoil with a servo mechanism and flap

The two GenMAV airfoils are the same as was used in the 2-D wind tunnel testing. They are described in detail in Section 3.1.6. The thick Selig MFC airfoil was not tested in the 2-D wind tunnel, but is very similar to the thick MFC airfoil from those experiments. Both were made by the same fabrication procedure with the same profile and composite ply schedule described in Section 3.1.6. However, where the 2-D wind tunnel airfoil had 8514 MFCs, the airfoil used in FRF experiments had 8528 MFCs instead. Figure 5.1 shows the two airfoils. The servo airfoil was the same as that from the 2-D wind tunnel. It had a 30% chord flap and actuated ±20 deg. It is also described in detail in Section 3.1.6.

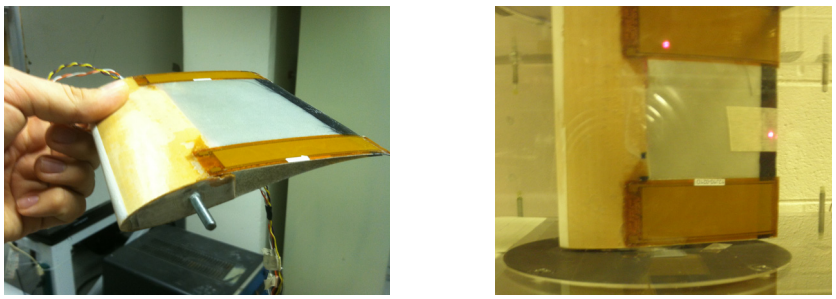

(a) 2-D Wind Tunnel (b) Frequency Response

Figure 5.1: The Selig airfoil used for 2-D wind tunnel testing and the one for frequency response

5.3 Test Equipment

There are three basic components used in these frequency response experiments: the electronics system to provide actuation input, the laser to measure the deflection output, and the wind tunnel which allowed for the study of wind velocity on the output. This section provides a brief description of the major equipment.

The MFC airfoils and servo airfoils were actuated in two different ways. The servo airfoil was controlled by a pulse width modulated (PWM) signal. A computer sent a PWM signal to the servo in the airfoil which rotated the linkage and moved the flap to a particular position. The position is based on the PWM signal. The MFC airfoils, on the other hand, are actuated by applying a voltage directly to the MFC bimorphs as described in Section 3.1.2. In this case, the computer outputs a small control voltage which is then amplified and scaled as required by the MFCs.

Two voltage amplification methods were studied to compare the effects of the control system on the MFC airfoils' frequency response. The first amplification system employed a large Trek 623B high voltage amplifier. The second amplification system used a prototype of the flightweight AMPS circuit designed by Gustafson[5]. Detailed descriptions of these systems are given in Section 3.1.3. During testing, the airfoils were installed in the wind tunnel at Virginia Tech's CIMSS laboratory. This wind tunnel was the same as used for the 2-D wind tunnel experiments of the previous chapters, and is described in detail in Chapter 3. For these tests, a fixture was made to hold the C-arm fixed and minimize its effect on the frequency response of the airfoils. A laser measured the displacement of each airfoil's trailing edge.

5.4 Test Procedure

The testing procedure was developed by AVID, LLC. and has been used for previous frequency response experiments on MFC airfoils[6][3]. After installation in the wind tunnel, the procedure has been went as follows. Using National Instrument's LabVIEW software, a sinusoidal control signal of a specified frequency was generated. This control signal was then either outputted as a PWM signal and sent to the servo airfoil or for the MFC airfoils, outputted as voltage and sent to one of the voltage amplifier circuits. The amplitude of the input signals was such that when scaled represented $\pm 40\%$ actuation for the airfoils. The laser then measured the TE displacement output for that particular control signal. The frequency of the sine wave inputs was varied such that the input and output relationship was recorded at several points across the bandwidth of the airfoils. Gain and phase could then be calculated at each point and plotted.

This process was repeated for each airfoil such that the frequency response could be calculated at two different wind speeds, 0 and 17 m/s. This was done to compare the effects of aerodynamic loading on the frequency response. The tests were also repeated with MFC airfoils using the two different amplification systems. For each system, the airfoil was tested at both wind speeds. Thus, the MFC airfoils were tested in four different setups while servo airfoil was only tested in two different setups.

The data processing used a MATLAB code also developed by AVID, LLC. The output displacement data was first filtered with a second order Butterworth filter and then was fit to a sine wave. This sine wave was then scaled by the first low frequency data point to normalize. The calculated gain and phase shifts were then plotted as a function of the corresponding input signal. A transfer function was then fit to the data points. Figure 5.2 through 5.5 show the calculated bode plots and transfer function fits.

5.5 Results and Conclusions

This section presents the frequency response data and analyzes it comparing between the wind at 0 m/s vs 17 m/s, the MFC vs. servo airfoils, and the Trek vs. AMPS board amplifiers.

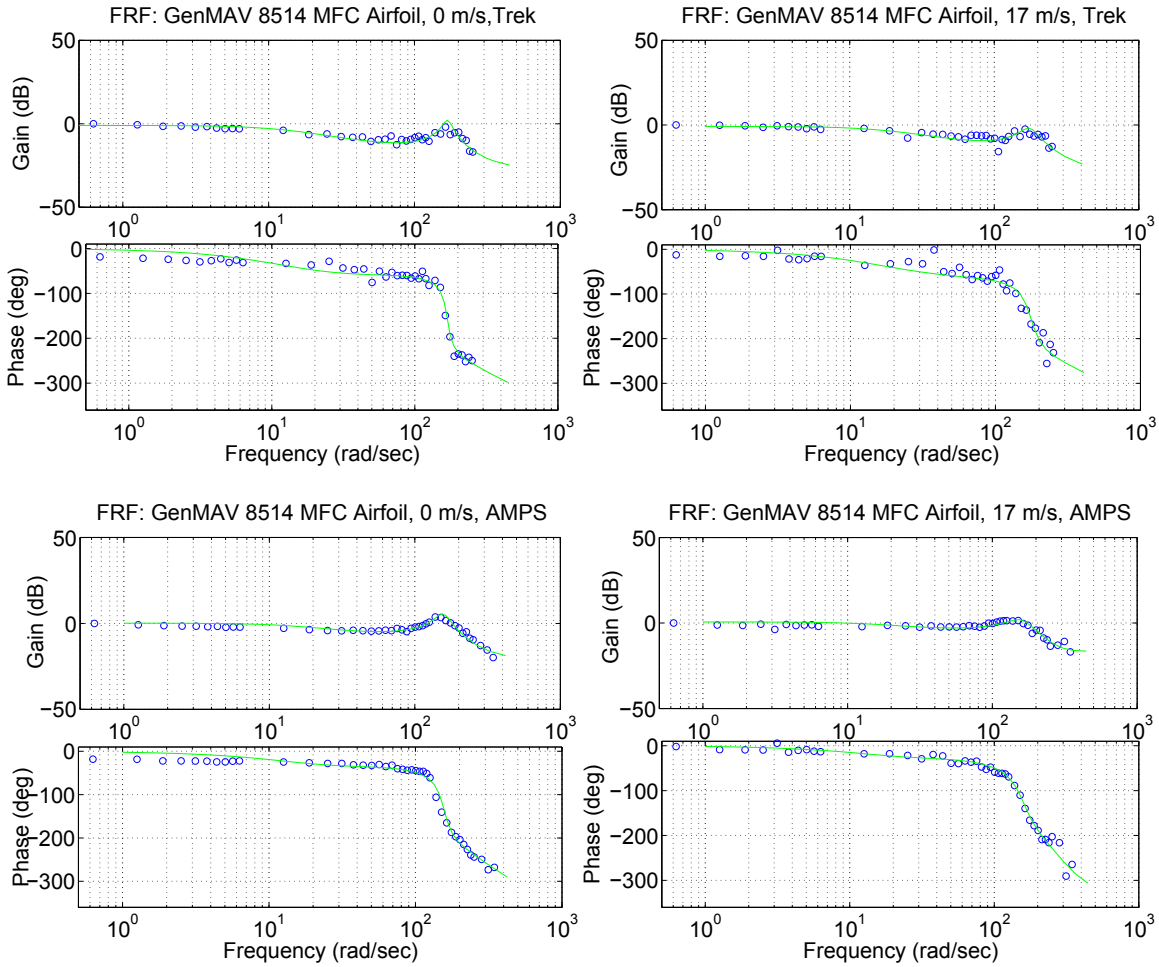

Figure 5.2: Plot of the frequency response of the GenMAV 8514 MFC airfoil.

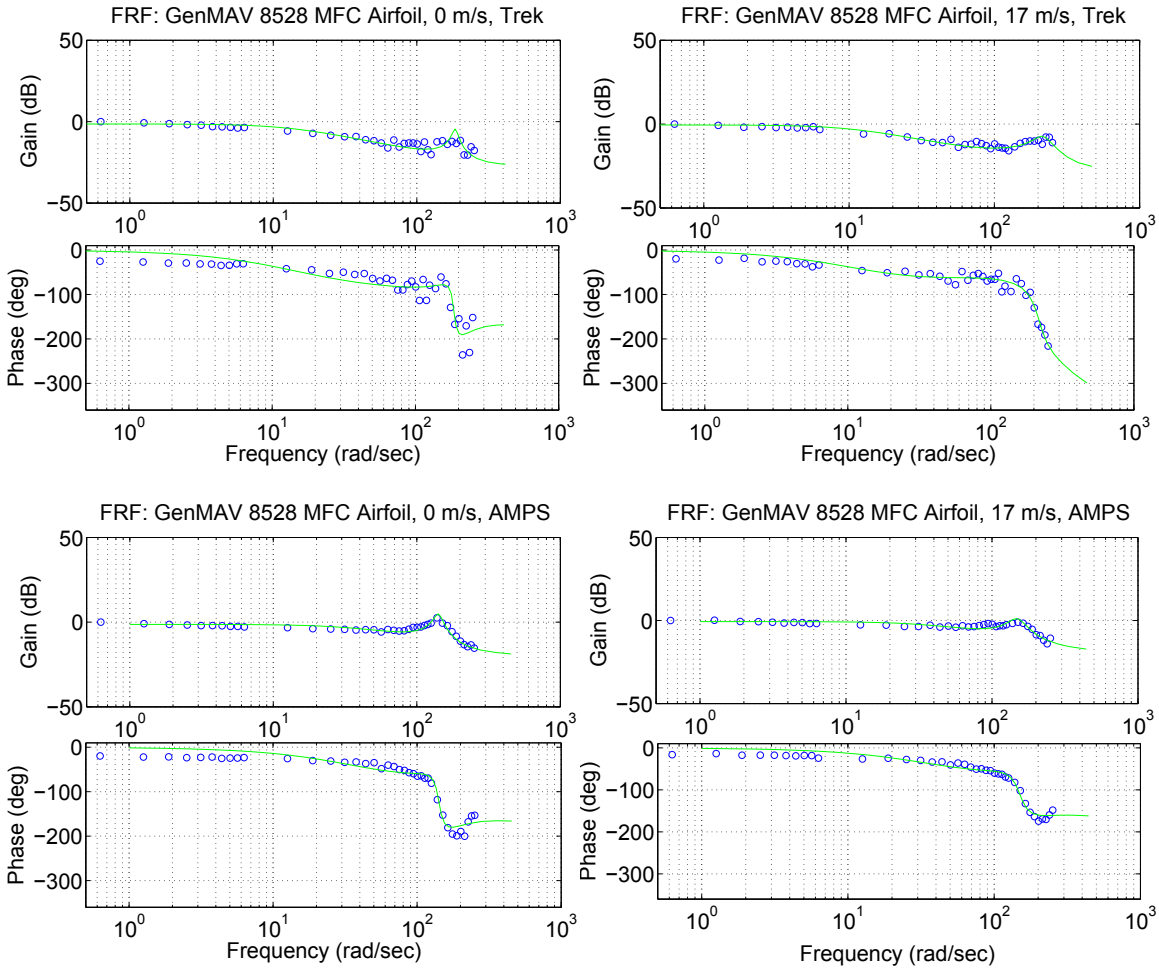

Figure 5.3: Plot of the frequency response of the GenMAV 8528 MFC airfoil.

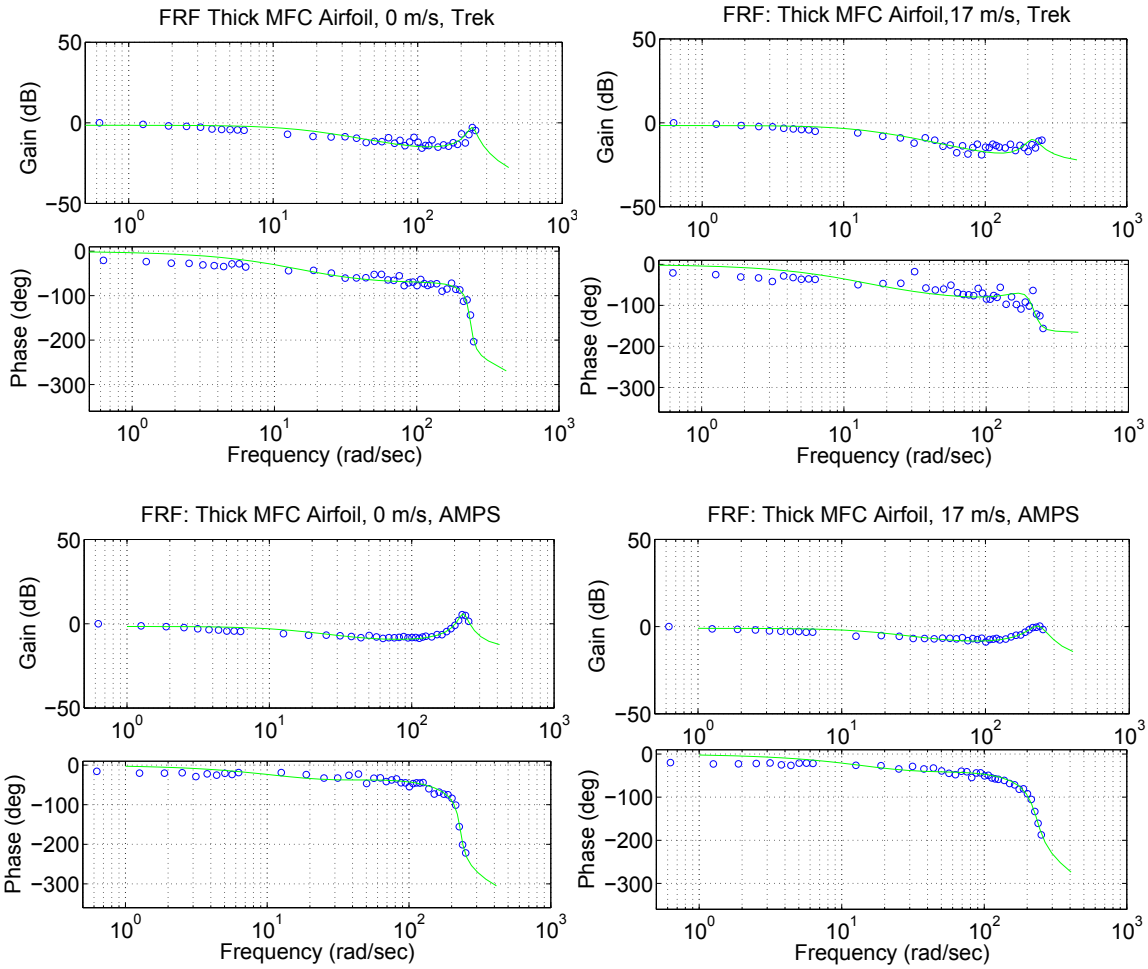

Figure 5.4: Plot of the frequency response of the thick MFC airfoil.

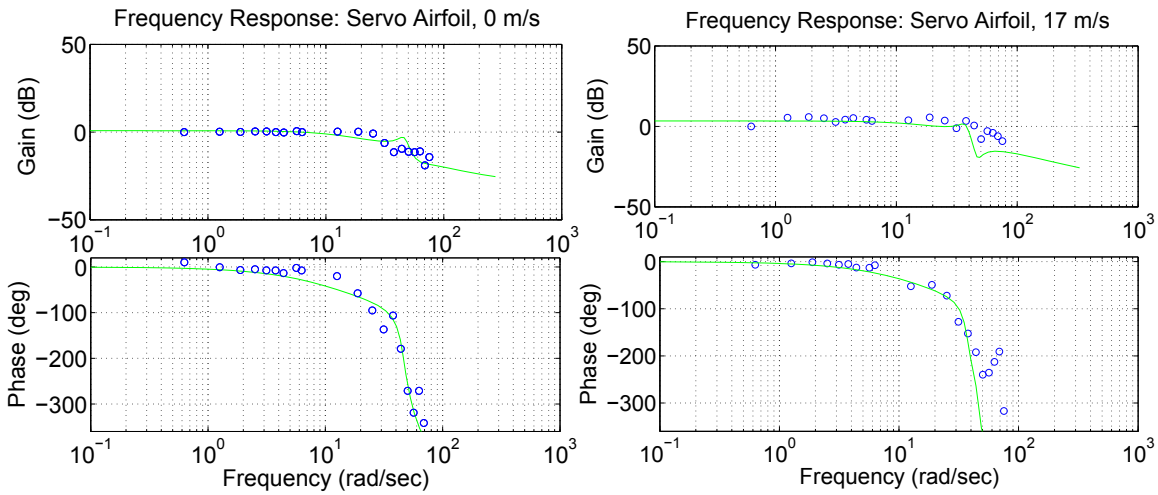

Figure 5.5: Plot of the frequency response of the servo airfoil.

Overall, the data was consistent with previous frequency tests on similar airfoils from literature[6][3]. Three main bases for comparison are shown below. As presented above, the transfer function (TF) fit the data relatively well except in a few notable instances. First, towards higher frequencies after the natural frequency, the data gets noisy and the TF becomes only a rough estimate of the data. Second, the TF does not model the phase lag in the MFC airfoils at low frequency. The MFC airfoils consistently had a small phase lag even at low frequency. Some in literature have theorized this is an artifact of the hysteresis.

0 m/s vs. 17 m/s

For the MFC airfoil, aerodynamic loads did not affect the overall frequency response significantly. The slight phase lag observed in previous tests was not affected by the aerodynamic loading. The resonance frequency also remained approximately the same for both wind conditions. The most notable effect of the wind was to decrease the gain resonance peak. This effect was expected as the aerodynamic loading should counteract extremes in deflection like those caused by resonance, and act like an increase in damping. For the servo airfoil, the aerodynamic loadings had almost no effect. The only differences are at frequencies where the data is noisier and the transfer functions are not as effective estimates.

Trek Amplifier vs. AMPS board

While the low frequency phase lag remained, the AMPS board decreased the phase lag seen at middle to high frequencies. The AMPS board also had almost half the gain attenuation at higher frequencies before and around resonance. The AMPS system seems to be more effective at all frequencies than the larger Trek.

Servo vs. MFC

One major difference between the MFC airfoils and the servo airfoil is the MFC airfoils' increased natural frequency. The servo airfoil experiences a phase lag and gain attenuation after approximately 4 Hz while the MFC airfoils maintains a low phase and gain attenuation until its resonance frequency near 40 Hz. This gain attenuation below 40 Hz does reach significant values depending on the exact application. However, until 4 Hz the servo does exhibit better behavior with low phase lag and nearly zero gain. The positive gain for the servo airfoil shown in the plots is likely a result of error being magnified by the transfer function fit. The MFC airfoils show a small gradually increasing phase lag which has also appeared in previous experiments. The small gradually increasing gain attenuation is also a concern. However, because the MFC airfoils lags are small, it may be possible with a control system to achieve a significantly larger bandwidth compared to the servo.

As for comparing the effect of aerodynamic loading on the two airfoils types, the aerodynamic loadings do not seem to affect the general trends of either significantly. However, the wind does have a damping effect on the MFC airfoil response, as the wind reduces the resonance peak somewhat. The servo data is also much noisier than the MFC due to constraints on sampling rate. Thus, it is more difficult to draw conclusions about the specific transfer function dynamics for the servo airfoil.

Chapter 6

Description of FE Model of Full Wing Morphing

One of the potential applications of an embedded actuator such as an MFC is to allow the morphing of the entire wing surface. Instead of discrete control surfaces, a wing could be designed such that the entire surface morphs to create camber change and angle of attack change. The goal of this study is to examine the parameters that affect the the morphing ability and to quantify that effect.

6.1 Introduction

Currently, almost all unmanned and manned aircraft are controlled with discrete designated control surfaces. The idea is that there is the fixed wing surface, and a section of this surface is separated and hinged to be a control surface. This surface is then deflected to create camber change and thus lift change and control actuation. The camber change can be done with continuous embedded actuators such as MFCs which is the focus of the first part of this thesis. However, because MFCs can be embedded in many configuration, they do not have

to be constrained to discrete surfaces and can be arranged to create much more complex deflection shapes.

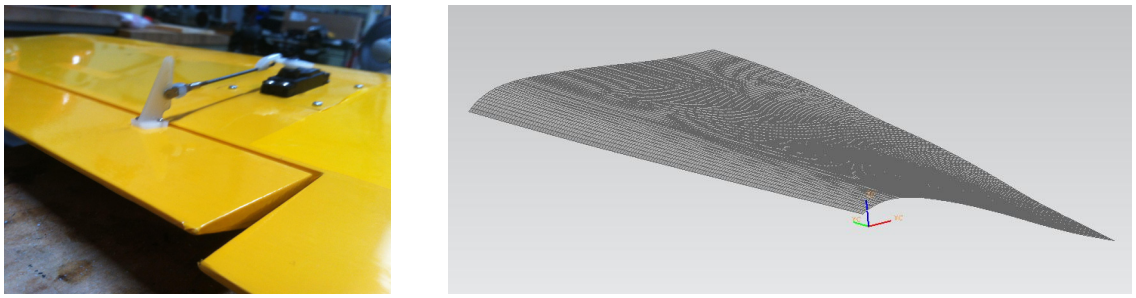

(a) Discrete (b) Full Wing Morphing

Figure 6.1: Examples showing different control methods.

The objective is to contort the entire wing planform to create complex, twisted shapes. Entire wing morph is not a new idea to aerodynamics. The Wright brothers employed wing warping in their original airplanes[23]. MFCs enable small UAVs to also use this technology. The research presented here attempts to quantify the abilities of wing morphing to actuate roll and how the variation of certain parameters affects this ability.

6.2 Methodology

As stated above, the goal is to evaluate MFC actuated wing morphing and how varying certain parameters can improve the performance. Performance here will be evaluated based the criteria of how well the morphing controls the aircraft. The wing morphing replaces normal ailerons, which primarily are responsible for roll. Thus, the measure of performance is how well the wing morphing creates roll moment.

An added complication that has to be compensated for is aeroelasticity. The wings must be inherently flexible to allow the MFCs to bend them and create deflection. However, this flexibility means that maximizing the deflection created by the MFCs comprises the wing's ability to maintain shape under aerodynamic loading. Thus part of the evaluation process

will be to balance the roll moment created against the wing's stiffness against aerodynamic loading. The stiffness against aerodynamic loads will be measured by looking at deflection magnitudes without aeroloads versus with aeroloads. The case with aeroloads will be determined by evaluating the static loading and converging to the deflection pattern with those loads by the process described here.

The process of design and evaluation will consist of modeling the wing in a finite element solver to get deflections and then input the new shape into a flow simulator to evaluate aerodynamic coefficients and generate aerodynamic loads. The aerodynamic loading can then be inputted back into the finite element solver to get a new deflection shape. The process is repeated until the wing converges to a particular deflection. Figure 6.2 shows the block diagram this process.

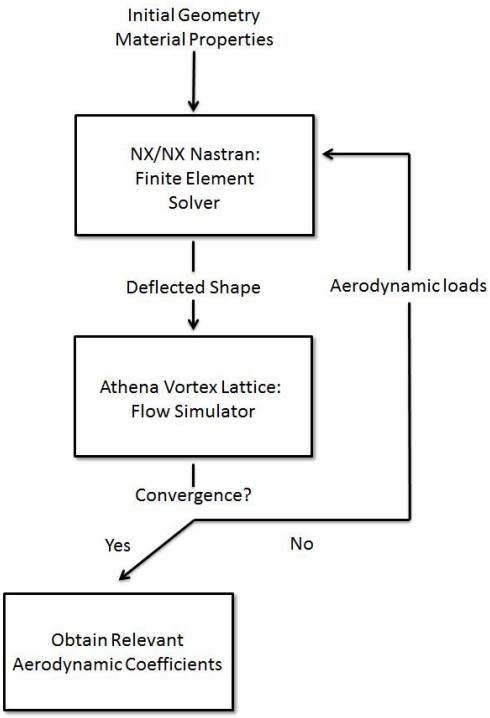

Figure 6.2: Block diagram of the process for converging to a deflection and obtaining the aerodynamic coefficients.

There are numerous parameters that affect deflection and stiffness against loading. One of the advantages of MFCs in morphing wings is the many configurations this system can be implemented. The following parameters are key, but there exist many ways to vary each parameter and each has advantages and disadvantages:

- Undeflected airfoil profile
- Number of MFC actuators
- Size of MFC actuators
- Actuator orientation relative to chord line
- Actuator location on chord line
- Actuator location along span
- Composite substrate material
- Composite substrate thickness
- Composite substrate orientation schedule

These parameters represent a tremendous design space as each can be varied independently, but the effects could potentially couple. In order to tackle the problem, a few assumptions and simplifications were made to examine the effects of particular parameters in more detail. This will be discussed in more detail in Section 7.1.1.

6.3 Finite Element Model

Finite element analysis was chosen to solve for the deflection created when a composite wing is actuated by embedded MFCs. This method has proven successful in previous models of wings and airfoils with MFCs [5]. The parts were created in the computer design program, NX. The geometry and material properties of the wing were assigned. NX then creates an input file for NX Nastran which solves the finite element problem and outputs the deflection results to be post-processed and viewed in NX again.

6.3.1 Geometry and Boundary Conditions

The airfoil profile chosen for this study was the GenMAV airfoil. This airfoil was created to be a baseline to compare the effects of different research projects on MAV technology[10]. The coordinates for this airfoil are given in Stewart et al. [10]. The wingspan was chosen to be 2 ft. and the chord 5 in. as this matches wind tunnel results and that of the flight test vehicles currently under development by AVID LLC. The finite element model of an undeflected thin GenMAV wing is shown in Figure 6.3.

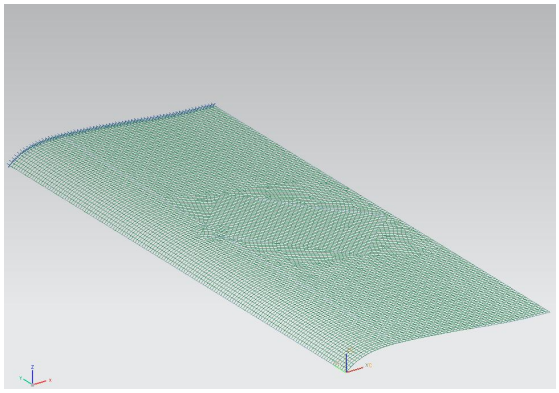

Figure 6.3: Finite element representation of one side of the wing with a fixed boundary condition at the fuselage attachment point.

The wings are fastened to the fuselage in the center leaving 1 ft. on either side. This attachment creates a boundary condition where the wing is constrained against all deflection along the centerline of the wing where it is attached to the fuselage. Because of this attachment point and boundary condition, only one half of the wing is modeled. In the real wing, when performing a roll maneuver, the wing will actuate asymmetrically with half the wing deflecting up and the other half deflecting down. The deflections of the downward and upward actuations are modeled independently. They will later be combined when solving for the flow and aerodynamic forces.

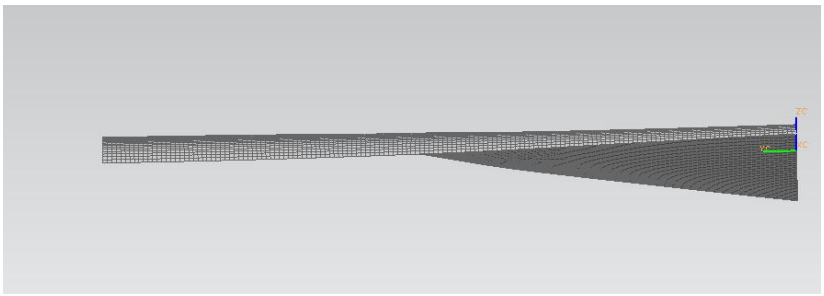

(a)

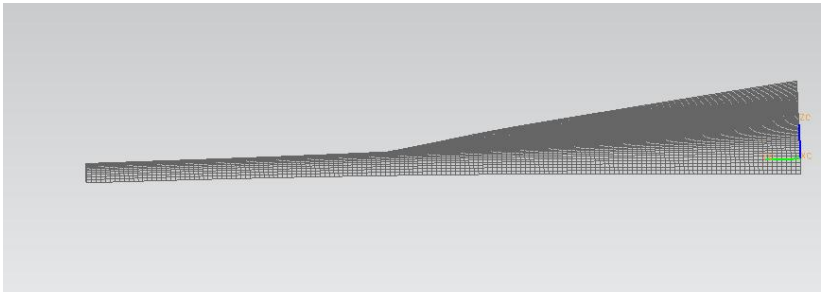

(b)

Figure 6.4: Example of a) positive, downward deflection, and b) negative, upward deflection.

For simplicity the wing was designed with zero dihedral and zero wing sweep. The results can easily be applied to a dihedral or swept wing design by transforming the forces into the appropriate coordinate system. The wing will also be composed of a composite material and be relatively thin on the order of 1 mm. The exact thickness depends on the composites used and the number of layers. This is one of the design parameters to be examined later.

6.3.2 Composite Properties

The basic structure of the wing is a thin composite wing with MFC patches epoxied to the upper and lower surface in a symmetric bimorph configuration. The exact material composition and orientation of the composite substrate is one of the design parameters to be evaluated. Any material could be used for the substrate. However, for this study the design space was limited to composites due to the ease of fabrication. Composites are easily molded to complex shapes such as that of an airfoil. In addition, the anisotropic properties of

most composites mean the stiffness can be tailored in certain directions to allow large MFC deflection while maintain stiffness against aerodynamic loadings. Many researchers have shown in detail the advantages and disadvantages of using composites in MFC actuated applications[5][9].

Even further, the research presented here focused the study to two common composite materials: fiberglass, specifically E-glass, and carbon fiber, CF. These materials have proven successful in similar airfoils including those used in Chapters 3 and 4 [5]. They also represent a range of the possible stiffness choices of composite substrate. The carbon fiber has a relatively large elastic modulus while the fiberglass has a more moderate elastic modulus. In addition, the composite material was limited further to weave fabrics with two sets of fibers oriented perpendicular to one another. A picture of these weaves is shown in Figure 6.5. This limitation was done for easier comparison to previous research and for ease of fabrication[5]. The perpendicular weaves also create balanced laminates which have beneficial properties that are detailed in depth in Hyer[24].

(a) (b)

Figure 6.5: Examples of carbon fiber and fiberglass weave fabrics.

For the calculation of material properties, the matrix material which cures and binds the layers together was chosen to be West System 105/206 Epoxy. Again this was chosen to compare to previous research, and because the material properties for this composite composition have already been calculated and verified[5]. The material properties of the constituent materials are from Gustafson[5]. The total composite properties of the two types of composite

after fabrication are shown in Table 6.1.

Table 6.1: Material properties after fabrication with epoxy. All values from Gustafson[5]

Composite Type	E_x (MPa)	E_y (MPa)	G_{xy} (MPa)	Poisson's Ratio
Carbon Fiber	63720	63720	3310	0.04
Fiberglass	23710	23710	3100	0.09
MFC	31200	17050	5270	0.303

6.3.3 MFC Properties and the Thermal Analogy

The material properties of macro-fiber composites have been the subject of a great deal of research. Several researchers including Williams and Bilgen have developed models and material properties for MFC actuators [9][8]. In addition, MFCs are manufactured by Smart Material Corporation, who supply their own values for the various material properties[20]. Gustafson also gives a detailed discussion of the comparisons between the various models. However, each model is consistent within a few percent. Again for better comparison with previously verified results on this project, Gustafson's values were used and are shown in Table 6.1[5].

The key to modeling the deformation caused by MFC actuation is modeling the expansion and contraction. NX and NX Nastran like most finite element solvers do not have a feature specific for piezoelectric expansion. However, piezoelectric expansion and contraction is not physically different than thermal expansion. Thermal expansion can be modeled in NX and NX Nastran. Gustafson provides a detailed derivation of the coefficients of thermal expansion which can model the piezoelectric expansion of MFCs due to voltage. Other researchers outside this project have also used this technique[12]. Gustafson studied expansion from -100% actuation through 100% and derived coefficients for the low and high voltage regions. In this study of morphing wings, the interest is comparing the effects of different parameters so the actuation percentage was always set to 100%. Gustafson's thermal analogy values for

100% actuation are shown in Table 6.2[5].

Thermal Analogy:

$\Delta L/L = \alpha \Delta T$ (Thermal expansion)

$\Delta L/L = \alpha \Delta V$ (MFC expansion)

Where ΔV ranges from -500 to 1500V as the actuation range of an MFC.

Table 6.2: Thermal expansion coefficients equivalent to piezoelectric strain. Values from Gustafson[5]

		Top MFC	Top MFC	Bottom MFC	Bottom MFC
Actuation (%)	$\Delta V(V)$	$\alpha_x(\frac{1}{V}\text{x}10^{-7})$	$\alpha_y(\frac{1}{V}\text{x}10^{-7})$	$\alpha_x(\frac{1}{V}\text{x}10^{-7})$	$\alpha_y(\frac{1}{V}\text{x}10^{-7})$
100	1500	10.02	-4.575	-3.34	1.525

In a bimorph configuration, the voltages are applied asymmetrically where the bottom MFC receives a third of the voltage as the top MFC and receives the opposite sign. In NX, only a single temperature, which is analogous to voltage, can be applied to a region. Thus, to account for the different applied voltages, the thermal expansion coefficients are scaled appropriately.

6.3.4 Details of FE model

The thin wing was modeled with 2-D 4-node shell elements called CQUAD4 elements. These elements are suitable due to the small thickness and have been verified in similar models[5]. Element lengths of 2 mm modeled the surfaces well and provided adequate geometry resolution for export into the flow simulator. A nonlinear static solution was chosen due to the complex geometry of the airfoil profile and the large deflections. In NX Nastran, the basic nonlinear static solution is NLSTATIC 106.

In assigning the geometry, the wing was separated into groups of elements called bodies. Different material properties and loadings could then be applied to each body. In addition,

because of the orthogonal nature of the composite material properties, a material principal direction, x, was defined for each body. Thus the wing surface was divided into bodies where the material properties changed.

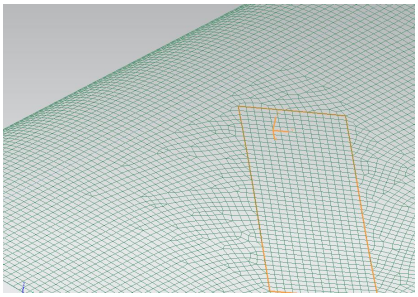

Figure 6.6: Example of a body (highlighted in orange) representing an MFC patch and substrate with a defined material coordinate system.

NX also has a laminate feature which allows for easy definition of composite laminates such as those used throughout this research. For a body of elements, first the material coordinate system was defined. Then the laminate feature allows you to set the number of layers, the layer order, the material of each layer, the orientation relative to the material coordinate system, and the thickness of each layer. NX and NX Nastran then solve for the overall laminate properties when solving the simulation.

For loadings, the first iteration only included a temperature loading of 1500 degrees C, or -1500 degrees C for negative actuation. This temperature corresponds to 100% actuation by the thermal analogy discussed above. The true thermal expansion coefficients were set to zero for all the materials so no real thermal expansion would occur. For successive iterations, the pressure field from the flow simulator was included as pressure loading.

After solving, NX Nastran output the displacement of each node and the new shape of the wing. The displacements of each node could then be transferred to a Microsoft Excel file for export to the flow simulator.

6.4 FE Model Verification

It is important to assess the validity of any model. Here as a preliminary study to verify the accuracy of the finite element model results, a few finite element solutions were created which could be compared to classical lamination theory which is a well-known and accepted model of laminate behavior[24]. An experimental test case was also run on the more complex geometry of an MFC GenMAV airfoil. The deflection of this airfoil was then compared to experimental results for that particular airfoil.

6.4.1 Modeling a Bimorph with Substrate

The verification solutions are to show the NX/NX Nastran solution and the elemental representation are accurate modeling a laminate with expanding and contracting layers separated by a substrate. In this case, a bimorph was modeled in FE and compared to an accepted solution. Figure 6.7 shows a layer-view of a MFC bimorph with a generic substrate.

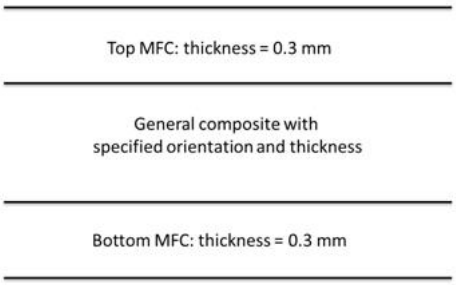

Figure 6.7: Ply schedule for general bimorph with a composite substrate.

Classical Lamination Theory

Classical lamination theory (CLT), is derived in great detail in Hyer[24], but a few of the highlights will be shown here. CLT relies on few key assumptions including but not limited to:

- Elastic deformation

- Undeformed normal lines
- Plane-stress

The bimorph model is essentially a thin plate so 2-D plane stress applies and assuming the stress does not approach the strength of the material the other assumptions hold as well. Because previous MFC actuated composites have proven successful and have not approached the material strength, this is likely a valid assumption. Williams also verified the validity of CLT for MFC and bimorph modeling[8].

With these assumptions and the material properties of each layer, CLT provides a method for determining strains and curvatures of laminate given applied loads such as a thermal expansion loading. Again the details are available in Hyer[24]. Given a system such as the bimorph with substrate employing the thermal analogy and then applying a temperature load, CLT will give an estimate of the expected laminate strains and curvatures.

CLT vs. FEM: 8528 Bimorph

The bimorph test case uses a bimorph with a fiberglass substrate. The material direction is defined where the x-axis is in the direction of the MFC piezoelectric fibers. The fiberglass fibers are oriented 0 deg. meaning the fibers are in the same direction as the MFC fibers. The MFC material properties are taken from Table 6.1 and Table 6.2. The fiberglass material properties are taken for a typical fiberglass composite with a polymer matrix. These were taken from Hyer and shown in Table 6.3[24]. The bimorph size was chosen to be based on an 85 mm by 28 mm actuator and the geometry is shown in Figure 6.8.

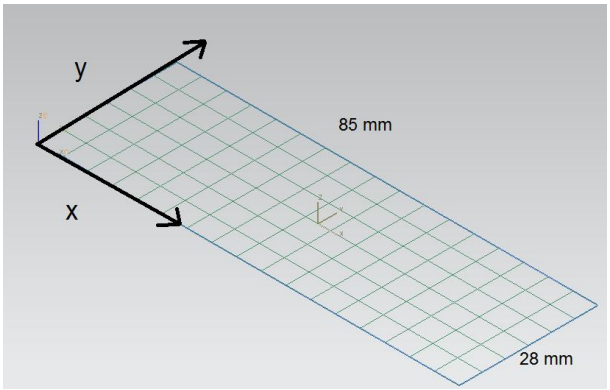

Figure 6.8: Geometry of 8528 bimorph test case

Table 6.3: Fiberglass and polymer composite material properties from Hyer[24]

	E_x (MPa)	E_y (MPa)	G_{xy} (MPa)	Poisson's Ratio
Fiberglass/polymer	50000	15200	4700	0.254

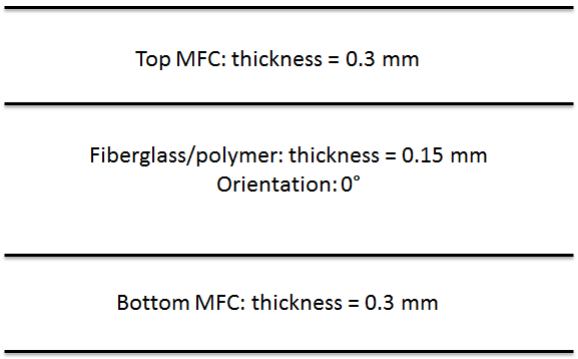

Figure 6.9: Ply schedule for 8528 bimorph test case 1

These material properties and layer information were then run in a CLT computer code which outputs the strains and curvatures given a temperature of $1500\,\mathrm{deg}\,C$.

Classical Lamination Theory Results

With the given dimensions and calculation of the strains, the non-zero displacement and curvatures in each direction are:

$\Delta x = 0.0305$ mm

$\Delta y = -0.0047$ mm

Curvature in x-direction, $\kappa_x = -0.00383$ 1/m

Finite Element Results:

The finite element mesh of the bimorph is shown above in Figure 6.8. The bimorph was constrained with a fixed boundary condition at the midpoint of left short edge. A nonlinear solution was then run with CQUAD4 elements and the same finite element model choices as discussed in the sections above including NX's laminate feature. The same material properties and temperature loading was used as with CLT. The results are shown in Figure 6.10.

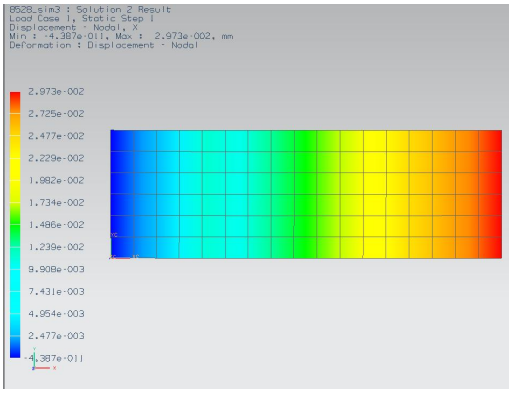

(a) x-displacement

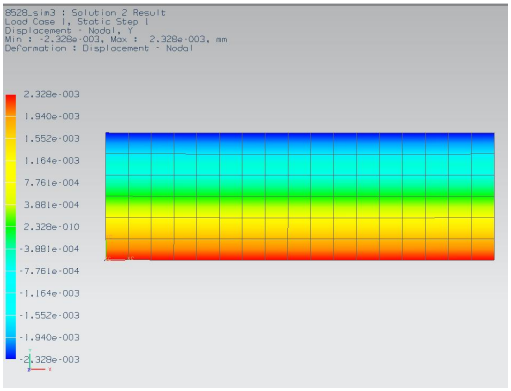

(b) y-displacement

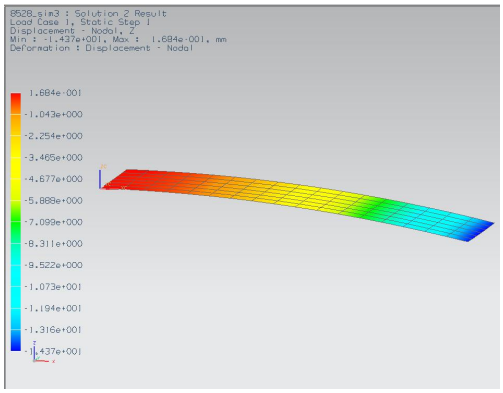

(c) z-displacement

Figure 6.10: Geometry of 8528 bimorph test case

The tip displacements from finite element analysis are:

$\Delta x = 0.0297$ mm

$\Delta y = 2 * (-0.00233) = -0.00466$ mm

$\Delta z = -14.37$ mm which equates to a curvature in the x-direction of $\kappa_x = -0.00387$ 1/m

Comparison

The Classical Lamination Theory results match the finite element results very well. All non-zero displacements and curvatures were within 3%. It is also worth noting, this comparison uses the same material and MFC-expansion properties which are the most likely source of error in a real MFC system. The comparison validates the finite element mesh and the assumptions associated with the actual solution method.

6.4.2 Experiment vs. FEM: GenMAV Airfoil

In addition, to the verifications against classical laminate theory, a test case was performed to look at the accuracy of modeling a complex airfoil with several ply schedule changes and a complex geometry like what would be used for this study on full wing morphing. This test will also include the error associated with the estimation of material properties and the thermal analogy. For this test case, the finite element solution would be compared to experimental data. During wind tunnel testing, a laser measured airfoil displacement during actuation. The laser used was an optoNCDT ILD1800-200. Figure 6.11 shows the experimental setup where the red dot on the trailing edge is the laser measuring deflection. For comparison against the finite element model, the airfoil was actuated +90% to -90% then back to +90% without aerodynamic loading.

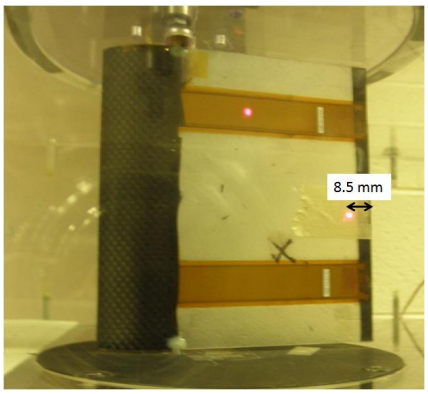

Figure 6.11: GenMAV airfoil in wind tunnel for deflection testing

The airfoil used in this experiment was a thin GenMAV airfoil embedded with two MFCs that were 85 mm by 14 mm. The composite schedule was that used for all GenMAV wind tunnel testing. The composite layup and fabrication process was developed by Gustafson[5]. The layup schedule for the airfoil is mix of carbon fiber and E-glass with epoxy matrix. The exact layup is shown in Figure 6.12. The airfoil was made for 2-D testing and had a 5 in chord with a 5.25 in span. It also described in detail in Section 3.1.6.

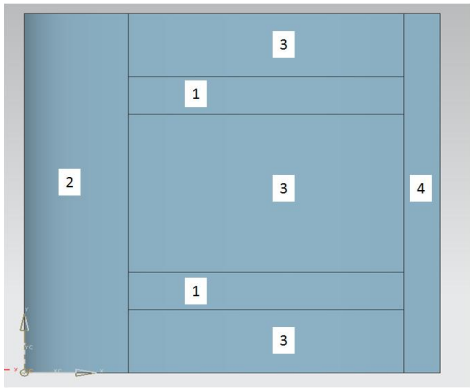

Figure 6.12: Diagram of the ply schedule for different sections of GenMAV 8514 airfoil

The finite element model was based on this airfoil. Figure 6.13 shows the mesh and geometry of the model. The red represents a temperature load while the blue crosses represent a fix constraint. The mesh and composite characteristics were defined by the process described in the preceding sections. The system was solved at +90% actuation and Figure 6.13 shows

the displacement in the vertical z-direction.

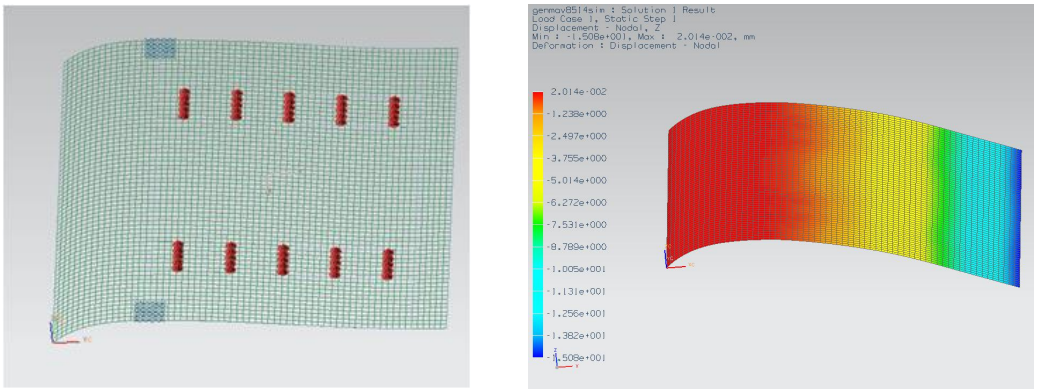

(a) Mesh and Geometry (b) Solution Z-displacement

Figure 6.13: Finite element model and solution of 8514 MFC GenMAV airfoil deflection

Table 6.4: Displacement comparison for GenMAV verification test case

	Finite Element Model	Experiment
Displacement(mm)	11.73	9.22

Table 6.4 shows the deflections for the experiment and those from the finite element. As seen in Figure 6.11, the laser measured vertical z-direction displacement of a point just in-board of the trailing edge. Thus, the finite element value of displacement is at a node an equal distance from the trailing edge.

While the experiment differs from the finite element model by approximately 2.5 mm or approximately 20%, the model does get close. The reason for the difference is likely due to two main issues: inherent problems with fabrication and problems with the thermal analogy itself. During fabrication, the exact ratios of fiber to epoxy are not going to be the same as predicted. This will cause the material properties of the laminate to be different than the model. In addition, the thicknesses vary slightly and deflection is very sensitive to thickness[5]. The other key source of error is inherent in the model itself. The thermal analogy is a simplification of a complex nonlinear process. Through experimentation, hysteresis and

creep behaviors have been found to significantly affect measured deflections[6]. Creep by itself adds can error on the order of a few millimeters. Also, it is possible the electric fields from the individual MFC patches interfere with one another[5].

However, while the finite element model has the above mentioned sources of error, these issues will be constant between test cases. Thus, while the absolute deflection could be slightly different, the comparisons should still be accurate.

6.5 Vortex Lattice Model for Aeroelasticity Solution

The goal of the vortex lattice model and solution is to find the aerodynamic forces that are created when the deformed wing of the finite element model is in flight. The aerodynamic forces give a measure to evaluate the effectiveness of a certain MFC actuation configuration. The amount of roll moment, lift, drag and other important measures of wing performance can all be calculated from a flow solution. In addition, the aerodynamic forces can then be added to the finite element to get a new deflection pattern. Repeating the process, the wing will converge to a certain deflection and have aeroloads associated with that deflection.

This is common technique in aerodynamic design and thus there exist a wide assortment of computer programs which can solve for aerodynamic forces given an airplane's geometry. Many of these programs are readily available in the public domain and several researchers have done extensive analysis into each programs and their relative accuracy and application[17]. Two of these programs are Xfoil and Athena Vortex Lattice (AVL) developed by Drela and Youngren[25]. AVL uses a finite element flow technique called vortex lattice which is described in more detail below while Xfoil is a panel method code. Xfoil solves for 2-D flow around airfoils while AVL is designed for 3-D solutions around entire wings and airplanes[25].

6.5.1 Vortex Lattice Method

Vortex Lattice is essentially a finite element method of flow analysis. A brief overview of the primary assumptions of the technique will be discussed here, but Bertin and Smith gives a much more in depth derivation of the process[26]. First, the equations of motion for flow around wing are simplified with a few key assumptions. The flow is assumed to be inviscid and incompressible over an infinitely thin wing. The wing or airplane surface is modeled as a mesh of vortices with zero thickness. As discussed in Bertin and Smith, the boundary conditions are used to solve for the forces and flow velocities associated with each vortex element. The primary boundary condition is that flow does not go through the surface at these vortices. There are many more details to the solution process which are outside the scope of this paper[26].

The assumptions of vortex lattice are both important and limiting for a UAV of the size discussed in the presented research. Here the UAV is flying in air at a cruise velocity of approximately 13 m/s and a Reynold's number of approximately 10^5. The thickness is also 0.5 mm with 127 mm chord and 610 mm span. In these conditions, incompressibility and no thickness effects are likely good approximations, but inviscid flow is likely not true. In fact, viscous effects are very significant at this Reynold's number. In particular viscous drag, or friction drag, is likely the main component of total drag. However, as long as these effects can be calculated and added later, vortex lattice can give a good approximation[26]. Viscous effects are primarily affected by surface finish and wetted surface area. The total forces should be a combination of inviscid forces from vortex lattice plus a viscous term which is only a function of area and surface finish[10]. Thus, if two test cases with similar surfaces and areas are analyzed with vortex lattice, both should give results with the same error due to viscous effects. All test cases in the presented study have the same area and surface finish will be assumed the same when fabricated.

6.5.2 Athena Vortex Lattice

Athena Vortex Lattice (AVL) is a program developed by Drela and Youngren[25]. The program accepts text files as an input. These properly formatted text files represent the geometry of the model. With these input files, AVL can generate an assortment of run cases to test the airplane model under different flight conditions. After defining the geometry and flight conditions, AVL solves the system to output the aerodynamic force created at each vortex in the model. With these forces, AVL calculates all aerodynamic coefficients such as the coefficient of lift, drag, and roll. AVL was used for this study due to its ability to model complex geometry and solve for 3-D flow. Figure 6.14 shows a block diagram of the process of creating and solving a model in AVL.

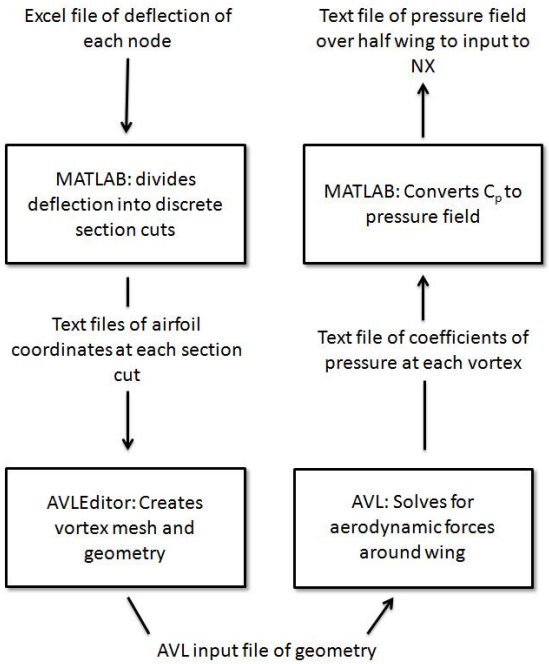

Figure 6.14: Block diagram of creating and solving a model in AVL

Creating AVL Input Files

In order to run simulations in AVL, the geometry from the finite element solver, NX, must be transferred to a format that can be understood by AVL. Generating the geometry in AVL is a complicated process. AVL allows for complex wing geometry that can vary in both spanwise and chordwise directions. Figure 6.15 shows the coordinate system AVL uses for geometry. The center of this coordinate system is the wingspan midpoint at the leading edge. The x-axis runs parallel to the flow. The y-axis is along the wing LE, and the z-axis is up to complete the right handed coordinate system.

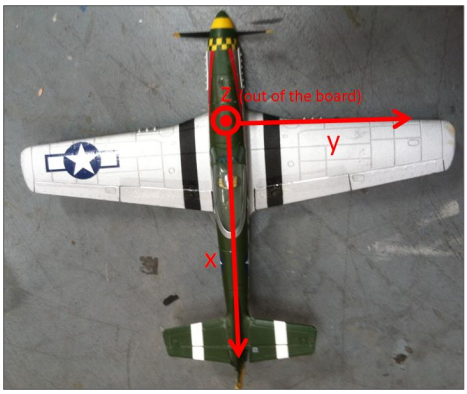

Figure 6.15: AVL coordinate system for a typical aircraft

The geometry definition process is done by defining discrete section cuts along the wing span, y-direction. A text file then defines the airfoil profile at each section cut. The airfoil text file is a series of x and z coordinate pairs. AVL fits a spline to these coordinates at the particular y-coordinate of the section cut. AVL then interpolates between the section cuts to create a smooth continuous surface. Figure 6.16 shows the coordinates of a couple typical section cut profiles.

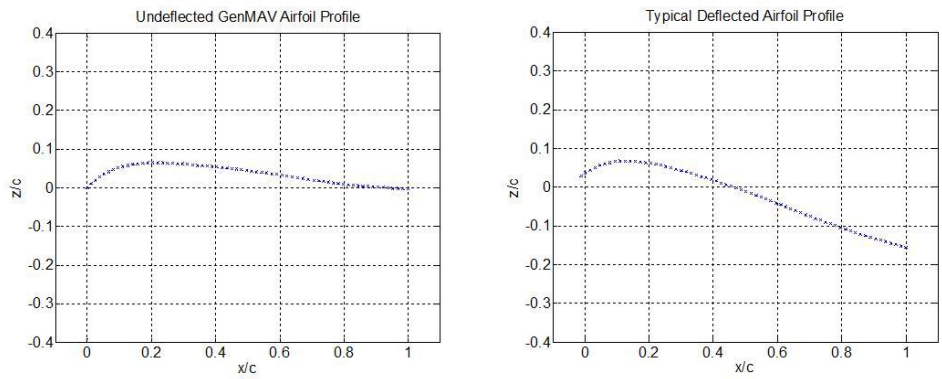

Figure 6.16: Typical airfoil profiles from section cuts of deflection pattern

The location and displacement of each node in the NX finite element model was outputted to an Excel file. A program was written in MATLAB which read this Excel file. The MATLAB program then divides the wing into many section cuts and creates a text file with airfoil coordinates for each section cut. Each text file is also labeled with its spanwise location. One hundred section cuts were created for each side of the wing.

The section cuts were then inputted into a program called AVLEditor. AVLEditor is graphical user interface developed by Cloud Cap Technology which creates properly formatted geometry files for export to AVL[27]. The AVLEditor user interface is shown in Figure 6.17. The geometry shown in the user interface is an estimate of what AVL reads.

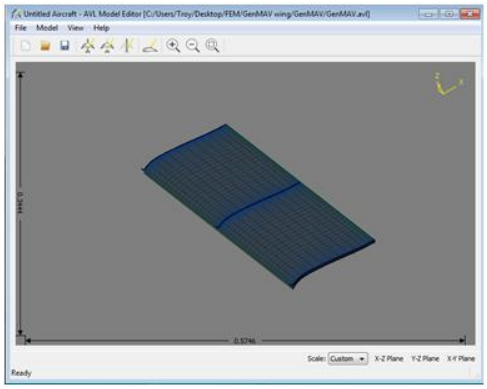

Figure 6.17: User interface and example model with AVLEditor

An issue was found while generating complicated wing shapes in this manner. While AVL

allows for complex geometry, it is limited to some degree. The limitations of the function which fits splines to airfoil coordinates and the tedious nature of the input process meant that not all 100 section cuts of each wing half could be inputted into AVL geometry. A typical AVL geometry file ended up containing around 30-40 section cuts. Care was taken to model areas with a greater density of section cuts where the airfoil profile changed the most compared to areas of mostly constant airfoil profile. However, this discretization process limited the resolution of the geometry to approximately 1 mm. Figure 6.18 shows an example of wing geometry that is ready for export to AVL.

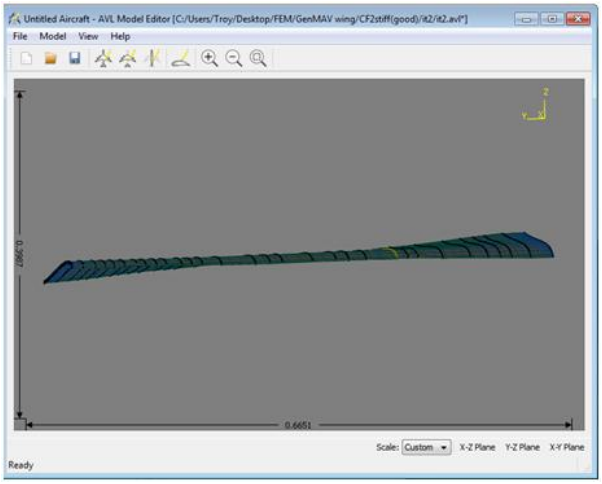

Figure 6.18: Typical deflected wing geometry for input to AVL

Running an AVL Simulation

After creating the wing surface geometry in AVLEditor, the geometry was inputted into AVL and the surface was divided into discrete vortices. All simulations in this study were run with 12 vortices in the chordwise and 64 in the spanwise direction over the entire 2 ft wing. These vortices were spaced in cosine-scaled spacing which concentrated the vortices in areas of rapid flow change such as the leading and trailing edges and the outboard wing tips. Concentrating the vortices near areas of rapid change increases the solution accuracy [25].

The geometry file including vortex spacing was then opened in AVL. AVL then plots the geometry to check for errors. A typical geometry plot is shown in Figure 6.19. The green lines show the camber of the thin wing. Each line represents a line of vortices so as can be seen the vortices are dense near the wing tips. The pink and white plane illustrates the location of the leading edge and the vortex spacing. The scale is in meters. The flight conditions to be modeled were then inputted into the simulation. All test cases were run with an angle of attack and sideslip angle of 0 degrees and a cruise velocity of 13 m/s.

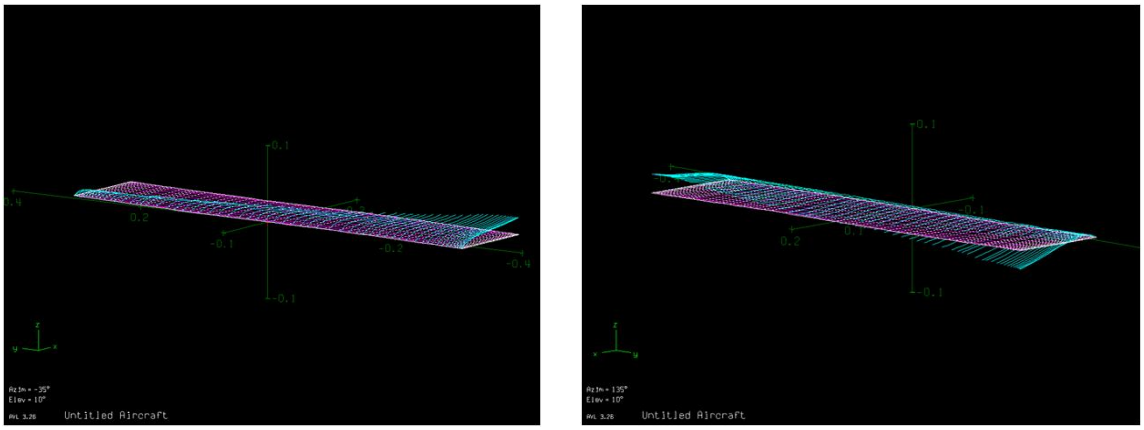

(a) View of LE (b) View of TE

Figure 6.19: Example of a geometry plot from AVL

AVL Output and Conversion to NX Pressure Loading

AVL then solves for aerodynamic forces at each vortex. The actual output of AVL is all in terms of aerodynamic coefficients which scales the force by wing area and dynamic pressure. The total force coefficients in each principal direction and total moment coefficients about each principal axis were outputted. In addition, these force and moment coefficients were outputted as a function of spanwise location. Most importantly, the pressure coefficient at the location of each vortex was calculated.

The pressure coefficients, C_p, at each vortex were exported to a text file. A MATLAB code was written which read this text file and converted the C_p at each vortex to a spatial map

of pressure. The conversion was done by the equation below from Bertin and Smith[26].

$\Delta P = \frac{1}{2} V_\infty^2 \rho_\infty C_p$

Where:

ΔP = Gauge pressure at the given vortex location

V_∞ = Free-stream velocity, 13 m/s was used as the expected cruise velocity for this aircraft

ρ_∞ = Free-stream density of the fluid in this case air

C_p = Coefficient of pressure at each vortex

After conversion, the spatial map of pressures was saved a text file. This text file was imported into NX and used to define a pressure load.

6.6 AVL Verification

In order to verify the accuracy of the model, the aerodynamic data generated from AVL checked against 2-D wind tunnel data and 2-D simulations in the literature. The model chosen was a simple undeflected GenMAV airfoil profile. For the AVL case, the wing was made with a large aspect ratio of 158 so the result should approximate 2-D flow. The calculated lift coefficient as a function of angle of attack is compared to experimental results and a 2-D simulation.

Xfoil is a 2-D flow simulation program that is well-established in literature [5] and [17]. The Xfoil data presented here is for an undeflected 2-D GenMAV airfoil and is from Gustafson[5].

The experimental data is from 2 separate 2-D wind tunnel tests: one testing a GenMAV airfoil with 2 8528 MFC bimorphs and another testing a GenMAV airfoil with 2 8514 MFC bimorphs. These tests are discussed in Section 3.2. For both experimental results in Figure 6.20, the airfoils are at decreasing 0% actuation case and at 13 m/s. The Xfoil data is from [5] and was calculated at 10 m/s. The AVL data was calculated with 13 m/s wind speed.

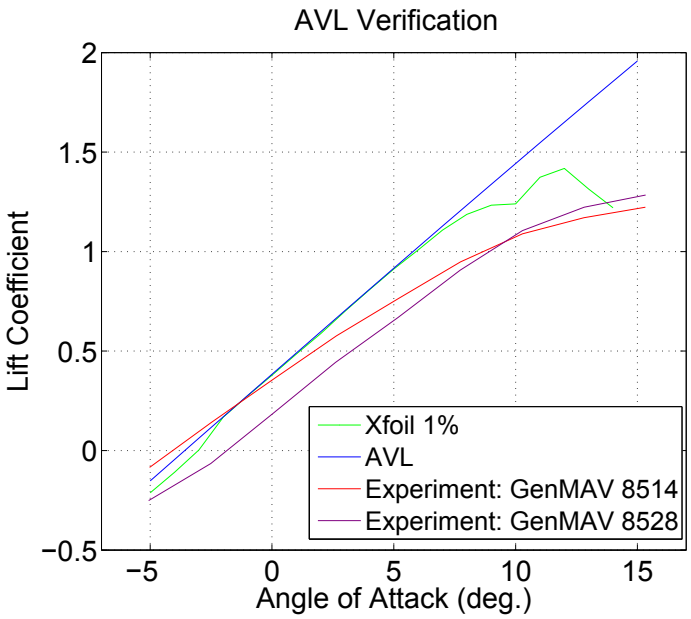

Figure 6.20: Plot comparing the lift coefficient from different sources for a GenMAV airfoil. Xfoil data is from Gustafson[5]

Comparison

From Figure 6.20, it can be seen that the AVL result matches very well with the verified Xfoil data from the literature. Both of these match the experimental data considering that the real airfoils deflect under aeroloads. The aeroload-deflected airfoils produce slightly less lift. The 8528 (x2) airfoil with larger MFC area maintains its shape slightly better, which increases its lift. AVL does not model flow separation and stall so the stall behavior is absent at high angles of attack.

Chapter 7

Full Wing Morphing Simulation Results

7.1 Design Comparison Procedure

Now that a model has been developed and verified, there is a means to look at how different parameters affect the morphing performance of the wing. As listed below, there are several key parameters which affect the deflection and ability to withstand aerodynamic loading. The purpose of this study is to look at a few of these parameters and compare how they affect morphing. As discussed previously, part of the advantage of morphing with MFCs is design freedom and number of different ways this can be implemented. However, the large freedom also means a comprehensive study into each parameter would take a tremendous amount of time and resources. In order make the design space more manageable a few assumptions and limitations were imposed on the list below. It also must be noted that while all figures show only half the wing, both halves were used in the calculation of the roll coefficient with one side deflecting up and the other deflecting down. Deflections in figures are for downward cases but the upward case deflections are proportional and have the same pattern.

7.1.1 List of Parameters

This section lists the key parameters that affect morphing and describes how each was taken into account in these simulations. Some of the parameters were varied and evaluated through a series of simulations. Other parameters were held constant based on work by previous researchers. Each parameter is listed and described below. The descriptions include how the parameter was varied or at what value it was set and why.

1. Undeflected airfoil profile
2. Number of MFC actuators
3. Size of MFC actuators
4. Actuator orientation relative to chord line
5. Actuator location on chord line
6. Actuator location along span
7. Composite substrate material
8. Composite substrate thickness
9. Composite substrate orientation schedule

Descriptions of comparisons completed and associated assumptions:

1. The undeflected airfoil profile was restricted to always be a GenMAV airfoil whose coordinates were developed in Stewart et al. [10]. This airfoil was developed for the purpose of comparing different MAV technology and allows for comparisons to experimental data already developed on this project. Figure 3.10 shows the GenMAV profile.

2. Number of actuators was limited to one or two MFC bimorphs with the total MFC area limited to the equivalent of one 85 mm by 57 mm MFC. This limitation was done for two reasons. First, the MFCs are dense in comparison to the substrate and thus

there is a goal to minimize weight in order to achieve wing that is not too heavy to fly. Second, a simple geometry is easier to fabricate and employing many tiny actuators could be difficult to locate precisely in fabrication.

3. The size of the MFC actuators was thus also limited to either one 8557 MFC or two 8528 MFC bimorphs. The reason was discussed in 2.

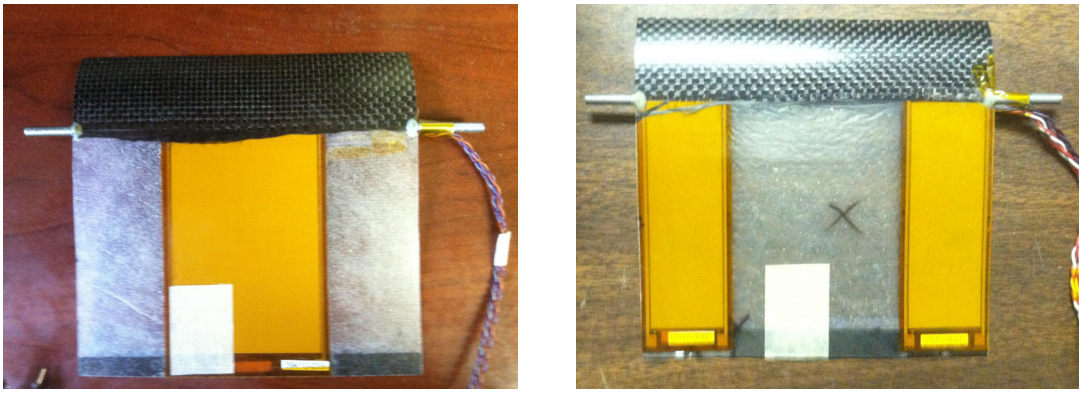

(a) Airfoil with one 8557 MFC (b) Airfoil with two 8528 MFCs

Figure 7.1: Examples of airfoils with different sized MFC bimorphs

4. The actuator orientation relative to the chordline, shown in Figure 7.2 was set at a constant 45 degrees of all test cases. This is parameter was chosen in an attempt maximize deflection while maintaining spanwise and chordwise stiffness against aeroloads. However, in future work this is one parameter that could be investigated in more depth.

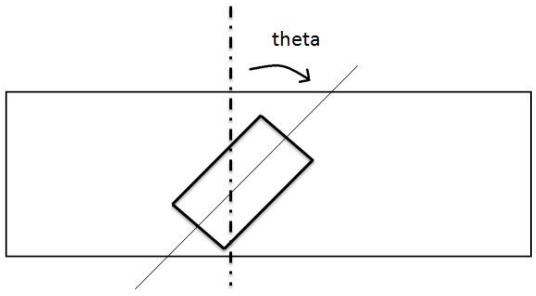

Figure 7.2: Diagram of the variation of the angle of the actuator with chordline

5. The location along the chord was chosen to be constant for all test cases. The leading

edge of the MFC bimorph was chosen to be as close as possible to the quarter chord location. Gustafson showed this location gave the greatest deflection, but his work was centered on aileron-like control surfaces with actuators parallel to the chord[5]. This parameter would be an interesting possibility in future work.

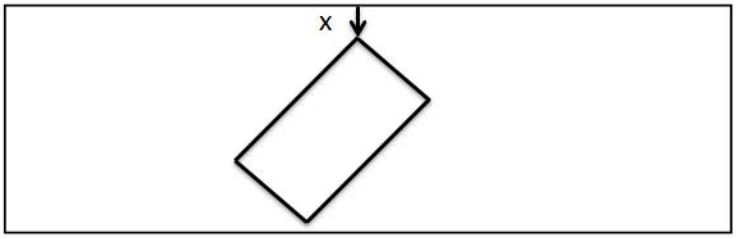

Figure 7.3: Diagram of actuator's chordwise actuator location on wing

6. The location along span, as shown in Figure 7.5 is a parameter which will be investigated in some detail. See Section 7.3.

7. The composite substrate material was limited to carbon fiber or E-glass weave fabric. This allows for a simple comparison of the effects of the substrate's Young's modulus, but a much comprehensive study could be done in the future.

8. The composite substrate thickness was chosen as parameter for a simple comparison. See Section 7.5. The comparison also looks at varying the thickness at different wing locations. Thickness was varied by varying the number of layers. The thickness of a single layer of each material is shown in Table 7.1.

Table 7.1: Thickness value used for one layer of each material

	Carbon Fiber	E-glass	MFC
Thickness (mm)	0.22	0.15	0.30

9. The composite substrate layup schedule was set a constant for all test cases. The substrate weaves were set to 0/90 with fibers in both spanwise and chordwise directions.

This was done to maximize stiffness in chord and span directions against aerodynamic loading. Gustafson also showed that deflection is a maximum with substrate orientation +/-45 degrees relative to the MFC bimorph fibers[5]. Thus, for the 45 deg. actuators in this study, fibers at 0/90 deg. should also produce maximum deflection. This could be looked at in more detail in the future.

7.1.2 Defining Convergence

As discussed before, the methodology of this study was to get deflections, apply aeroloads, get a new deflection, and then get new aeroloads. This is repeated until convergence which is where the deflection does not change significantly with the new aeroloads. This represents the static case where the morphed deflection is able to withstand the aeroloads it creates without further deflection. A key limitation is the geometry resolution discussed in Section 6.5.2. This resolution was approximately 1 mm. Thus, the convergence was defined where the new deflection of the trailing edge wing tip did not change by more than 1 mm from the previous iteration. This geometry limitation also affects the aerodynamic coefficients, adding an uncertainty of approximate 5%. The idea of this study is to create comparisons to between test cases, not to gain the absolute values for the coefficients. Thus while there is some error associated with all steps in the methodology, the error should be constant between test cases.

7.1.3 Performance Measures

The performance in these comparisons is based on the configuration's ability to function as an aileron. Ailerons are primarily responsible for roll so coefficient of rolling moment will be the primary performance measure. Rolling moment coefficient is defined by the following Equation 7.1. Typically, rolling moment coefficient is designated C_l. However, for the purposes of this paper and to avoid confusion with the sectional lift coefficient, the

rolling moment coefficient will be referred to as C_{roll} or just roll coefficient.

Roll coefficient:

$$C_{roll} = \frac{M_x}{QSb} \tag{7.1}$$

Where: M_x = moment about the x-axis, or centerline of the wing parallel to the chord, see Figure 6.15.

q_∞ = dynamic pressure

S = wing area

b = wing span

In addition, the wing needs to be relatively stiff against aerodynamic loading. There are a few reasons this is important. Section 7.8.1 discusses in more detail the importance of this criteria and how it fits within the design decisions. However, initially roll moment will be the primary measure.

7.2 Control Study on Conventional Ailerons

A test case was run to calculate the roll coefficient of conventional flapped ailerons. This conventional wing's roll coefficient serves to verify the morphing test cases as it should of a similar order of magnitude. In addition, this gives a basis of comparison for the effectiveness of a morphing surface when actually implemented in a UAV. The conventional wing was thin with 2 ft. wingspan and 5 in. chord. The airfoil profile was an undeflected GenMAV across the entire slap. An aileron control surface was defined which extended 5.25 in. from each wing tip. The control surface was 30% of the chord. Previous conventional flap comparison tests on this project use this control surface geometry. This geometry was inputted into AVL and the result is shown in Figure 25. The control surfaces were deflected asymmetrically 15 degrees up or down.

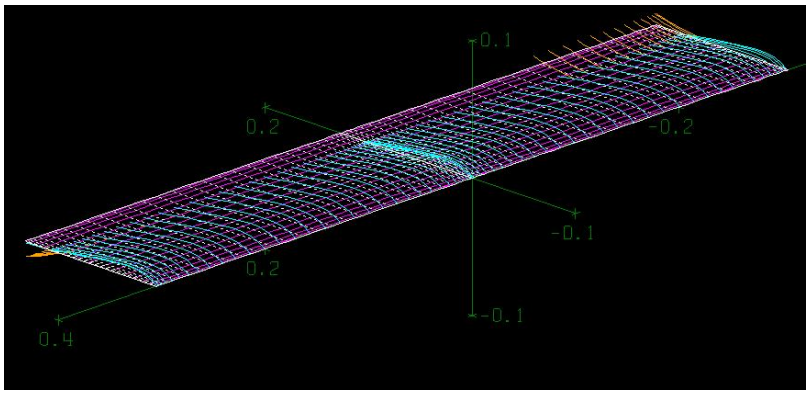

(a) View of LE

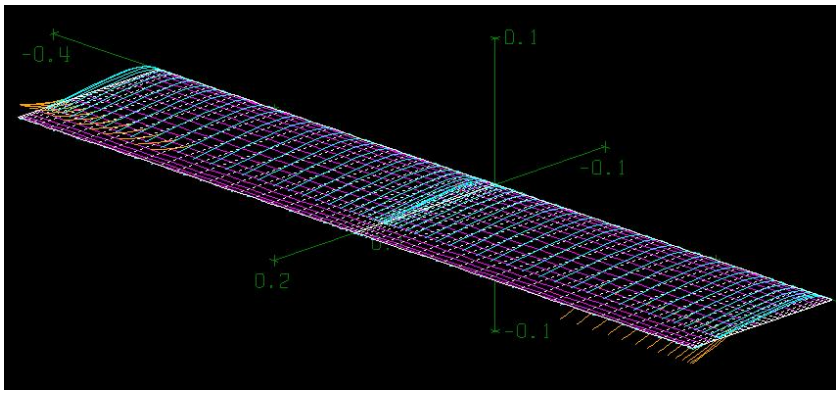

(b) View of TE

Figure 7.4: AVL geometry of GenMAV wing with conventional ailerons

For ±15 deg deflection of these conventional 30% chord ailerons:

Roll coefficient = 0.0670

7.3 Span Location Comparison

The first study looked at the placement of the actuator in the spanwise direction. The following variables were all fixed for all test cases in addition to the fixed parameters mentioned in Section 7.1.1:

- Composite substrate schedule (see Figure 7.5)

- One MFC actuator, 85 mm by 57 mm
- Chordwise location (see Figure 7.5)

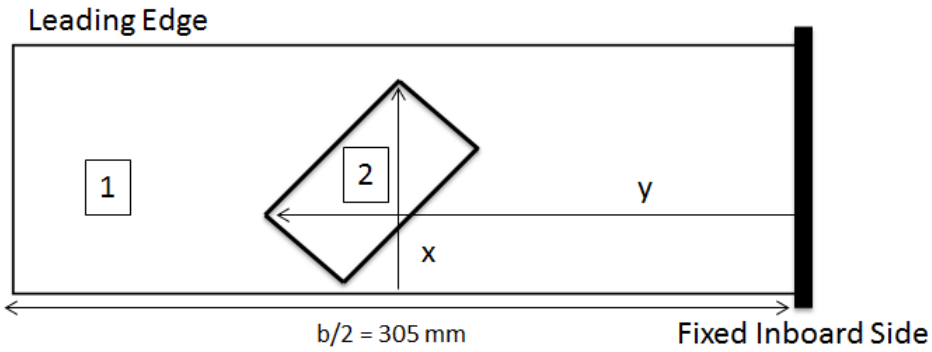

1: 2 layers 0/90 CF, [0-90 CF / 0-90 CF]

2: 2 layers 0/90 CF between a bimorph, [MFC / 0-90 CF / 0-90 CF / MFC]

X = 106 mm (close as possible to quarter chord)

Figure 7.5: Diagram of spanwise actuator placement on wing

While the figure only shows half the wing, the entire wing with one side deflecting up and the other deflecting down was used. Five test cases were run varying y from the most inboard possible, y = 110 mm, to most outboard, y = 300 mm.

Table 7.2: Roll coefficient associated with span location

y (mm)	Roll Coefficient
110	0.0558
160	0.0735
200	0.0751
250	0.0700
300	0.0525

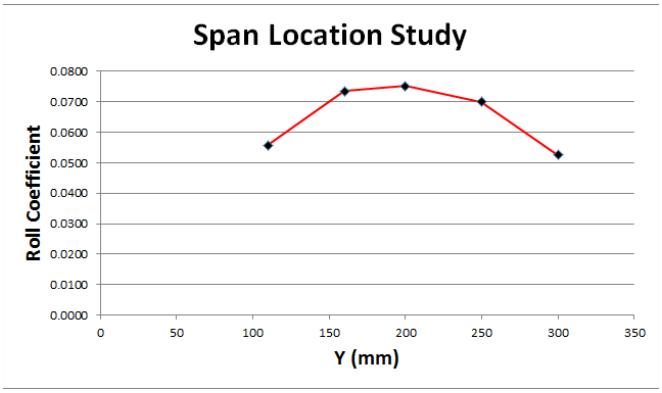

Figure 7.6: Plot of roll coefficient vs. spanwise location

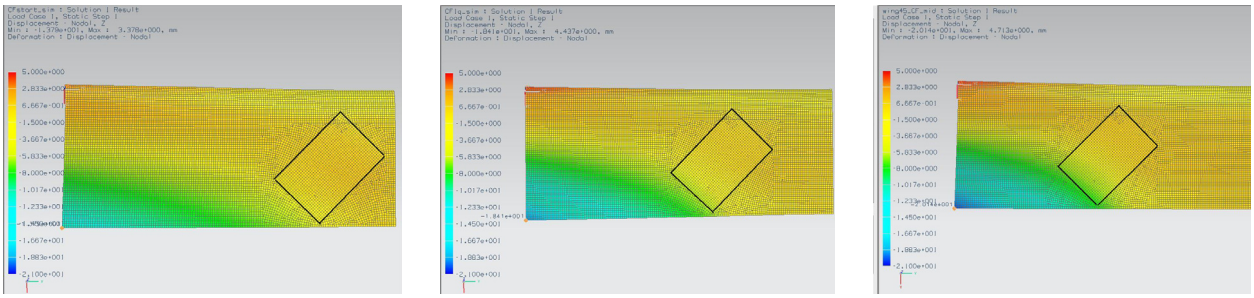

(a) y = 110 mm (b) y = 160 mm (c) y = 200 mm

(d) y = 250 mm (e) y = 300 mm

Figure 7.7: Deflection results for span location study after convergence. Actuators are outlined to highlight location.

Conclusion

From Table 7.2, it can be seen that as the actuator moves from inboard to outboard, the roll coefficient increases and then decreases reaching a maximum around y = 200 mm. This y value is where the actuator center is near the center of the wing. The maximum roll

coefficient is 0.0814. This parabolic behavior makes sense looking at the deflection patterns. An actuator at the tip creates large maximum displacement at the tip. However an actuator near the fixed inboard side creates lower magnitude displacement over a larger region. It then follows that the maximum occurs in the middle as here it is a mix of large magnitude over a large area. Aeroelastic differences are discussed in more detail in Section 7.8.1, but there was not a significant difference between the induced deflections.

7.4 Two Actuators Location Comparison

From the spanwise location study above, it can be seen that there is an advantage to maximizing the area of the wing that is deflected which also follows logically. Thus this comparison looks at the effects of breaking up the one 85 mm by 57 mm actuator into two 85 mm by 28 mm actuators which spreads the actuation over a larger area. This also allows many more possible actuator placements as each can move spanwise in an absolute sense and relative to each other. This study was limited to 3 test cases which are described below:

- **End/start**: one actuator is placed as close to inboard and the other as close to outboard as is reasonable
- **End/mid**: one actuator is placed close to the outboard edge and the other approximately the center of the wing
- **Mid/mid**: both actuators are placed towards the middle of the wind with each being approximately equidistant from the midpoint of the wing

The actual geometry is shown in Table 7.3 and Figure 7.8. The fixed parameters from Section 7.1.1 remained fixed with the following also true of each test case:

- Constant composite substrate schedule (see Figure 7.8)
- Two MFC actuators, 85 mm by 28 mm

- Constant chordwise location (see Figure 7.8)

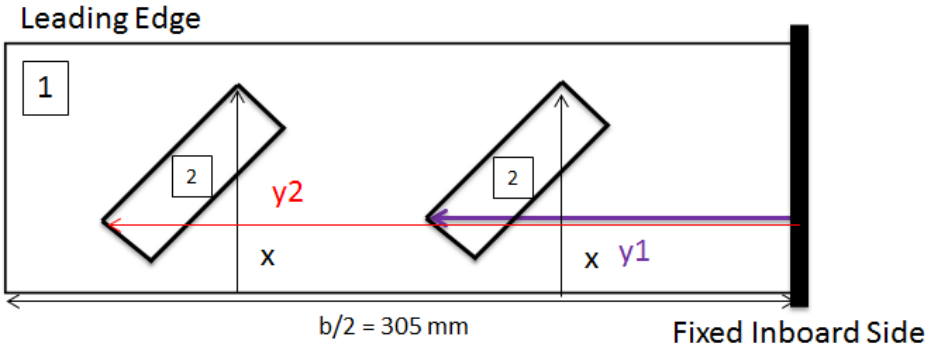

1: 2 layers 0/90 CF, [0-90 CF / 0-90 CF]

2: 2 layers 0/90 CF between a bimorph, [MFC / 0-90 CF / 0-90 CF / MFC]

X = 86 mm

Figure 7.8: Diagram of actuator placement on wing for two actuator simulations

Table 7.3: Roll coefficient for two actuator simulations

Test Case	y1 (mm)	y2 (mm)	Roll Coefficient
end/start	90	300	0.0692
end/mid	195	300	0.0655
mid/mid	130	250	0.0814

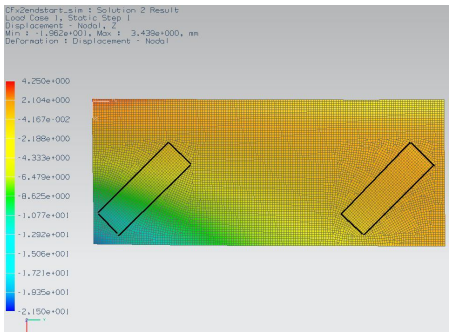

(a) End/start

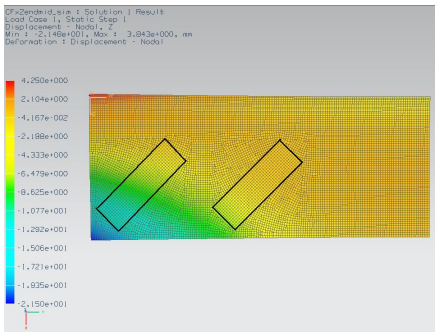

(b) End/mid

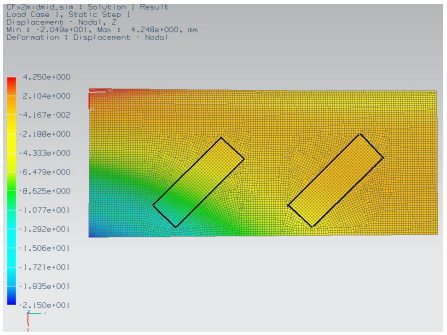

(c) Mid/mid

Figure 7.9: Deflections of two actuator test cases after convergence. The actuators are outlined to highlight their location.

Conclusion

From Table 7.3, splitting the one large actuator into 2 small actuators worked to increase the roll coefficient. With two actuators, the deflections were larger in magnitude and over a larger area. Placing the actuators at the extremes worked slightly better than placing both toward the wing tip. However, the slight difference is likely within the uncertainty the modeling process. Placing both actuators bracketing the centerline produced a significant increase in roll coefficient. With one large actuator, the middle produced the best case. Thus, it follows that maximizing the actuation in the center section of the wing also produced the best results.

7.5 Thickness Comparison

The next parameter to be investigated is the effect of substrate thickness. For this study, the Mid/mid test case from the two actuator comparison was used as a baseline. In order to test the thickness, instead of 2 layers of carbon fiber (CF), 3 layers were modeled for the entire wing surface. From Table 7.1, the thickness of each layer of CF after fabrication is approximated as 0.22 mm. All other parameters were held constant from the Mid/mid test case.

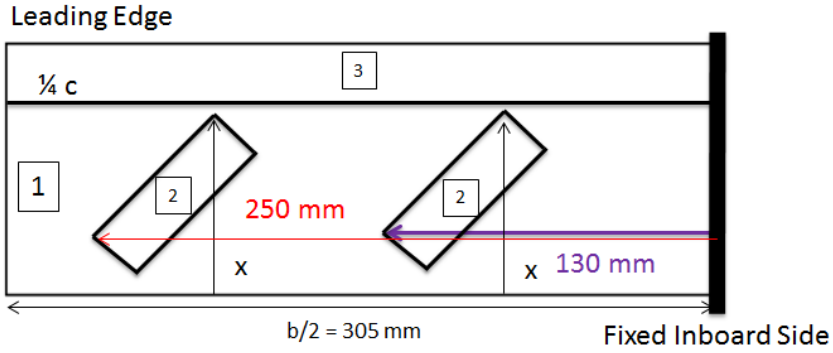

1: 3 layers 0/90 CF, [0-90 CF / 0-90 CF / 0-90 CF]

2: 3 layers 0/90 CF between a bimorph, [MFC / 0-90 CF / 0-90 CF / 0-90 CF / MFC]

X = 86 mm

Figure 7.10: Diagram of actuator placement on wing for increased thickness simulation

Table 7.4: Roll coefficient as a function of substrate thicknes

Test Case	Substrate Thickness (mm)	Roll Coefficient
2 layers CF	0.44	0.0814
3 layers CF	0.66	0.0585

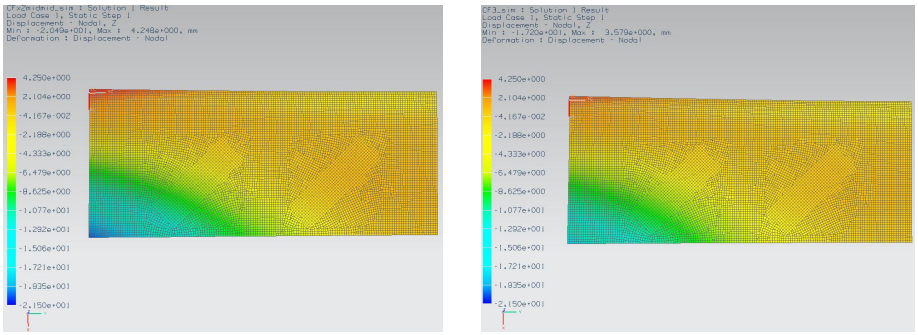

(a) Two layers CF (b) Three layers CF

Figure 7.11: Deflections for thickness comparison after convergence

Conclusion

Increasing the thickness overall substantial decreased the wing displacement. The decrease was roughly proportional across the entire area, and was reflected in a significantly decreased roll coefficient. The roll coefficient decreased by approximately 28%. This result is consistent with theory as the stiffness would be larger with more thickness, and agrees with literature as deflection should substantially decrease with thickness[5]. However, there are advantages to a less flexible wing towards aeroelastic effects which could justify the increased thickness. This is discussed in detail in Section 7.8.1.

7.6 Material Stiffness Comparison

Another parameter of interest is material stiffness and how it affects the roll coefficient. For this study the Mid/mid case of Section 7.4 was used. In order to keep constant thickness, 3 layers of E-glass were used as 3 layers of E-glass is approximately the same thickness as 2 layers of CF. All parameters and geometries were the same as this case except instead of carbon fiber, the substrate material was fiberglass, E-glass. See Figure 7.10 for a diagram and replace CF with E-glass where necessary for this case.

Table 7.5: Roll coefficient comparison for different material substrates

Test Case	Thickness (mm)	Elastic Modulus (MPa)	Roll Coefficient
2 layers CF	0.44	63720	0.0814
3 layers E-glass	0.45	23710	0.0898

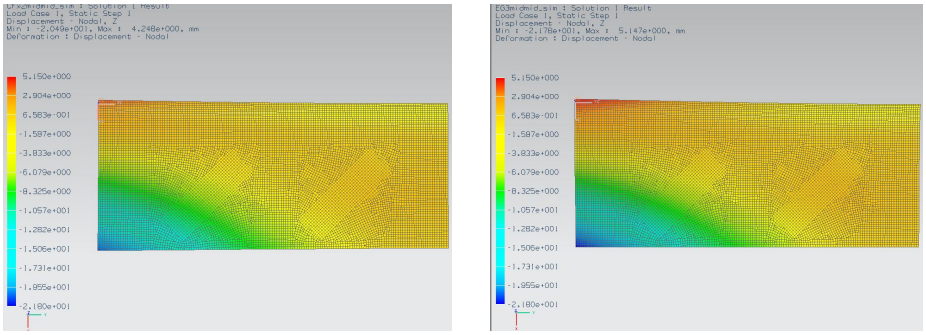

(a) Two layers CF (b) Three layers CF

Figure 7.12: Deflections for material stiffness comparison after convergence

Conclusion

As expected the more flexible E-glass allowed for more deflection proportionally over the whole surface and thus a larger roll coefficient. However, the roll coefficient only increased by approximately 10%. Despite a substantial decrease in material elastic stiffness, the roll coefficient was only increased a small amount. Part of the reason behind this is that much of the increased deflection with E-glass was negated by the effect of aerodynamic loads. This large aeroelastic penalty and its effects are discussed in Section 7.8.1.

7.7 Leading Edge Stiffener Comparison

An advantage of embedded MFCs and in the use of composites in general is ability to vary the composite layup as a function of location on the wing. This study examines the effects of varying the thickness on the leading edge (LE). The idea is that this added thickness

acts as a stiffener to support the aerodynamic loads on the leading edge while maintaining a flexible wing to allow large deflection and camber change. From plotting the aerodynamic forces of the previous test cases, it is apparent that the leading quarter of the wing is where a large fraction of the aerodynamic loads are applied. Thus, for this study, using the same geometry from Mid/mid test case of Section 7.4, a third layer of CF substrate was applied to the area from the leading edge to the quarter chord line along the entire span.

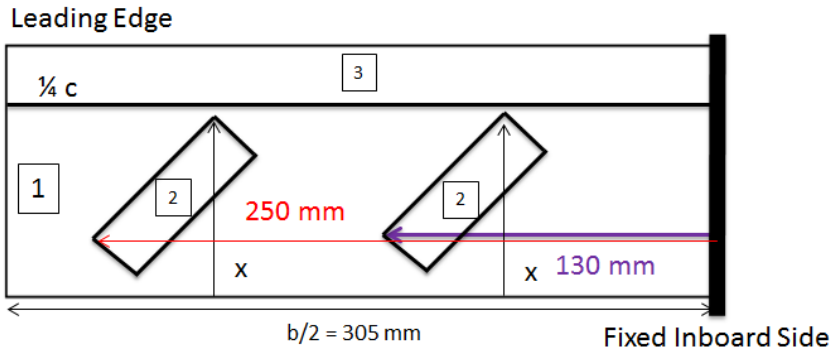

1: 2 layers 0/90 CF, [0-90 CF / 0-90 CF]

2: 2 layers 0/90 CF between a bimorph, [MFC / 0-90 CF / 0-90 CF / MFC]

3: 3 layers 0/90 CF, [0-90 CF / 0-90 CF / 0-90 CF]

X = 86 mm

Figure 7.13: Diagram of test case with leading edge stiffener

Table 7.6: Roll coefficient comparison with LE stiffener

Test Case	Roll Coefficient
2 layers CF	0.0814
3 layers CF	0.0585
2 layers CF w/ LE stiff	0.0747

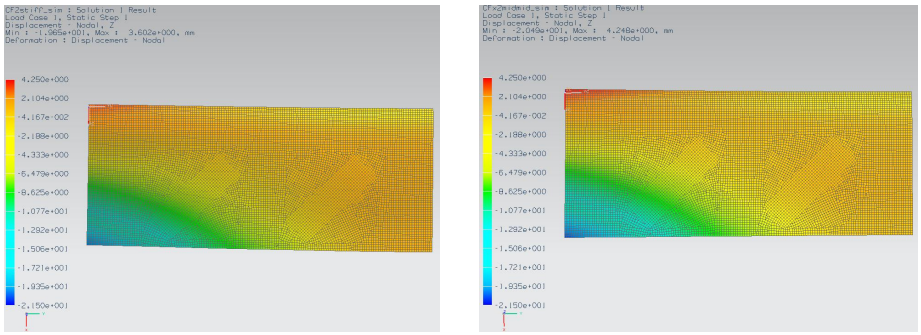

(a) With LE stiffener (b) No LE stiffener

Figure 7.14: Deflection LE stiffener comparison after convergence

Conclusion

As shown in Table 7.6, the LE stiffener decreased the roll coefficient by approximately 8%. This decrease is significantly less than the decrease with the entire wing having 3 layers. Comparing the displacement in Figure 7.14, the stiffener reduces the overall deflection slightly and especially near leading edge. However, this deflection change is small particularly when compared to the change associated with 3 layers over the entire wing. If more stiffness is required, a LE stiffener could be a good way to add it.

7.8 Discussion of the Results

There are two important measures for assessing the performance of these ability to actuate roll and ability to maintain shape against aerodynamic loading. The preceding sections provided comparisons of roll coefficient and thus of the ability to actuate roll. The more challenging performance measure is the suitability to aeroelastic deformation.

7.8.1 Aeroelastic Comparisons

Here the effect of the aerodynamic loading will be quantified by comparing the trailing edge wing tip deflection with aerodynamic loads to the deflection without them. The trailing edge wing tip is also the maximum deflection location for all test cases. In general, aerodynamic loads affect a particular location on the wing roughly proportionally to the displacement at the tip. The effect on the trailing edge wing tip will be indicative as this is the area most susceptible. It is the least stiff point geometrically and the furthest from the fixed boundary condition. While this is only an approximation, the effect on the entire wing surface would be difficult to compare.

In addition, only the downward-deflected half of the wing surface will be considered. The upward deflected surface experiences loads which are significantly less on the order of a third of the downward deflection forces. The effect should also be proportional. The test case where the wing is stiffest against aeroloads will be the least affected in both upward and downward actuations. Table 7.7 gives a good summation of the results for each test case. The configuration which changes the least under aeroloads is the case with 3 layers of CF while the largest change occurs with 3 layers of E-glass.

Table 7.7: Comparison for all full wing morphing test cases with aeroelastic deflections

Wing Tip displacement, magnitude: downward case, (mm)

Test Case Number	Brief Description	Roll Coefficient	No aeroloads	After convergence	Difference
1	Span study: 1 8557, inboard	0.0558	17.56	13.84	3.72
2	Span study: 1 8557, 1/4 span	0.0735	22.20	18.48	3.72
3	Span study: 1 8557, middle	0.0751	23.98	20.22	3.76
4	Span study: 1 8557, 3/4 span	0.0700	24.27	21.08	3.19
5	Span study: 1 8557, outboard	0.0525	22.91	19.40	3.51
6	2 8528: End/start	0.0692	23.84	19.69	4.15
7	2 8528: End/mid	0.0655	25.76	21.56	4.20
8	2 8528: mid/mid	0.0814	25.22	20.57	4.65
9	Mid/mid: 3 layers CF	0.0585	18.94	17.26	1.68
10	Mid/mid: E-glass	0.0898	30.37	21.87	8.50
11	Mid/mid: 2 layers, w/ LE stiff	0.0747	23.61	19.71	3.90

Span location comparison

Looking only at span location of the actuator, the difference is constant until the actuator approaches the tip. The minimal difference then occurs at an actuator location about 3/4 of the span from inboard. From the plots of aerodynamic loads, the largest loads occur not at the tip, but slightly inboard due to 3-D tip effects. The MFC bimorphs add stiffness so it makes sense that adding the stiffness where the most load occurs produces the most stiffness against aerodynamic loading.

Two actuator comparison

Splitting the large actuator into 2 smaller actuators did increase the roll coefficient, but there is a penalty as the wing was more susceptible to aeroloads. However, the 4 mm range of difference is not prohibitively large. It is likely beneficial to take the increased roll coefficient in these configurations and give up the stiffness.

Thickness comparison

As expected the 3 layer CF test case was by far the stiffest and had the least difference at 1.68 mm. However, the roll coefficient was significantly reduced. Increasing the thickness gives a means for adding stiffness but the roll coefficient penalty is sizable.

Substrate material comparison

Comparing the 2 layer CF Mid/mid test case versus the 3 layer E-glass test case which had equal thicknesses also gave an interesting result. The E-glass test case had a large deflection difference, nearly double the other test cases, but did improve the roll coefficient. However, the roll improvement was only marginal compared to the flexibility penalty. This implies that material stiffness is important to aeroload rigidity but not as important to improved roll coefficient. Thus, the best design is likely maximizing the material stiffness.

Stiffener Comparison

The stiffener test case showed that stiffeners can be a way to improve aeroload rigidity while

maintaining good roll coefficient. Compared to test case 8, the stiffener test case, 11, showed a decrease in aeroload-induced deflection and had an only slightly reduced roll coefficient.

7.8.2 Model Limitations

The goal of this paper was to examine the effects of different parameters on morphing, and with this goal, a few assumptions were made. These assumptions mean the model has a few inherent limitations that must be accounted for when designing a morphing wing. First, the analysis present here is for static loads at zero angle of attack. This method allows for comparisons and convergence, but an aircraft undergoing complex maneuvers and flight conditions will experience aerodynamic loadings in far excess of the loadings presented here. Second, a common issue that plagues aircraft with aeroelastic surfaces is flutter. Flutter is the uncontrolled and often large vibrations of wing surfaces caused by the wings resonating with the forces of the flow. Flutter can be devastating for an aircraft causing loss of control or even structural failure[28]. The model presented here does not account for flutter possibilities. As a result of these limitations it is better to side with caution and over-stiffening the wing versus maximizing roll coefficient.

Another consideration that is not addressed here is weight. An 8557 MFC actuator or two 8528 MFC actuators are a relatively heavy for a small UAV control system. There may be a need to decrease weight to make morphing wings a practical solution. In addition, the effect of actuator placement on moment of inertias was not considered. Actuators further from the center of mass could be better at creating roll, but the increased moment of inertia of being further out may offset any advantage.

7.9 Comparing to Flight Testing Results

In parallel with the research presented here, several flight tests were done on various airframes and wing and control surface configurations. The flight tests were designed and performed by researchers from AVID LLC. and Virginia Tech's Unmanned Systems Laboratory. As part of these experiments, a thin GenMAV wing was included as one of the wing configurations. This thin wing was fabricated based on the research and simulations presented in the previous section. The design chosen was the wing with two centrally-located 8528 bimorphs. The substrate is 2 layers of CF throughout with 3 layers along the LE for stiffness. This configuration is discussed in detail in Section 7.7.

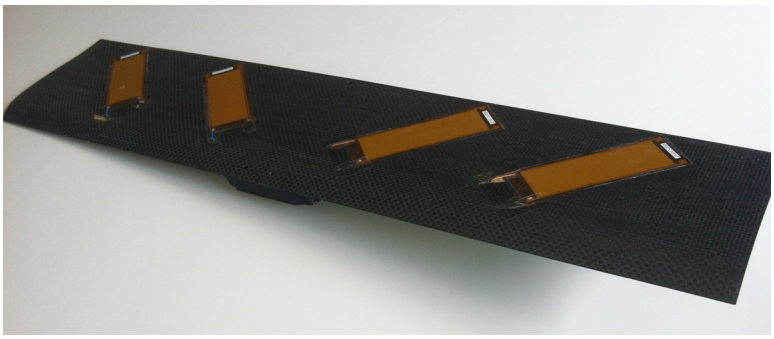

Figure 7.15: Picture of the thin GenMAV full morphing wing

This thin flight wing was tested to evaluate the methodology of the previously discussed simulations. However, the wing that was built, shown in Figure 7.15, did not perfectly match the wing described in Section 7.7. First, the boundary conditions were different than designed. The original simulation had a perfectly fixed boundary line between the two wing halves. In the actual wing, an adapter had to be built to attach the wing to the fuselage. The adapter, shown in Figure 7.16, restricted the motion of a sizeable area in the center of the wing. The second difference between the design and the actual wing is likely the modulus of elasticity. The CF available during wing construction was slightly different density from what Gustafson used. In addition, the wing shows tiny holes and gaps that imply the volume fraction of epoxy is low relative to the airfoils. Thus, the elastic modulus is somewhat of

an unknown. The last inconsistency between the two is the small difference in geometry developed from the layup process. The thickness and actual location of the MFCs were kept as close to design as possible but did turn out slightly different.

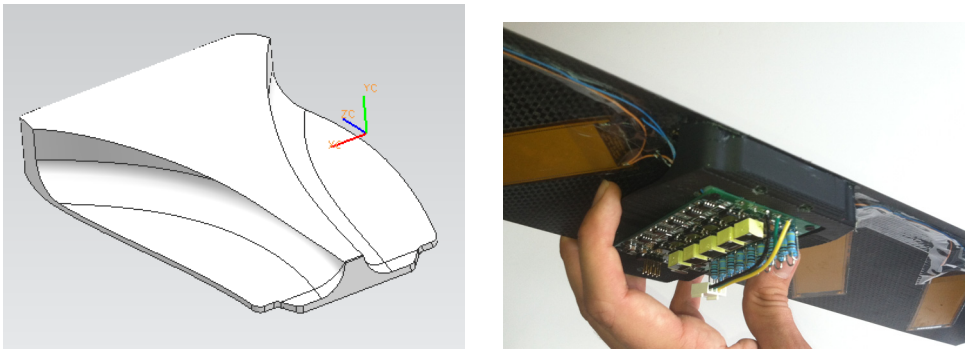

Figure 7.16: CAD model (left) and picture (right) of the adapter as installed on the thin wing

Thus, a simulation was performed based on the flight wing. This simulation used the exact same methodology used in all the other simulations but started with a model that matched the flight wing. The change in boundary condition was conservatively modeled by fixing the location where the adapter restricts wing motion. As the actual wing stiffness was unknown the values were held the same from the previous simulations. The geometry was updated with the as-constructed values. The finite element model was then solved, and the result converged to account for aerodynamic loading as has been done previously. The convergence to find roll coefficient was done with 80% actuation to match the flight test results.

Simulation results after convergence: Roll coefficient = 0.055

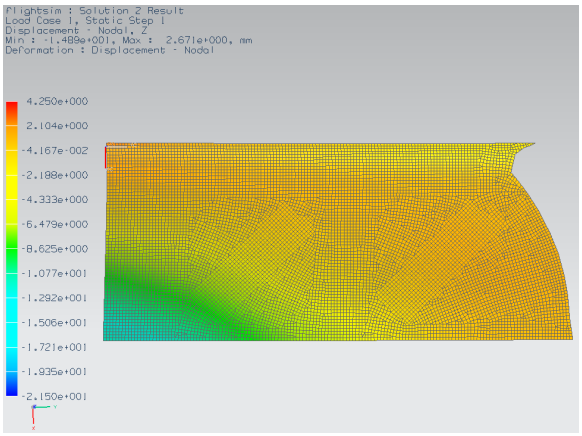

Figure 7.17: Deflections for simulation wing used in flight testing after convergence

In addition, the range in tip displacement from +100% to -100% actuation under no aeroloads is shown in Table 7.8 for both actual case and simulation. AVID LLC. measured the tip deflection of the flight wing with a laser.

Table 7.8: Total range in tip displacement comparing simulation to flight wing

Test Case	Range (mm)
Simulation	43.8
Actual Wing (Right)	32.0
Actual Wing (Left)	24.1

The flight testing was done at Virginia Tech's experimental flight facility at Kentland Farms. An unmanned flight vehicle was designed that incorporated the MFCs in both the wings' control surfaces and the elevators. The plane had a vertical stabilizer with no rudder. With the thin wing installed, the entire wing surface morphed with actuation. A picture of the flight vehicle with the thin wing installed is shown in Figure 7.18. The flight controller incorporated custom algorithms to account for MFC-specific issues such as hysteresis. A great deal of data was collected while the airplane did a variety of different maneuvers. The relevant tests for this research were roll doublets.

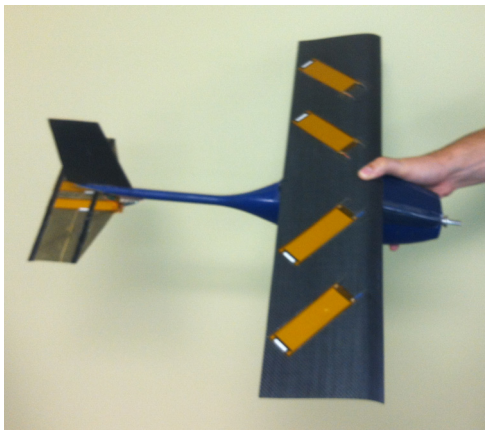

Figure 7.18: Picture of flight vehicle with thin wing installed

For roll doublets, the pilot remotely controlled the aircraft into steady, straight cruise flight. At which point, he flipped a switch and the autopilot sent signals to actuate roll briefly and then return to straight flight. To actuate roll, the wing MFCs were asymmetrically given $\pm 80\%$ constant actuation such that one side of the morphed up while the other side morphed down. The up/down actuations were then flipped for an equal amount of time to return the aircraft to its previous course. The amount of time the MFC were actuated determined the actual amount of roll. Two different times were used: One where the total doublet took 0.2 sec and the other where the doublet took 0.4 sec. Three runs were done for the 0.2 sec case while five runs were done for the 0.4 sec case. The response of the aircraft was then measured. Figure 7.19 shows the roll rate with the corresponding aircraft speed input for the three 0.2 sec test cases. Figure 7.20 shows the same data for the five 0.4 sec test cases. The experiments and data are courtesy of AVID LLC.

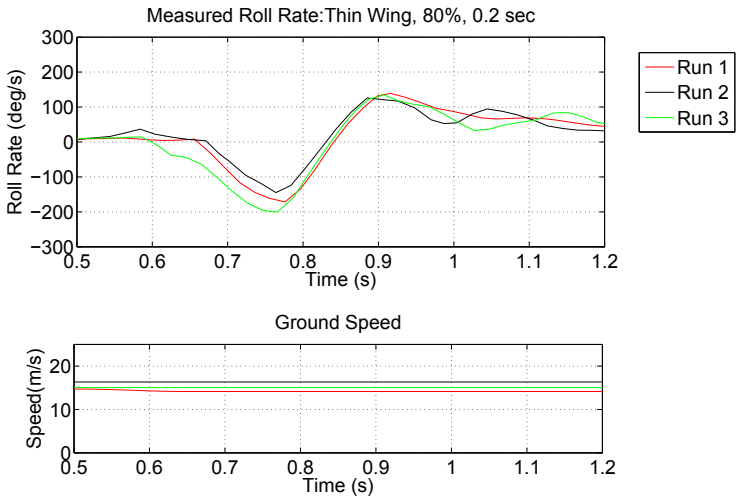

Figure 7.19: Flight data showing roll rate and ground velocity for thin wing airplane during 0.2 sec roll doublets

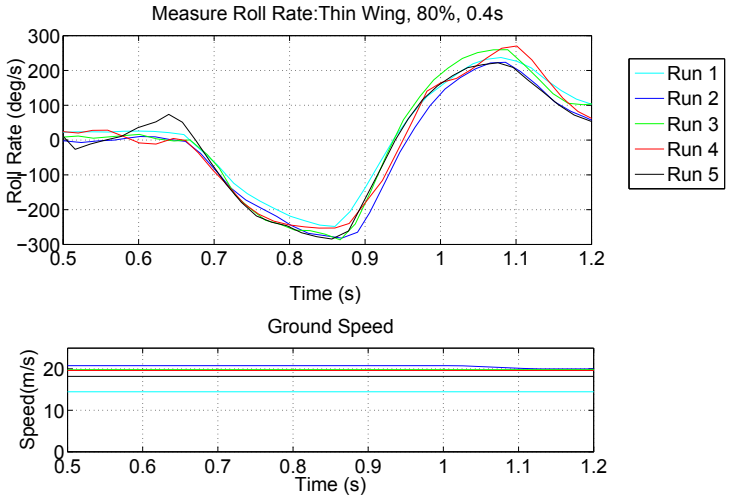

Figure 7.20: Flight data showing roll rate and velocity for thin wing airplane during 0.4 sec roll doublets

In order to compare the flight data to the simulations, the rolling moment coefficient was calculated from the roll rate. An approximation of the roll acceleration, α, was found by calculating the slope of the linear region near where the roll rate is zero. Then assuming the actuation is only significant roll moment, the rolling moment due to this actuation can then be calculated from Equation 7.2.

$$\text{Roll Moment}, M_x = \alpha_x I_{xx} \tag{7.2}$$

The moment of inertia for roll, I_{xx} was then roughly approximated by making some simplifications about the aircraft geometry. The axis of rotation was assumed to be the longitudinal axis of the fuselage. In reality, the axis will be slightly different depending on the aircraft configuration, but it will be close enough for this approximation. The wing's contribution to moment of inertia dominates the total by two orders of magnitude over that of contribution of the fuselage and tail. Thus, the aircraft moment of inertia was assumed to be equal to that of the wing. The wing moment of inertia was approximated by assuming the wing was a flat plate. The actual wing obviously has a curvature, but the inertia will dominated by the span so the effect of this curvature was assumed to be negligible. The wing was also assumed to be homogenous. This is also not the case, but without knowing the final densities of the different components, this rough assumption had to suffice. The moment of inertia was then calculated by the following Equation 7.3 from Marghitu and Dupac for a flat plate rotating about an axis as shown in Figure 7.21[29].

$$I_{xx} = \frac{1}{12} m(b^2 + t^2) + md^2 = 0.00511 kgm^2 \tag{7.3}$$

Where: m = mass of the entire wing was measured as 158.7 g, b = wingspan, 610 mm, t = average thickness, 0.55 mm, and d = distance shown in Figure 7.21 for parallel axis theorem

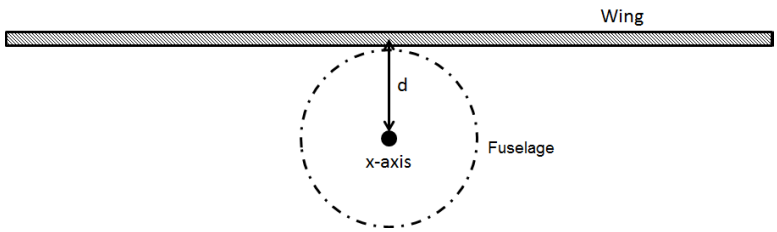

Figure 7.21: Diagram for roll moment of inertia calculations

Once the rolling moment is found, the rolling moment coefficient can be calculated from

Equation 7.1 which can also be written as shown in Equation 7.4.

$$\text{Roll Coefficient} = \frac{M_x}{\frac{1}{2}\rho V^2 b^2 c} \tag{7.4}$$

Where for this case: M = roll moment calculated from Equation 7.2 ρ = density of air, $1.19 kg/m^3$ V = ground velocity b = wingspan, 610 mm c = chord, 127 mm

Using this procedure, the rolling moment coefficient for each test run was calculated and shown in Table 7.9.

Table 7.9: Rolling moment coefficient for the eight flight test runs

Test Run	Doublet Duration (s)	Roll Coefficient
1	0.2	0.0300
2	0.2	0.0443
3	0.2	0.0427
4	0.4	0.0297
5	0.4	0.0240
6	0.4	0.0329
7	0.4	0.0496
8	0.4	0.0373
Average		0.0363

Comparison

First, comparing the maximum deflections of the actual flight wing and the flight wing simulation shows that the model significantly overestimated the tip deflection. The tip displacement range was approximately 28 mm for the actual wing, but the model predicted a range of 44 mm. Correspondingly, the FE model with AVL convergence overestimated the rolling moment coefficient compared to that calculated from the flight data. The flight data roll coefficient averaged to 0.036 while the simulation convergence predicted 0.055. The

difference between the two results does highlight some of the flaws with the model, but does not necessarily discredit the simulation results. While the deflections were different, the rolling moment results are consistent with one another. The change in C_{roll} from the simulation's 0.055 to the 0.036 from the flight data is approximately what is expected given the different deflections.

The deflection difference could be due to a number of factors. First, the true composite properties are relatively unknown. The stiffness of the composite is highly sensitive to the ratio of the stiff carbon fibers to the flexible epoxy. It could be the material stiffness values inputted to the simulation are much smaller than the actual values. This would lead to the simulation overestimating the deflection. Another possible explanation is a flaw in the thermal analogy. The thermal analogy derives values from manufacturer's datasheets for MFCs. The datasheets list approximate values and differences between individual MFCs could cause significant effects on true deflection and corresponding errors in the simulation results. The issues with material properties and the thermal analogy point to a possible significant variability between identically constructed MFC-actuated control surfaces. This variability is supported by the fact that even though the actual wing is nearly symmetric, the left and right sides show a significant difference in tip displacements.

Overall, the variability means that it may be a challenge to predict the behavior of a real wing with absolute accuracy using simulations. However, the relative simulation results and the comparisons studied in Section 7.8 would not be biased by this variability and are likely still true.

Chapter 8

Conclusion

8.1 Summary of Contributions

There were two major sections this research. First, the current technology in MFC airfoils was evaluated against a similar conventional flapped airfoil. The comparison was done with 2-D wind tunnel experiments and frequency response tests. Each airfoil's performance was measured by their ability to create lift while minimizing drag. The experiments showed that the servo airfoil was better able to maintain its profile under aerodynamic loading and thus created more lift. However, the differences were relatively small and could also be due to manufacturing differences in profile or surface finish. To strictly quantify any benefit of continuous versus discontinuous profile, a flapped airfoil and morphing airfoil were rapid prototyped based on CAD models and tested in the wind tunnel. The continuous, morphed profile showed significantly higher lift and lower drag. Several configurations of actuating MFC airfoils were also compared including airfoils with thick and thin profiles and varying the size of the MFC actuators. Again, an advantage of MFC technology is the many possible configurations with both thick and thin wings. As expected, the deflection and aerodynamics of the MFC airfoils with the larger actuators were not as dependent on aerodynamic loading. The thick and thin airfoils both produced similar results and provided

adequate range in lift coefficient. The effect of MFC hysteresis on the coefficients of lift and drag was also quantified. The frequency response testing highlighted the increased bandwidth possible with MFCs compared to conventional servos, but also illustrated some limitations. Applying aeroloads had a damping effect on the response of the MFC airfoils. The tests also highlighted the effect of the voltage amplifier on the system.

The second part of this thesis evaluated the effect of different configuration parameters on the performance of the MFC morphing. The research focused on a thin UAV wing with embedded MFC actuators such that the entire surface of the wing morphed. The comparisons were done with simulations. A finite element solver calculated the deflected profile of a particular configuration. Vortex lattice software then determined the aerodynamic loads. The process was repeated to convergence to account for the effects of aeroelasticity. The performance of each was measured from the simulated rolling moment coefficient and difference in deflection with and without loading. From the simulations, the following conclusions were made. The best spanwise location of a single MFC bimorph was toward the center middle of each side of wing. Also, using two smaller actuators produced better results, and it was best to center them near the middle of each side of the wing. A thicker wing led to less aeroelastic difference but a significant decrease roll coefficient. Similarly, using a more flexible substrate increased roll coefficient, but substantially increased the deflection due to aerodynamic loading. A design was then developed which employed extra thickness only on the leading edge. This wing was built and tested in flight. The simulations overestimated the static deflection of the real wing. This highlighted some of the problems of modeling such a complex system with significant variability. Given the different deflection predictions, the roll coefficient from flight testing was consistent with that of the simulation.

8.2 Recommendations for Future Work

While this research answered a few questions about the potential of MFC technology in UAV control surfaces, new questions were raised and many still remain. One of the huge challenges is to account for the aeroelasticity of a system that depends on flexibility for actuation. First, how much aeroelasticity is acceptable needs to be defined. In this thesis, the aeroelasticity was somewhat qualitatively described looking at the deflection with and without aeroloads in a static situation. In reality, a UAV in flight is looking at many dynamic load cases. The effect of dynamic loads on the flexible wings would be an interesting and important area of research. For example, flutter is not something that was considered in this work, but may dictate how flexible these morphing wings can be. It is important to how it what flight condition and speed will flutter be an issue. Gustafson noted limit cycle oscillations were a problem during his wing tunnel testing[5]. This type of behavior should be examined in further evaluations of MFC control surfaces. The next question is can aeroelasticity be minimized. This thesis quantified the effect of a few of the many different parameters. There are an endless number of MFC configurations, and it would be informative to look at parameters not studied here such as varying the chordwise location, other material properties, composite orientation, or the orientation of MFC bimorphs. More interestingly creating more complex designs by mixing and matching the different parameters could yield better results.

Another issue that has been illustrated in this thesis is the need for more consistency in the MFC surfaces. The flight tested thin wing varied in deflection even comparing one wing half to the other. Its possible more complex techniques and models could yield better deflection predictions, but part of the problem is in the MFC-composite substrate fabrication. Looking at the variability in the MFCs themselves and its effect would be good method of improving predictions. In addition, developing other manufacturing techniques for laying up the MFCs and composites could provide more consistent wing actuation. As Gustafson pointed out, the fiber volume fraction of the composite drives the composite properties and method used

in the current MFC layups allows a great deal of variability in the volume fractions[5]. Also, updating the simulation model with values from experiments could increase the accuracy of the model. It is possible to derive new thermal analogy coefficients from the flight test wing. There are also methods to determine material stiffnesses and composite fiber fractions from the flight wing and update the values in the model.

In a bigger picture for the MFC morphing wing technology, there are some interesting comparisons yet to be fully quantified. AVID LLC. has done some preliminary comparisons of power and weight, but it would be important to research how each of those can be optimized[3]. A potential MFC advantage that was not examined in this thesis was reliability and survivability. MFC actuation requires no moving parts or linkages unlike servos and flaps. Quantifying any advantage in this area could add credence to expanded use of the MFCs. In addition, scalability is an interesting research question. Looking at the design trade-offs could yield upper or lower limits to the size of aircraft that could benefit from MFC actuated control surfaces.

Bibliography

[1] General Atomics Aeronautical Systems Inc. *MQ-1 Predator*. 2012. URL: http://www.ga-asi.com/products/aircraft/pdf/MQ-1_Predator.pdf.

[2] Aeryon Labs Inc. *SCOUT Micro-UAV*. 2012. URL: http://www.aeryon.com/attachments/aeryon-scout-brochure.pdf.

[3] Osgar John Ohanian III et al. "Piezoelectric Morphing versus Servo-Actuated MAV Control Surfaces". In: *53rd AIAA/ASME/ASCE/AHS/ASC Structures, Structural Dynamics and Materials Conference*. 2012.

[4] Onur Bilgen. "Macro Fiber Composite Actuated Unmanned Air Vehicles: Design, Development, and Testing". Master's thesis. Virginia Polytechnic Institute and State University, 2007.

[5] Eric A. Gustafson. "Design, Simulation, and Wind Tunnel Verification of a Morphing Airfoil". Master's thesis. Virginia Polytechnic Institute and State University, 2011.

[6] Troy A. Probst et al. "Smart Material Actuators as a Means of UAV Flight Control". In: *AIAA Aerospace Sciences Meeting*. 2012.

[7] W. Keats Wilkie et al. "Low-Cost Piezocomposite Actuator for Structural Control Applications". In: *SPIE Smart Structurs and Materials*. 2000.

[8] Robert Brett Williams. "Nonlinear Mechanical amd Actuation Characterization of Piezoceramic Fiber Composites". Ph.D. dissertation. Virginia Polytechnic Institute and State University, 2004.

[9] Onur Bilgen. "Aerodynamic and Electromechanical Design, Modeling and Implementation of Piezocomposite Airfoils". Ph.D. dissertation. Virginia Polytechnic Institute and State University, 2010.

[10] Kelly Stewart, Jeffery Wagener, and Gregg Abate. "Design of the air force research laboratory micro aerial vehicle research configuration". In: *AIAA Aerospace Sciences Meeting*. 2007.

[11] Lauren Butt et al. "Wing Morphing Design Utilizing Macro Fiber Composite Smart Materials". In: *Conference for the Society of Allied Weight Engineers, Inc.* 2010.

[12] Bradley W. LaCroix and Peter G. Ifju. "Utilization and Performance Enhancements of Multiple Piezoelectric Actuators on Micro Air Vehicles". In: *50th AIAA Aerospace Sciences Meeting*. 2012.

[13] Silvestro Barbarino et al. "Review of Morphing Aircraft". In: *Journal of Intelligent Material Systems and Structures* 22 (2011).

[14] Roelof Vos et al. "Post-buckled precompressed elements: a new class of control actuators for morphing wing UAVs". In: *Smart Materials and Structures* 16 (2007), pp. 919–926.

[15] Ugo Icardi and Laura Ferrero. "SMA Actuated Mechanism for an Adaptive Wing". In: *Journal of Aerospace Engineering* 24 (2011), pp. 140–143.

[16] Larry D. Peel et al. "Development of a simple morphing wing using elastomeric composites as skins and actuators". In: *ASME Conference on Smart Materials, Adaptive Structures and Intelligent Systems*. 2008.

[17] Mustafa Turan. "Tools for the Conceptual Design and Engineering Analysis of Micro Air Vehicles". Master's thesis. Department of the Air Force Air University, 2009.

[18] Richard J. Margason and John E. Lamar. *Vortex-Lattice FORTRAN Program for Estimating Subsonic Aerodynamic Characteristics of Complex planforms*. NASA Langley Research Center.

[19] Daniel T. Grant. "Modeling and Dynamic Analysis of a Multi-Joint Morphing Aircraft". Master's thesis. University of Florida, 2009.

[20] Smart Material Corporation. *Macro Fiber Composite*. 2012. URL: http://www.smart-material.com/MFC-product-main.html.

[21] Michael S. Selig et al. *Aerodynamics for Engineers*. Prentice Hall, 1989.

[22] Joseph Katz and Allen Plotkin. *Low-Speed Aerodynamics*. Cambridge University Press, 2001.

[23] Kevin Kochersberger et al. "An evaluation of the Wright 1901 glider using full scale wind tunnel data". In: *40th AIAA Aerospace Sciences Meeting and Exhibit*. 2002.

[24] Michael W. Hyer. *Stress Analysis of Fiber-Reinforced Composite Materials*. DEStech Publications, Inc., 2009.

[25] Mark Drela and Harold Youngren. *AVL 3.30 User Primer*. 2010. URL: http://web.mit.edu/drela/avl/avl_doc.txt.

[26] John J. Bertin and Michael L. Smith. *Aerodynamics for Engineers*. Prentice Hall, 1989.

[27] Bill Vaglienti, Marius Niculescu, and Jeff Hammitt. *Piccolo Simulator*. Cloud Cap Technology.

[28] Tuncer Cebeci et al. *Physics of Unsteady Flows*. Springer, 2005.

[29] Dan P. Marghitu and Mihai Dupac. *Advanced Dynamics*. Springer, 2012.

[30] American Institute of Aeronautics and Astronautics. *Assessment of Experimental Uncertainty With Application to Wind Tunnel Testing*. 1999.

Appendix A

2-D Wind Tunnel Measurement Uncertainty

The primary parameters of interest in these wind tunnel experiments are the sectional lift and drag coefficients. This section describes the uncertainty associated with these coefficients. Uncertainty calculations are based on the AIAA Standard: Assessment of Experimental Uncertainty With Application to Wind Tunnel Testing[30]. This standard presents a procedure for estimating the uncertainty in experimental results. The applicable steps and equation are reproduced here and then applied to the 2-D wind tunnel data from Chapter 4. All calculations were completed based on a 95% confidence interval.

The first step is to take the data reduction equation, r, and identify the measured variables, X_i. For this research, the data reduction equations are the definitions of lift and drag coefficient given in Equation 3.1 in Section 3.2. From this the measured variables are identified as the force (lift or drag), the dynamic pressure, q_∞, the measured span, b, and the measured chord, c. The uncertainty due to the span and chord measurements is negligible compared to the other sources and is not included. The next step is to estimate the uncertainty on each of these measurements using the equations below[30]. For a given measured variable, X_i, the uncertainty, U_i, is a combination of the bias limit, B_i, and the precision limit, P_i.

$$U_i = (B_i^2 + P_i^2)^{1/2} \tag{A.1}$$

The precision limit, P_i, is based on the standard deviation, S_i, times a factor, K. For a 95% confidence uncertainty, $K = 2$. In addition, for the measured variables that are averages over time, Pi is divided by the square root of the number of samples in that time, N_i. The force and dynamic pressure measurements are both averages over time. The bias limits are based on the measuring instrument and the relevant values for this research are shown in Table A.1.

$$P_i = KS_i \tag{A.2}$$

$$P_{\bar{X}_i} = \frac{P_i}{\sqrt{N_i}} \tag{A.3}$$

Table A.1: Bias limit values for the three primary measurement instruments. Values take from Gustafson[5]

Measurement	B_i
Force	0.068 N
Pressure	3.32 Pa

Next, in order to calculate the uncertainty in the overall coefficients, the uncertainty in the constituent measurements is propagated as shown in Equations A.4 through A.7. The equations are from [30].

$$U_r = (B_r^2 + P_r^2)^{1/2} \tag{A.4}$$

$$P_r = (\sum_{i=1}^{J} (\theta_i P_i)^2)^{1/2} \tag{A.5}$$

$$B_r = (\sum_{i=1}^{J} (\theta_i B_i)^2)^{1/2} \tag{A.6}$$

$$\theta_i = \frac{\partial r}{\partial X_i} \tag{A.7}$$

From these equations, the uncertainty in the coefficients can be calculated for each actuation level at each support angle. Given the number of actuation levels, support angles, wind speeds, and airfoils, the uncertainties were averaged for easier visualization. The average coefficient uncertainty is presented for each airfoil at each wind speed. These values are shown in Tables A.2 through A.5.

Table A.2: Mean and Maximum Coefficient Uncertainty for GenMAV MFC 8528 airfoil

	C_l		C_d	
Wind Speeds (m/s)	U_{mean}	U_{max}	U_{mean}	U_{max}
9	0.098	0.133	0.079	0.102
13	0.051	0.065	0.042	0.048
17	0.028	0.036	0.024	0.026

Table A.3: Mean and Maximum Coefficient Uncertainty for GenMAV MFC 8514 airfoil

	C_l		C_d	
Wind Speeds (m/s)	U_{mean}	U_{max}	U_{mean}	U_{max}
9	0.086	0.113	0.071	0.085
13	0.045	0.061	0.038	0.042
17	0.029	0.036	0.025	0.028

Table A.4: Mean and Maximum Coefficient Uncertainty for thick MFC airfoil

	C_l		C_d	
Wind Speeds (m/s)	U_{mean}	U_{max}	U_{mean}	U_{max}
9	0.102	0.141	0.077	0.091
13	0.052	0.070	0.040	0.045
17	0.028	0.037	0.023	0.025

Table A.5: Mean and Maximum Coefficient Uncertainty for thick servo airfoil

	C_l		C_d	
Wind Speeds (m/s)	U_{mean}	U_{max}	U_{mean}	U_{max}
9	0.101	0.143	0.080	0.104
13	0.052	0.078	0.041	0.048
17	0.031	0.043	0.024	0.027

Appendix B

Load Cell Calibration

The most critical and most sensitive instruments used in the 2-D wind tunnel testing was the load cells. The load cells measured the force of lift and drag. They are sensitive to a variety of factors and thus it is important that they be calibrated regularly to ensure accurate results. The calibration process developed by Gustafson consisted of hanging precision weights from the C-arm[5]. The weights were positioned such that their weight simulated lift and drag forces. The load cells outputted a voltage that corresponds to a force. The voltage was measured and graphed with the corresponding weight of the precision weights. The weight was graphed as function of voltage in order to calculate the calibration curve which converts the outputted voltage to lift or drag in an actual experiment. The graphs are shown in Figures B.1 and B.2. The lift and drag load cells were calibrated separately.

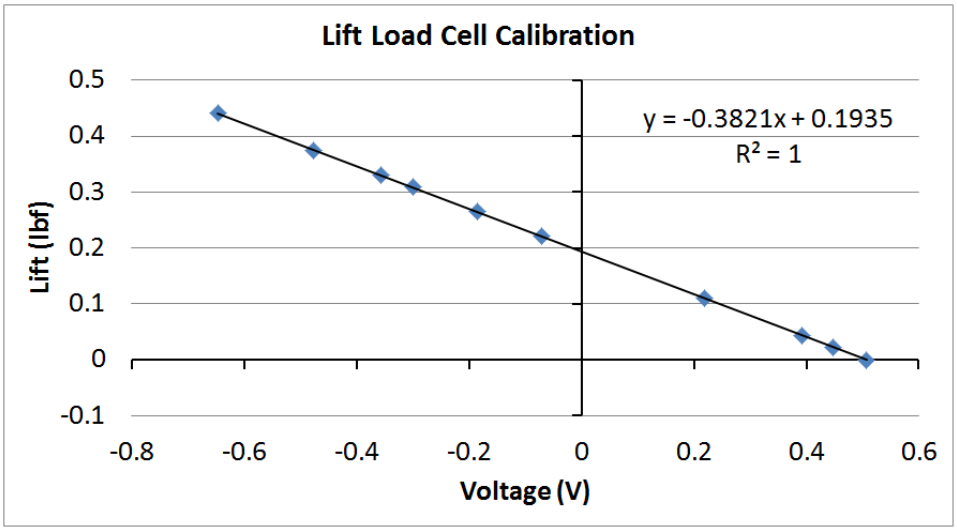

Figure B.1: Lift load cell calibration

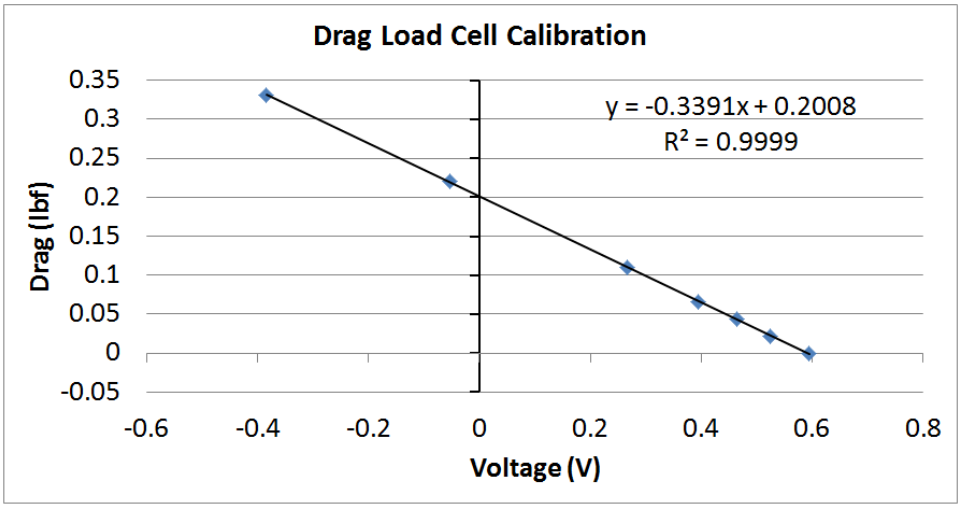

Figure B.2: Lift load cell calibration